Tufts UNIVERSITY | SCHOOL OF ENGINEERING Mechanical Engineering

Thermophysical Property Measurement and Modelling of Ni-Cr- (Fe, Mo) Superalloy Analogs

A dissertation submitted by

Peace Muusha

IN PARTIAL FULFILLMENT OF THE REQUIREMENTS FOR THE DEGREE OF

DOCTOR OF PHILOSOPHY

IN

MECHANICAL ENGINEERING

Tufts University

February 2026

Advisor: Professor Douglas Matson

Abstract

The development of advanced materials for high-performance applications in aerospace, energy, and chemical industries relies on precise prediction and control of thermophysical properties. This work presents an integrated experimental and computational investigation of Ni-Cr-Fe and Ni-Cr-Mo based ternary alloys, with a focus on four ternary analog systems: TA 625-Mo, TA 625-Fe, TA 718-Ni, and TA 718-Fe, which were selected as simplified models for the industrial superalloys Inconel 625 and Inconel 718.The primary objective is to measure the density and surface tension of these analog alloys and compare the results with those of their industrial counterparts. Experimental measurements were conducted using Electrostatic Levitation (ESL) at NASA's Marshall Space Flight Center (MSFC), and Electromagnetic Levitation (EML) in parabolic flights providing short-duration zero-gravity environments. Surface tension was modelled using the Conventional Butler Model, while density was determined through direct experimental evaluation and excess volume modelling. A comprehensive uncertainty analysis was evaluated to identify and quantify potential sources of error in experimental approach, assessing their influence on data accuracy and reliability. By combining high-precision experimental data with robust thermodynamic modelling, this work addresses a critical knowledge gap in the thermophysical characterization of ternary alloy systems. The insights gained provide a deeper understanding of their physical behaviour and support the optimization of superalloy analogs for demanding industrial applications such as turbine blades in jet engines, components in rocket propulsion systems, high-efficiency heat exchangers in power plants, and corrosion-resistant equipment for chemical processing, where materials must maintain mechanical strength, thermal stability, and oxidation resistance under extreme operating conditions.

Signature Page

Author	**Peace Muusha**	
Advisor & Committee Chair	Dr. Douglas M. Matson, Professor Department of Mechanical Engineering Tufts University	
Committee Member	Dr. Jannatun Nawer, Research Assistant Professor Department of Mechanical Engineering Tufts University	
Committee Member	Dr. Greses Pérez, Assistant Professor Department of Civil and Environmental Engineering Tufts University	
Committee Member	Dr. Stephan Schneider, Scientist Institut für Materialphysik im Weltraum Deutsches Zentrum für Luft- und Raumfahrt (DLR)	

Acknowledgements

This work would not have been possible without the encouragement, guidance, and generosity of many people and institutions. I sincerely appreciate the scientists Stephan Schneider, Georg Lohoefer, Juergen Brillo, and Benedikt Reiplinger from DLR, Institut für Materialphysik im Weltraum along with colleagues from the European Space Agency (ESA), for their collaboration and assistance in providing access to the EML equipment. Their expertise and commitment were essential to the success of this research. I am equally thankful to Michael SanSoucie, Brandon Philips, Glenn Fountain, Prado Irene, Bergeron Kane M, and Trudy Allen from NASA's Marshall Space Flight Center (MSFC) ESL facility for their continued guidance and technical support during experimental testing over the years. This research was made possible through the generous funding provided by NASA, for which I am deeply grateful. This financial support enabled the successful execution of this work.

I also wish to thank Professor Jannatun Nawer, Brian Stanford, Jeremiah Bonso, and Dr. Colby Azersky from Tufts University for their valuable contributions, technical assistance, and thoughtful feedback, which have greatly enhanced the quality of this dissertation. I am profoundly thankful to my academic advisor, Professor Douglas Matson, for his exceptional mentorship, insightful guidance, and unwavering encouragement. His expertise, vision, and support have been instrumental in shaping both the direction and the impact of this research.

Finally, I am especially grateful to my wife, Ruvarashe Makuwe, whose love, patience, and understanding have been my greatest source of strength. I also extend my heartfelt thanks to my family and friends, whose support and encouragement have carried me through the challenges of this journey.

Table of Contents

List of Figures

Table of Tables

Nomenclature

ICME: Integrated Computational Materials Engineering

ESL: Electrostatic Levitation

EML: Electromagnetic Levitation

TA: Ternary Analog

Inconel 625: A nickel-based superalloy known for corrosion resistance

Inconel 718: A nickel-based superalloy known for strength at high temperatures

TA 625-Mo: Ternary alloy analog based on Inconel 625 with molybdenum (Mo)

TA 625-Fe: Ternary alloy analog based on Inconel 625 with iron (Fe)

TA 718-Ni: Ternary alloy analog based on Inconel 718 with less iron (Fe)

TA 718-Fe: Ternary alloy analog based on Inconel 718 with more iron (Fe)

Surface Tension: A measure of the cohesive forces acting at the surface of a liquid

Viscosity: A measure of a fluid's resistance to flow

Density: Mass per unit volume of a substance

Butler Model: A model used to calculate surface tension

Parabolic Flight: A method of processing microgravity through controlled flight maneuvers

Uncertainty Analysis: The process of quantifying uncertainty in measurements or model

Cr: Chromium

Ni: Nickel

Mo: Molybdenum

Fe: Iron

Co: Cobalt

Nb: Niobium

W: Tungsten

Ta: Tantalum

Re: Rhenium

Al: Aluminum

Ti: Titanium

Hf: Hafnium

CHAPTER 1. Introduction

The design and optimization of high-performance materials for aerospace, energy, and chemical applications depend on accurate knowledge of thermophysical properties, particularly density and surface tension, which influence melt behaviour, solidification, and defect formation in processes such as casting and additive manufacturing [1]. This work examines four Ni-Cr-Fe and Ni-Cr-Mo based ternary analog alloys, namely TA 625-Mo, TA 625-Fe, TA 718-Ni, and TA 718-Fe, developed as simplified representations of the industrial superalloys Inconel 625 and Inconel 718. These analogs enable targeted investigation of the key elemental interactions of Ni, Cr, Mo, and Fe without the complexity introduced by fully multi-component chemistries.

The study employs advanced levitation methods to generate experimental measurements that are supplemented with thermodynamic modelling to improve the prediction of these properties. The scope encompasses both ternary analog systems and their industrial counterparts. The present chapter outlines the research motivation, objectives, methodology, and organization of the dissertation.

1.1 Motivation

Modern manufacturing technologies and their application in aerospace, energy, and chemical industries demand high-performance materials with precisely controlled thermophysical properties. The accuracy of manufacturing process models, such as those used in casting, additive manufacturing, and welding, depends heavily on the fidelity of the thermophysical property database for metals and alloys. Among these properties, density and surface tension play critical roles in controlling melt behavior, solidification, defect formation, and final component quality. Accurate measurement and modelling of these properties enable better predictive capabilities, reduce reliance on costly trial-and-error experimentation, and allow engineers to optimize processes for performance, cost-effectiveness, and reliability [2].

Understanding surface tension and ternary alloy behavior is important because these properties govern how liquid metals flow, how defects form, and how advanced superalloys perform in the severe thermal environments found in jet engines, gas turbines, and space hardware. They therefore influence both manufacturing outcomes and the long-term reliability of critical engineering systems.

Advanced alloy design benefits greatly from integrating experimental data with computational models, a principle central to Integrated Computational Materials Engineering (ICME). However, for many technologically important alloys, particularly Ni-Cr-Fe and Ni-Cr-Mo based ternary systems, high-precision thermophysical data remain scarce, especially under conditions that eliminate the influence of buoyancy-driven convection [3]. This limitation restricts the accuracy of process simulations and the ability to optimize manufacturing routes.

This research addresses this gap by investigating four Ni-Cr-Fe and Ni-Cr-Mo based ternary analog alloys: TA 625-Mo, TA 625-Fe, TA 718-Ni, and TA 718-Fe. These analogs are simplified models of the industrial superalloys Inconel 625 and Inconel 718 and allow focused study of Ni–Cr–Mo and Ni–Cr–Fe interactions without the complexity of multi-component chemistries. Measurements are conducted using non-contact levitation methods, specifically Electromagnetic Levitation (EML) aboard the short-duration microgravity parabolic flights and Electrostatic Levitation (ESL) at NASA's Marshall Space Flight Center (MSFC). The absence of container contact avoids contamination, minimizes heterogeneous nucleation, and enables more precise determination of density and surface tension at high temperatures [4].

Microgravity experiments offer significant advantages over ground-based facilities, including improved sample sphericity, elimination of buoyancy-driven segregation, and reduced convection, all of which lead to higher precision in property evaluation. By comparing results from ground-based and space-based measurements, this research not only delivers high-quality thermophysical property data but also demonstrates the advantages of microgravity platforms for materials research.

1.2 Objectives of the Research

The primary objectives of this study are to:

i. Measure density and surface tension of industrial Inconel 625 and Inconel 718 as well as Ni–Cr–Fe and Ni–Cr–Mo ternary analog alloys (TA 625-Mo, TA 625-Fe, TA 718-Ni, TA 718-Fe) over a wide temperature range using ESL and EMLtechniques.
ii. Model liquid density using the Partial-Molar-Volume (PMV) approach, including excess volume (V^E) corrections based on Redlich–Kister parameters.
iii. Develop and apply thermodynamic surface tension models, particularly the Conventional Butler Model, and compare with experimental results.

iv. Perform uncertainty analysis to assess data accuracy and highlight the benefits of microgravity testing.

By combining high-precision experimental data with robust modelling approaches, this research aims to strengthen the thermophysical property database for Ni-Cr-Fe and Ni-Cr-Mo based ternary alloys and support the optimization of manufacturing processes for critical high-performance applications.

1.3 Materials

This study investigates four Ni-Cr-Fe based ternary analog alloys: TA 625-Mo, TA 625-Fe, TA 718-Ni, and TA 718-Fe. These alloys are simplified representations of two widely used industrial superalloys, Inconel 625 and Inconel 718 (Table 1). The analogs are designed to retain the essential elemental frameworks of the parent alloys while omitting secondary alloying elements, allowing for a focused investigation of the interactions between nickel, chromium, molybdenum, and iron.

Inconel 625 is primarily composed of nickel and chromium, with significant additions of molybdenum and iron that enhance corrosion resistance, oxidation resistance, and high-temperature stability. Its composition provides solid solution strengthening without the need for heat treatment, making it particularly suitable for marine, chemical, and aerospace environments where resistance to pitting and crevice corrosion is essential [5].

Inconel 718 contains nickel, chromium, and iron in balanced proportions, with niobium and small additions of aluminum and titanium. These elements promote precipitation hardening, producing high strength over a broad temperature range. Inconel 718 is widely used in aerospace turbine engines and other critical applications requiring exceptional mechanical properties and creep resistance [6].

Table 1: Nominal compositions (at%) of industrial nickel-based superalloys

Alloy	Ni	Cr	Mo	Fe	Co	Nb	Al	Ti
Inconel 625	63.8	24.0	5.0	4.3	0.3	2.1	0.4	0.1
Inconel 718	53.7	20.1	1.8	18.7	0.2	3.2	1.1	1.2

The nominal compositions of the ternary analog alloys (Table 2), expressed in atomic %, TA 625-Mo and TA 625-Fe are derived from Inconel 625, while TA 718-Ni and TA 718-Fe are

derived from Inconel 718. In TA 625-Mo, molybdenum is retained as the third element, whereas in TA 625-Fe, molybdenum is replaced with iron to isolate the role of Fe in the Ni–Cr system. Similarly, TA 718-Ni retains relative binary ratios within the Ni–Cr–Fe framework of Inconel 718 at concentrations representing maximum Ni content, while TA 718-Fe increases the Fe content to evaluate its influence on thermophysical properties.

Table 2: Nominal composition (at%) of proposed ternary analogue alloys

Alloy	Ni	Cr	Mo	Fe
TA 625-Mo	69	26	5	- -
TA 625-Fe	69	26	- -	5
TA 718-Ni	58	22	- -	20
TA 718-Fe	48	18	- -	34

Brian Fu [7] conducted a complementary study focused on modeling evaporation behavior in simplified ternary analogs of Inconel 625 and Inconel 718 during electrostatic levitation experiments. His thesis applied a non-ideal Langmuir evaporation model, incorporating Thermo-Calc activity coefficients to correct species-specific vapor pressures, and validated predictions using experimental mass-loss measurements collected at NASA MSFC. By examining Ni–Cr–Fe and Ni–Cr–Mo ternary systems, he quantified the relative volatility of constituent elements and demonstrated that chromium exhibits the highest evaporation tendency, while overall composition changes remain small under typical molten-state hold conditions [7]. His work complements the broader levitation research by improving understanding of evaporation-driven composition shifts and by establishing a practical framework for modeling non-ideal vaporization in nickel-based alloy analogs, providing additional confidence in thermophysical property measurements performed under containerless conditions

1.4 Dissertation Outline

This dissertation is organized into the following chapters:

Chapter 1 – Introduction

Presents the research background, motivation, objectives, and materials studied.

Chapter 2 – Experimental Techniques and Methodologies

Describes alloy sample preparation, experimental facilities, and measurement procedures for density and surface tension. It details the operation of the Electrostatic Levitation (ESL) and Electromagnetic Levitation (EML) systems under parabolic flight setup, temperature corrections, and methods for frequency identification in signal processing.

Chapter 3 – Thermodynamic Modelling

Outlines the theoretical framework for modelling liquid density and surface tension. The chapter presents the Partial-Molar-Volume (PMV) approach with ideal and non-ideal excess-volume (V^E) formulations for density, and the Butler Model extended to ternary alloys for surface tension. Computational implementation and model integration with experimental results are also described.

Chapter 4 – Results

Provides experimental and modelled results for density and surface tension of the four ternary analog alloys across a wide temperature range. Comparisons are made between ESL, EML, and parabolic flight data, as well as with industrial superalloys Inconel 625 and Inconel 718.

Chapter 5 – Discussion

Analyses the modelled results and compares the behaviour of ternary analogs with their industrial counterparts. It interprets trends in composition, examines model performance, and discusses implications for manufacturing and ICME applications.

Chapter 6 – Uncertainty Analysis

Quantifies experimental and modelling uncertainties related to temperature, surface tension, and density measurements. The chapter also evaluates sample evaporation, facility performance, and the benefits of microgravity data quality.

Chapter 7 – Conclusion and Future Work

Summarizes the key findings, outlines future research directions, and presents closing remarks on the contribution of this study to alloy thermophysical property modelling and microgravity materials research.

CHAPTER 2. Experimental Techniques and Methodologies

This chapter outlines the preparation of ternary alloy samples and the use of Electrostatic Levitation (ESL) and Electromagnetic Levitation (EML) to measure thermophysical properties under containerless conditions. ESL at NASA MSFC enabled high-precision measurements in ultra-high vacuum, while EML experiments on parabolic flights provided short duration microgravity conditions. The chapter also introduces the droplet oscillation technique for density and surface tension measurements, with frequency identification performed using period measurement, cycle counting, FFT, Maximum Amplitude (MA), and Frequency Crossover (CO) methods.

2.1 Sample Preparation

Samples for Electrostatic Levitation (ESL) and Electromagnetic Levitation (EML) experiments were prepared in accordance with the dimensional and material requirements of each facility. For ESL measurements, the sample diameter was kept below 2 mm to comply with chamber constraints and to ensure stable levitation during high-temperature processing.

The four ternary analog alloys investigated in this study were produced from pre-alloyed stock. Sections of the required size were cut using precision saws and arc-melted into near-spherical shapes. Final sample masses for ESL testing ranged from 30 to 50 mg, depending on alloy density. Surfaces were carefully polished to minimise geometric irregularities and to reduce surface oxide nucleation sites that could compromise measurement accuracy.

For TEMPUS EML experiments conducted during parabolic flights larger samples were required, typically between 5 and 8 mm in diameter, to ensure stable levitation and measurable droplet oscillations. These samples were prepared by similar precision cutting, shaping, arc melting, and polishing to achieve a spherical geometry and uniform surface finish.

All samples (Appendix A) were handled under strict contamination-control procedures to prevent oxidation or any alteration to their thermophysical properties prior to testing. The target mass for each sample was calculated in advance using known density values and the specific volume requirements of the experimental platform. Appendix B contains the Acceptance Data Package records for the samples processed in the TEMPUS EML parabolic-flight campaign.

2.2 Electrostatic Levitation (ESL)

Electrostatic Levitation (ESL) is a container-less technique that levitates a charged sample using a static electric field, allowing for precise control of its position and thermal environment, with subsequent laser-based heating. By separating the levitation and heating processes, ESL eliminates contamination and surface contact, making it ideal for studying thermophysical properties at high temperatures. The sample, typically a small droplet (~40 milligrams), is levitated through a complex positioning algorithm during laser thermal processing. This setup minimizes surface deformation, allowing accurate measurements of the sample's behaviour [2].

At NASA's Marshall Space Flight Center (MSFC) shown in Figure 1, the ESL facility operates in an ultra-high vacuum (UHV) environment (10^{-8} Torr) to prevent arcing and contamination. The sample is heated by a radial laser, and Marangoni convection is minimized during free cooling. Marangoni convection arises from surface tension gradients caused by temperature differences within the liquid. Since surface tension decreases with increasing temperature, fluid motion occurs from hotter regions (lower surface tension along the equator) toward cooler regions (higher surface tension at the poles), generating internal flow during heating.

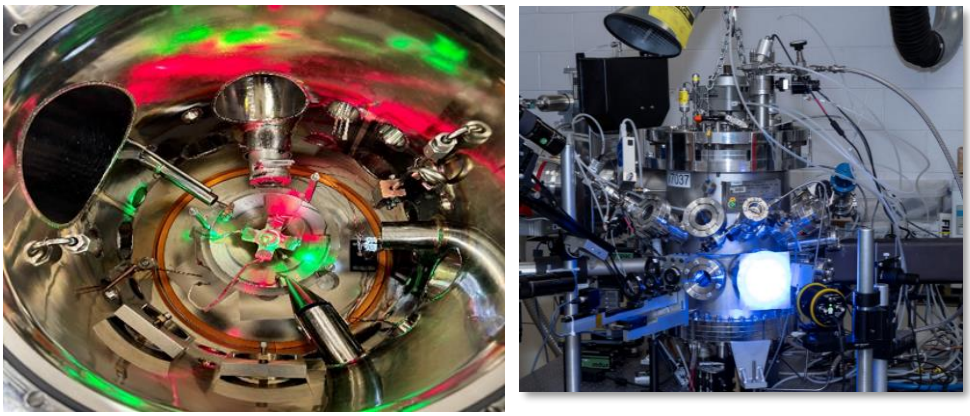

Figure 1: MSFC/ESL –photos courtesy of NASA [8]

High-speed backlit imaging captures side-view projections of the levitated sample with a resolution of 512x512 pixels (Figure 2). These images are processed using edge-detection algorithms to determine the sample's area, enabling accurate density and surface tension measurements as a function of time and temperature. During density testing the heating laser is turned off to minimize Marangoni convection and thus the thermal profile is characterized by a sudden, rapid decline in temperature (Figure 3).

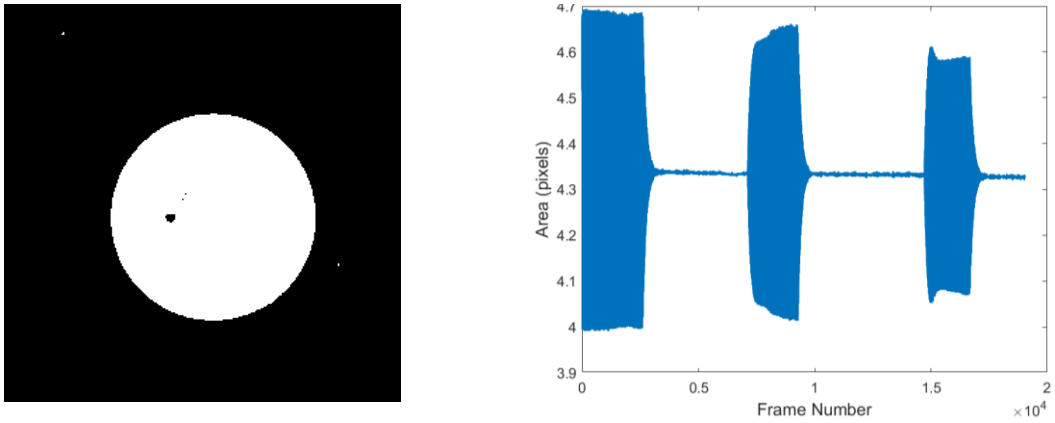

Figure 2: High-speed backlit imaging and processed area data from MSFC/ESL experiments

For surface tension measurements, the sample is first melted and then maintained at a constant temperature by adjusting the laser power to balance radiative thermal losses (Figure 3). As the sample spins, thermal gradients between the poles and equator lead to Marangoni convection, affecting internal fluid flow. After achieving thermal equilibrium, the levitation field is oscillated near the natural frequency of the sample (typically 150–200 Hz) to induce axial surface deformations [9]. High-speed cameras capture these oscillations at 1000 frames per second, enabling calculations of surface tension based on the rate of oscillation frequency.

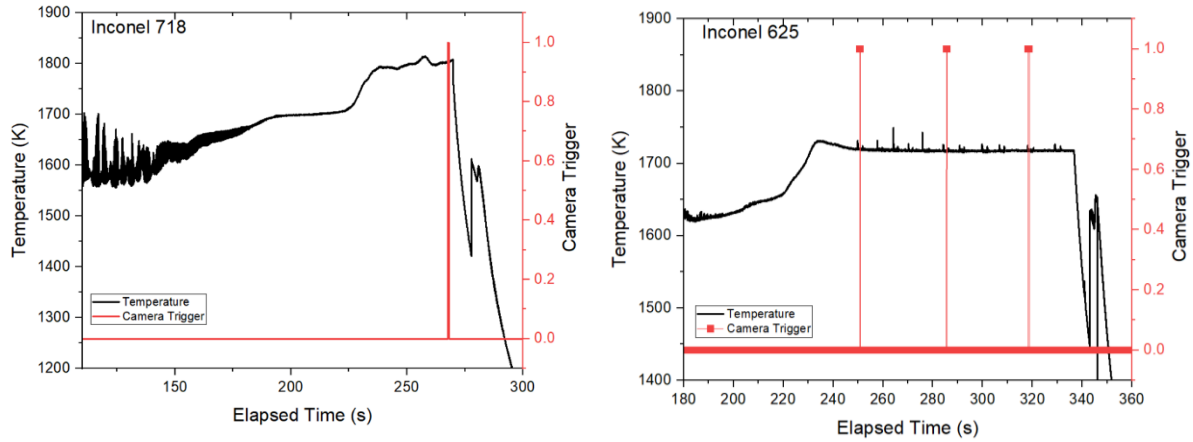

Figure 3: Thermal profiles for levitated alloy samples during density (left) and surface tension/viscosity (right) measurements, showing temperature evolution and camera trigger timing.

Surface tension measurements are conducted during an isothermal hold to ensure the sample remains at a stable and constant temperature. This is crucial because temperature fluctuations could influence the material's properties and the internal fluid flow, leading to inaccurate results. By holding the sample in an isothermal condition, oscillations can be accurately analysed without interference from temperature variations, ensuring reliable measurements of thermophysical properties.

2.3 Electromagnetic Levitation (EML) under Microgravity (ISS)

Electromagnetic Levitation (EML) under microgravity conditions, such as those aboard the International Space Station (ISS), allows for container-less processing of molten samples, eliminating the effects of gravity that can interfere with accurate measurements of thermophysical properties. The ISS-EML facility (Figure 4) is controlled remotely from the Microgravity User Support Center (MUSC) in Köln Germany by engineers from the German Aerospace Agency which is part of DLR, with remote telescience operations involving a series of automated preprogrammed steps to stabilize and manipulate samples.

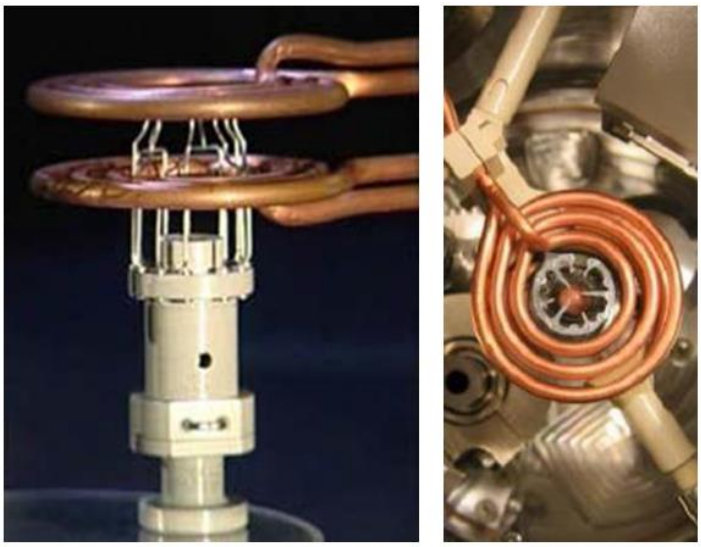

Figure 4: Electromagnetic Levitator (EML) on the ISS - photo courtesy of DLR [3]

In electromagnetic levitation (EML), a high frequency electromagnetic field is generated by water cooled copper coils to levitate and heat metallic samples at the same time. This containerless environment eliminates contamination and allows precise measurement of thermophysical properties such as surface tension, viscosity, and density. An important advantage of EML in microgravity, compared to ground based EML systems, is that heating and positioning can be controlled more independently. On Earth, strong electromagnetic forces are required to counteract gravity, which couples the heating power with the positioning force and makes independent adjustment difficult. In the microgravity environment of the International Space Station (ISS), only a small levitation force is needed, and this allows much finer control of temperature, sample shape, and oscillation behavior while greatly reducing convection and other disturbances that occur in Earth based experiments. The positioner coils still contribute a small amount of heating, but their effect is much lower, making ISS EML highly suitable for high precision thermophysical measurements [10].

During typical ISS experiments, samples weighing approximately 1 gram are preheated to just below the melting point before the electromagnetic fields are activated to melt and levitate the sample. The SUPOS coil system generates both positioning and heating fields to control the sample's stability and temperature. Once the sample reaches a superheated state (typically 50–70 °C above the melting point), cooling is regulated by reducing heater power, with cooling rates ranging from 25 to 70 °C/s. This controlled cooling helps prevent excessive evaporation and ensures precise measurements [11].

Surface tension and viscosity measurements are performed by inducing controlled oscillations in the sample via heaterpulses in the electromagnetic field. The oscillation frequencies, typically mode 2 oscillations, are monitored using high-speed cameras operating at 150–1000 fps, depending on the property being measured. The oscillation frequencies are then analysed to determine surface tension. Figure 5 present examplses of temperature, heater voltage, and positioning voltage profiles during ISS EML experiments, highlighting both heating and controlled cooling sequences [12].

One challenge during EML experiments in microgravity is the limited number of cycles that can be performed due to constraints in experimental time and resources. Motion damping is also crucial to control spinning of the sample, as unwanted motion can interfere with the precision of the measurements. While camera systems on the ISS capture essential data, transmission to Earth may occasionally be affected by bandwidth limitations or image corruption. Nonetheless, the ISS EML facility enables measurements that are impossible to achieve under Earth's gravitational conditions [13].

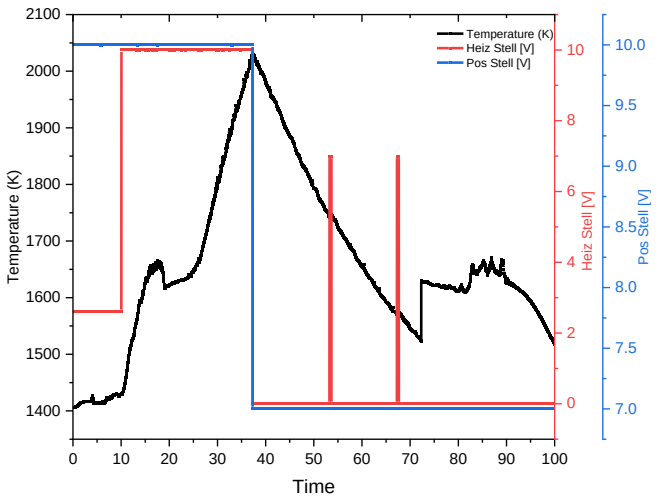

Figure 5: Temperature and voltage profiles during an ISS EML experiment, showing pyrometer-measured temperature (black), heating voltage U_{heat}(red), and positioning voltage U_{pos}(blue) as functions of time.

2.4 Parabolic Flight Experiments under Zero Gravity

Parabolic flight experiments simulate periods of near-zero gravity by flying aircraft in a parabolic trajectory, providing approximately 20-25 seconds of microgravity per parabola. These flights allow for container-less processing of molten materials using Electromagnetic Levitation (EML) to study thermophysical properties without the influence of gravity. The TEMPUS facility shown in Figure 6, operated by the German Aerospace Center (DLR), is used to perform these experiments aboard the "Zero-G" aircraft.

Figure 6: ESA parabolic aircraft and TEMPUS flight operations – photos courtesy of ESA and DLR

In each flight, the sample is preheated to just below its melting point (~1000°C) in a 20 mbar Argon atmosphere before the aircraft enters microgravity. Once the sample is free-floating, the SUPOS coil system is used to apply electromagnetic fields to melt and levitate the sample. After melting, the chamber is flooded with Helium to a pressure of 300 mbar to induce increased cooling, with cooling rates ranging between 25-70°C per second, depending on the heater setting and sample temperature. Induced convection within the droplet during cooling is maintained between 0.03 and 0.20 m/sec. Gas purity is maintained at less than 1 ppm O_2 and H_2O to prevent contamination [14].

High-speed cameras capture the behaviour of the molten droplet during these short periods of microgravity. The axial camera operates at 150 Hz, while the radial camera captures at 400 Hz. These cameras record the droplet's oscillations, which are induced by electromagnetic pulses, allowing for measurements of surface tension and viscosity [11]. The detailed heating,

levitation, oscillation, and cooling sequence for a Inconel 625 sample during a 2020 parabolic flight is shown in Figure 7, where heater voltage, acceleration in the z-direction, and sample temperature are tracked throughout the experiment.

One of the key challenges in parabolic flights is g-jitter, which refers to small residual accelerations during the transition into and out of microgravity. This jitter can cause unwanted mixed-mode oscillations in the droplet, affecting the precision of the measurements. To mitigate these effects, multiple parabolas are used during each flight, allowing data collection across several cycles. By selecting the cleanest oscillation patterns, we can ensure more accurate measurements.

Despite the short duration of the microgravity intervals, parabolic flight experiments provide crucial data on the behaviour of molten materials in near-zero gravity. These experiments complement ground-based and space-based studies by offering insights that help improve the understanding of thermophysical properties under reduced gravity conditions.

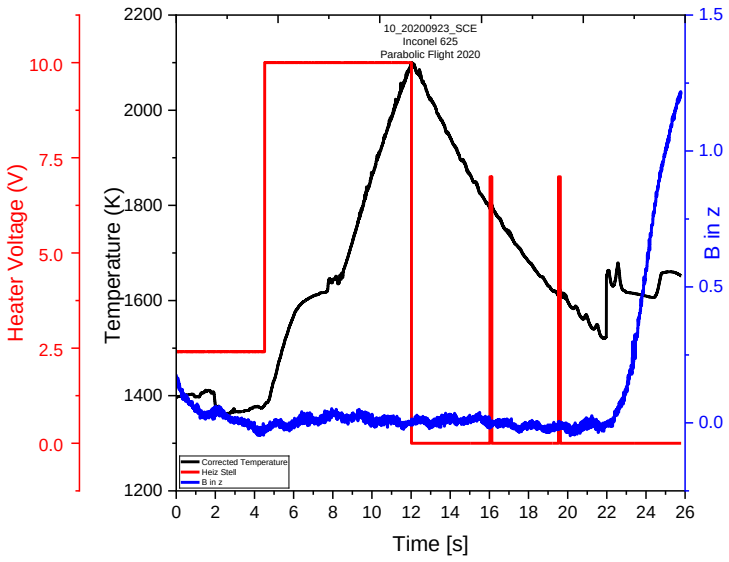

Figure 7: Parabolic flight EML experimental profile for Inconel 625, showing temperature (black), heater voltage (red), and magnetic field strength (blue) as functions of time.

2.5 Temperature Correction

Accurate temperature determination is critical for interpreting thermophysical property data obtained under containerless conditions. In levitation experiments, temperature is typically measured using a pyrometer directed at the droplet surface. However, due to emissivity variations, optical misalignment, and radiative heat losses, the apparent pyrometric temperature

(T_P) often deviates from the actual thermodynamic temperature of the sample. Therefore, a systematic temperature correction was applied to all datasets to ensure comparability across facilities and experimental campaigns.

$$\frac{1}{T} = \frac{1}{T_P} + \left(\frac{1}{T_L} - \frac{1}{T_{PL}}\right) \quad (1)$$

where

- T_P = pyrometer-measured temperature during the experiment,
- T_L = true liquidus temperature (from DSC),
- T_{PL} = observed liquidus temperature from the pyrometer during calibration.

This correction aligns the experimental temperature scale with the thermodynamic reference points, ensuring consistency between ESL and EML data acquired at different facilities. The term ($1/T_L - 1/T_{PL}$) represents the calibration offset that compensates for differences in sample emissivity and optical path length between experiments.

To further refine emissivity corrections, Planck's law-based adjustment was applied as [15]:

$$\frac{\varepsilon^S}{\varepsilon^L} = \exp\left[-\frac{C_2}{\lambda}\left(\frac{1}{T_1} - \frac{1}{T_2}\right)\right] \quad (2)$$

where $C_2 = 1.438 \times 10^4$ μm·K is the second radiation constant, λ is the pyrometer wavelength (0.90 μm for the MSFC ESL), and T_1 and T_2 correspond to the solidus and liquidus reference points, respectively. This approach minimizes temperature bias introduced by changing surface emissivity during melting and resolidification cycles.

2.6 Measurement of Thermophysical Properties

The thermophysical properties of high-chromium nickel-based alloys and their ternary analogs were measured using advanced levitation techniques mentioned above which provide containerless environments for high-accuracy measurements. The primary thermophysical properties measured in this study include density and surface tension.

2.6.1 Density Measurement

In this study, the measurement of density is conducted using non-contact methods that rely on high-speed video recordings to capture the sample's behavior, while temperature data is obtained via pyrometry.

The density (ρ) of a sample is defined as the ratio of its mass (m) to its volume (V). For molten alloys, the density changes with temperature due to thermal expansion. The relationship is typically expressed as:

$$\rho = \frac{m}{V} \tag{3}$$

Where ρ is the density, m is the mass of the sample, and V is the volume of the sample, calculated from the 2D area of the sample image, assuming spherical symmetry.

The calculation of droplet volume assumes that the liquid remains a perfect sphere throughout the experiment, yet several factors introduce small deviations from this idealized geometry. The imaging approach also assumes axial symmetry of the droplet because only a side view is used to extract the radius; a top view would be required to fully capture any asymmetry in the horizontal plane. The method further assumes that the radius obtained from 2D silhouettes is free of lens distortion, that the droplet is centered in the field of view, and that the camera plane is perfectly aligned with the droplet mid-plane. In practice, the levitation field can slightly elongate or flatten the droplet, and thermal gradients may produce anisotropic expansion, both of which alter the true volume. Additional effects such as minor mass loss during heating or thin oxide layers at the surface can also change the apparent radius without modifying the actual liquid volume. These assumptions primarily influence the accuracy of the volume term and therefore the calculated density, since density is directly proportional to m/V. Importantly, they do not affect the surface tension measurements because the natural oscillation frequency used to compute surface tension depends only on the deformation dynamics and is independent of the static radius.

In ground-based facilities, such as NASA MSFC, density measurements are obtained using high-speed video cameras that record at 1000 frames per second (fps). The volume of the molten sample is determined by analyzing the projected area of the sample in each frame, assuming an elliptical shape. Simultaneously, a pyrometer is used to record the temperature of the sample. The video data and pyrometer readings are synchronized to ensure accurate calculation of the temperature-dependent density. This approach is also used in microgravity environments, such as on Electromagnetic Levitation (EML) systems and during Parabolic Flights, where similar procedures are followed for density measurements.

In high-temperature environments, particularly in vacuum conditions like those used at NASA MSFC, molten samples can experience evaporation, leading to mass loss. This evaporation

must be accounted for in density calculations to ensure accurate results. The rate of evaporation is calculated using Langmuir's equation of evaporation, which tracks the dynamic mass loss over time:

$$m_i = \sum_{0}^{t} \sum_{i=1}^{m} \frac{\left(\gamma_i c_i P_{v,i} - P_{ref}\right)\alpha_i A_i}{\sqrt{(2\pi M_i RT)}} \Delta t \tag{4}$$

where m_i is mass loss at time t, γ is activity coefficient, P_v is vapor pressure, P_{ref} is reference pressure, α is correction factor, M is molecular mass, R is universal gas constant and T is surface temperature.This equation allows for real-time tracking of mass loss during the experiment, ensuring that the density measurements reflect the correct mass of the sample after accounting for any evaporated material [16].

For the purposes of this study, density is considered to vary linearly with temperature. This relationship can be expressed as:

$$\rho(T) = \rho_m + \frac{d\rho}{dT}(T - T_m) \tag{5}$$

Where ρ(T) is the density at temperature T, ρ_m is the density at the melting temperature T_m, and $\frac{d\rho}{dT}$ is the rate of change of density with respect to temperature. This linear behavior is observed as the sample cools, and by correlating the volume measurements from the video frames with the temperature data, the density can be accurately determined as a function of temperature.

2.6.2 Surface Tension Measurement

Surface tension was determined using the droplet oscillation technique, which measures the natural oscillation frequency of a molten droplet levitated in a containerless environment. The method combines controlled droplet excitation, frequency identification, and analytical calculation to relate oscillation behavior to surface tension. The following subsections describe the procedures used to generate droplet oscillations, determine their natural frequencies, and calculate the corresponding surface tension values.

2.6.2.1 Droplet Oscillation Technique

The droplet oscillation method involves levitating a molten droplet using electromagnetic levitation (EML) or electrostatic levitation (ESL) techniques, which allow the sample to be

suspended in a containerless environment. In ESL, a sinusoidal voltage is briefly applied to the levitation field, exciting the droplet into oscillation. Once the external excitation is removed, the droplet continues to oscillate freely, and its motion gradually decays due to the combined effects of surface tension and viscosity as shown in Figure 8 below.

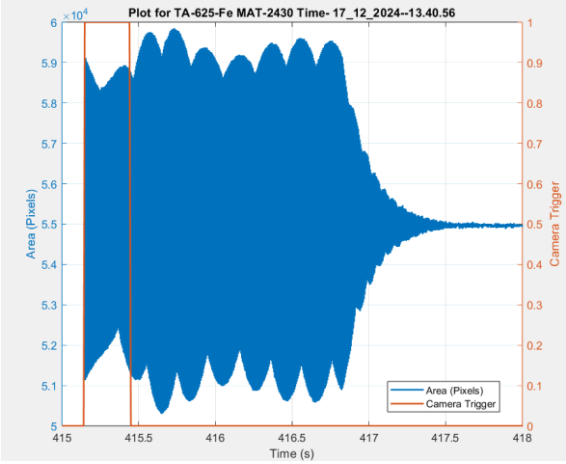

Figure 8: Droplet Oscillation Gradual Decay

In EML, the heater circuit is turned on until the sample reaches the melting plateau, at which point the heater is turned off to allow the sample to cool. During the cooling process, one or more heater pulses are applied to excite the sample and induce oscillation (Figure 7).

The oscillations of the molten droplet are recorded using high speed cameras, and the natural frequency of these oscillations is extracted from the time dependent radius signal. The natural frequency $\omega_l$depends on the surface tension γ, the density ρ, and the unperturbed radius $r_0$of the droplet. In an electrostatic levitation (ESL) system, the natural frequency is described by a modified form of Rayleigh's classical equation that includes an additional correction for the electrostatic surface charge. The expression used is:

$$\omega_l^2 = l(l-1)(l+2)\frac{\gamma}{\rho {r_0}^3}\left(1 - \frac{Q_s}{64\pi^2 {r_0}^3 \sigma \epsilon_0}\right) \quad (6)$$

Where l is the mode number of oscillations, Q_s is the surface charge, and ϵ_0 is the permittivity of free space [17]. For this study, mode l = 2 was selected, as it represents the axisymmetric oscillations of the droplet (Figure 9). The correction term for surface charge is typically small for liquid samples and was therefore neglected in this study to simplify the analysis. Mode l = 1 was also excluded, as it describes the translational movement of the droplet rather than oscillatory behavior. Thus, the simplified version of the equation for mode l = 2 becomes:

$$\omega_2^2 = (2\pi f_n)^2 = \frac{8\gamma}{\rho {r_0}^3} \tag{7}$$

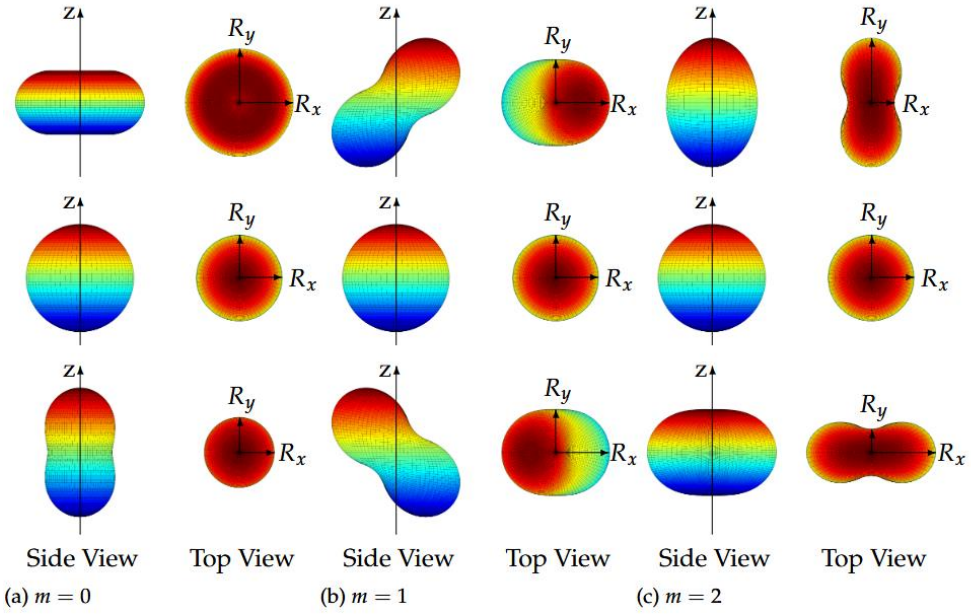

Figure 9: Simulated droplet oscillation shapes for modes [18]

2.6.2.2 Faraday Forcing Method

To accurately measure the natural oscillation frequency of the molten droplet, the Faraday forcing method was employed. This technique involves continuous parametric excitation of the droplet using an electrostatic field, in which the droplet is driven at a fixed amplitude while the excitation frequency is swept over a range that includes the expected natural frequency. As the excitation frequency approaches the natural frequency of the droplet, the oscillation amplitude increases significantly, allowing the natural frequency to be identified [19]. Figure 10 below shows an example of the Faraday Forcing method being used for TA 718-Ni sample. In Figure 10 you see excitation frequencies that were applied from 180Hz to 187Hz, and the natural frequency can be seen to be around 184Hz were the oscillation amplitude increased significantly.

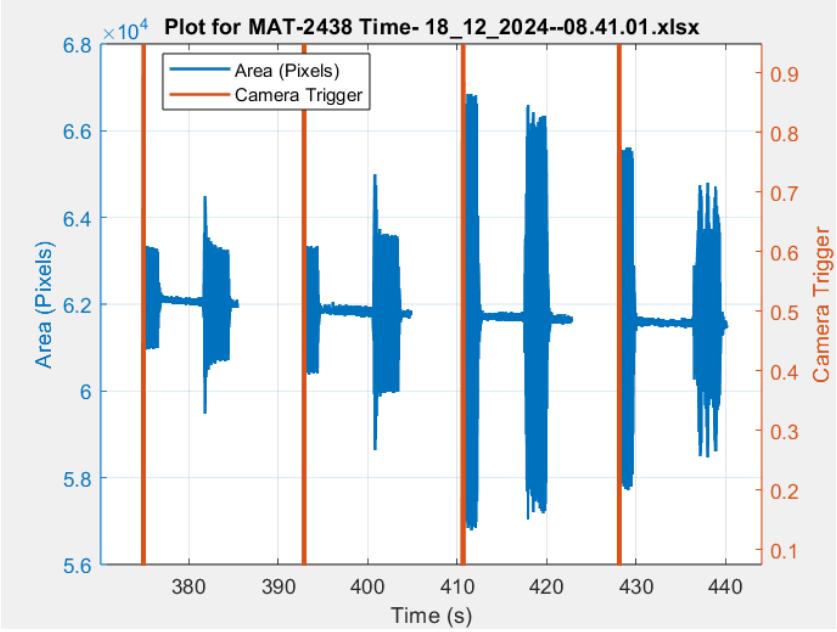

Figure 10: Faraday Forcing Method applied to TA 718-Ni

This method offers significant advantages over the traditional pulse decay method, which involves exciting the droplet once and allowing it to oscillate until the motion decays. The Faraday forcing method eliminates the need to identify the natural frequency by post-processing the decaying oscillation signal. It also minimizes interference from feedback systems and noise, as the natural frequency is observed directly during the excitation process.

2.6.2.3 Frequency Identification in Signal Processing

Accurate frequency identification is critical for determining dominant oscillations in a signal. Bandpass filtering is first applied to isolate the relevant frequency band and suppress noise. As shown in Figure 11, local maxima and minima can be identified in the filtered signal to extract the oscillation period. Three methods are commonly used:

(i) inverted period measurement, where the average interval between successive peaks or troughs gives the mean period and frequency $f = 1/T$;

(ii) cycle counting, where the number of complete oscillations within a defined time frame (T) yields the frequency $f = N/T$; and

(iii) Fast Fourier Transform (FFT), which converts the signal into the frequency domain and identifies the dominant frequency from the power spectrum [19].

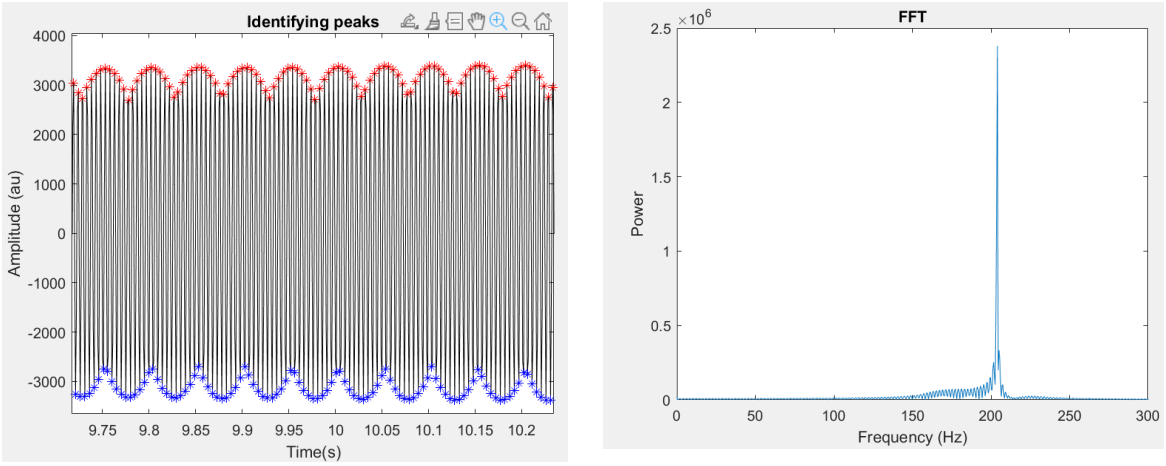

Figure 11: Peak detection (left) of maxima (red) and minima (blue) with corresponding FFT spectrum (right).

In ESL experiments, frequency identification was closely tied to oscillation behavior. The system initially oscillates in a forced region (Figure 12), where motion is dictated by the excitation frequency, reaching maximum amplitude when resonance with the natural frequency occurs. Once excitation ceases, the oscillations enter the damped region (Figure 12), where amplitude decays at a rate defined by the damping coefficient.

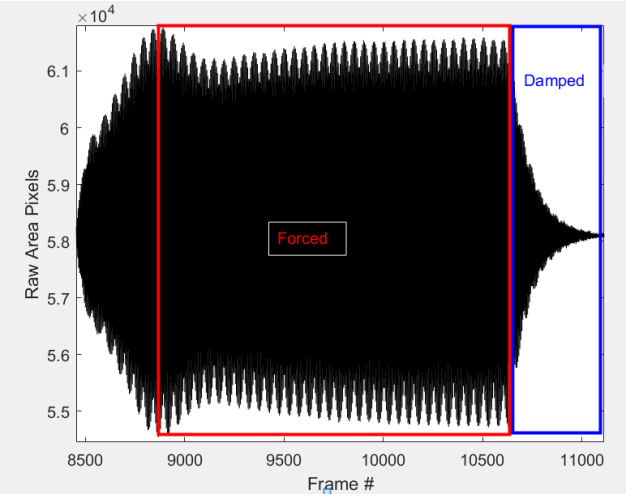

Figure 12: Signal Segmentation into Forced Excitation and Damped Decay Phases

Once the natural frequency (f_n) is determined, the surface tension (γ) can be calculated using the following equation:

$$\gamma = \frac{3\pi m f_n^2}{8} \tag{8}$$

Where γ is the surface tension, m is the mass of the droplet, and f_n is the natural oscillation frequency. The calculated surface tension values for some few alloys runs under different experimental conditions are summarized in Appendix C, which lists the corresponding liquidus

temperature, hold temperature, measured frequency, droplet mass, and resulting surface tension.

2.7 Sources of Error and Considerations

There are several factors that can influence the accuracy of surface tension measurements in droplet oscillation experiments:

i. Modulation due to Sample Movement:
   Any translational motion of the droplet can cause noise in the oscillation signal, leading to errors in determining the natural frequency. This issue was mitigated by using a bandpass filter and by carefully controlling the droplet's position.

ii. Evaporation:
   At elevated temperatures, molten samples are susceptible to evaporation, leading to measurable mass loss. This loss can alter oscillation dynamics and thereby affect the accuracy of surface tension measurements. In this study, evaporation effects were mitigated by continuously monitoring the sample mass, with losses maintained below 5% during analysis. The <5% mass-loss limit is used because evaporation below this level has negligible effect on droplet size and oscillation frequency, keeping surface-tension measurements accurate. Above ~5%, radius changes begin to distort the oscillation modes and introduce error, so staying under this threshold preserves the constant-volume assumption. A more detailed treatment of evaporation phenomena in levitation experiments is provided by Nawer et al. [18].

iii. Noise from Electronics and Optical Components:
   Noise generated by the data acquisition system and optical components can interfere with the measurement of the oscillation signal. This was minimized through careful calibration of the system and the use of filters during data processing [12].

2.8 Chapter Summary

This chapter detailed the preparation of Ni-Cr-Fe and Ni-Cr-Mo based ternary alloy samples and their investigation under containerless conditions using ESL and EML facilities. Density and surface tension were evaluated through droplet oscillations, with natural frequencies identified using multiple methods, including period measurement, cycle counting, FFT, Maximum Amplitude (MA), and Frequency Crossover (COF). Key experimental challenges such as evaporation, sample motion, and noise were addressed with corrective measures.

CHAPTER 3. Thermodynamic Modelling

3.1 Introduction

This chapter presents the thermodynamic modelling approaches used to describe the liquid-state properties of metallic alloys. Two fundamental quantities are considered: density, expressed through molar excess volume in binary and ternary systems, and surface tension, described using the Butler Model. Together, these models establish the theoretical foundation for interpreting the experimental data in later chapters.

3.2 Theoretical Framework for Density Modelling

To interpret the density measurements presented in this chapter, it is necessary to establish the thermodynamic framework upon which the analysis is based. The Gibbs free energy, *G*, provides the starting point for such a description, as it represents the most fundamental thermodynamic potential for systems held at constant temperature and pressure. Its general form is expressed as [3]:

$$dG = Vdp - SdT \tag{9}$$

where *V* denotes the volume, *p* the pressure, *S* the entropy, and *T* the temperature. From this relation, it is evident that, at constant temperature, the Gibbs free energy increases proportionally with pressure. This is formally represented by:

$$\left(\frac{\partial G}{\partial p}\right)_T = V \tag{10}$$

Equation (10) provides a direct link between the Gibbs free energy and the molar volume of a system, thereby making it particularly useful when analysing density data for both pure substances and multicomponent alloys.

When considering a multicomponent mixture, the Gibbs free energy is no longer a simple summation of its constituents. Instead, the free energy of such a system may be expressed as:

$$G = \sum_i x_i \, G_i^0 + \Delta G \tag{11}$$

where x_i is the mole fraction of component *i*, G_i^0 is the Gibbs free energy of the pure component $_i$, ΔG is the free energy associated with mixing. This mixing free energy is related to the enthalpy of mixing ΔH_{mix} and the entropy of mixing ΔS_{mix}:

$$\Delta G = \Delta H_{mix} - T\Delta S_{mix} \tag{12}$$

In an ideal solution, the enthalpy of mixing vanishes ($\Delta H_{mix} = 0$) leading to:

$$\Delta G^{id} = RT \sum_i x_i \ln (x_i) \tag{13}$$

In real systems, however, mixing can either absorb (endothermic) or release (exothermic) heat [3]. Deviations from ideal behaviour are accounted for by an excess free energy term G^E. The free energy of mixing in a regular solution thus becomes:

$$\Delta G = \Delta G^{id} + G^E = RT \sum_i x_i \ln (x_i) + G^E \tag{14}$$

Substituting into Eq. (11) yields the molar volume expression [3]:

$$V = \sum_i x_i V_i + V^E \tag{15}$$

Here, V_i is the molar volume of the pure component *i*, and V^E is the molar excess volume. This indicates that, unlike mass or mole count, the total molar volume of a mixture is not strictly additive because particle interactions contribute an additional term.

3.2.1 Binary Systems

For binary alloys, the description of non-ideal mixing behaviour is most frequently achieved using the Redlich–Kister polynomial expansion [20]. The excess free energy in such a system is written as:

$$G^E = x_i x_j \sum_v L_{i,j}^{(v)} (T)(x_i - x_j)^v \tag{16}$$

Here, $L_{i,j}^{(v)}$ is the binary interaction parameter between components *i* and *j*, and the summation accounts for higher-order terms in the composition dependence. Using the thermodynamic relation in Eq. (14), a corresponding expression can be obtained for the excess molar volume. For most binary metallic alloys, it is often sufficient to truncate the expansion after the zeroth-order term, yielding the parabolic approximation [3]:

$$V_{i,j}^E \approx x_i x_j V^0(T) \tag{17}$$

This parabolic dependence on composition is commonly observed in experimental density measurements of binary mixtures and provides an effective first-order description of non-ideal mixing effects.

3.2.2 Ternary Systems

The treatment of ternary alloys builds naturally upon the binary case but requires additional terms to capture three-body interactions. The Redlich–Kister–Muggianu formalism provides a convenient framework for this purpose [20]. The excess free energy in a ternary system may be expressed as:

$$G^E = \sum_{i<j} x_i x_j \sum_v L_{i,j}^{(v)}(T)(x_i - x_j)^v + G^T(T, x_1, x_2, x_3) x_1 x_2 x_3 + \cdots \quad (18)$$

In this expression, the first summation accounts for binary contributions embedded within the ternary system, while the parameter G^T introduces an explicit ternary interaction term. Applying the same procedure used for binary alloys leads to an analogous relation for the excess molar volume:

$$V_{1,2,3}^E = \overbrace{\sum_{i<j} V_{i,j}^E(T)}^{\text{binary term}} + \overbrace{V^T x_1 x_2 x_3}^{\text{ternary term}} \quad (19)$$

The binary terms $V_{i,j}^E$ can be determined directly from Eq. (17), while the ternary contribution, V^T, accounts for deviations arising from three-body interactions. In many cases, however, the ternary term is found to be small ($G^T \approx 0$), such that the excess properties of the ternary system can be effectively deduced from the properties of its binary subsystems [3].

For a single phase the density is defined by the mass *m* divided by the volume *V*. Respecting the previous derivations, for a mixture consisting of *i* components with molar masses M_i and mole fractions x_i the density can be written as:

$$\rho = \frac{\sum_i x_i M_i}{\sum_i x_i \frac{M_i}{\rho_i} + V^E} \quad (20)$$

with $\rho_i = M_i / V_i$ being the density of the pure component *i*. This relation forms the thermodynamic basis for the Partial Molar Volume (PMV) model employed in this study for both Ni–Cr–Fe and Ni–Cr–Mo alloy systems.

3.2.3 Density Modelling Methodology

To quantitatively interpret the experimental density data obtained from levitation measurements, a Partial Molar Volume (PMV) framework was employed to compute the temperature-dependent density of the Ni–Cr–Fe and Ni–Cr–Mo ternary alloy systems. The PMV model provides a physically grounded means of relating the molar mass, partial molar volume, and excess volume of mixing to the macroscopic density of a multicomponent liquid.

A. Model Formulation

Following the thermodynamic derivation presented in section above, the density of a multicomponent alloy can be re-expressed as:

$$\rho_{\text{mix}}(T) = \frac{\sum_i x_i M_i}{\sum_i x_i V_i(T) + V^E(T,x)} \tag{21}$$

where:

- x_i= mole fraction of element i,
- M_i= molar mass (kg mol^{-1}),
- $V_i(T)$= temperature-dependent molar volume of the pure liquid element,
- V^E= excess molar volume accounting for non-ideal mixing effects.

The partial molar volume of each element was modelled as a linear function of temperature:

$$V_i(T) = V_{0,i}\,[1 + \alpha_i(T - T_{\text{ref},i})] \tag{22}$$

where $V_{0,i}$is the reference molar volume (at $T_{\text{ref},i}$), and $\alpha_i$is the volumetric expansion coefficient. All constants were taken from Table 3 and correspond to the liquid state near the respective melting points of Fe, Cr, Ni, and Mo.

B. Ideal and Non-Ideal Mixing Models

Two PMV variants were implemented:

a) Ideal Mixing Model ($V^E = 0$)

In the ideal approximation, the total mixture volume is purely additive:

$$V_{\text{mix}}^{\text{ideal}}(T) = \sum_i x_i V_i(T) \tag{23}$$

and the density follows directly as

$$\rho_{\text{mix}}(T) = \frac{\sum_i x_i M_i}{\sum_i x_i V_i(T)} \tag{24}$$

This model assumes no volumetric deviation from ideality and was applied to all four ternary analog alloys as a baseline (Appendix F, *TernaryAnalogs_Density_PMV_Ideal.m*).

b) Non-Ideal Mixing Model ($V^E \neq 0$)

For Ni–Cr–Fe alloys, an excess molar volume term was incorporated as a first-order Redlich–Kister form:

$$V^E(T,x) = x_{\text{Fe}} x_{\text{Cr}} V^{\text{FeCr}} + x_{\text{Fe}} x_{\text{Ni}} V^{\text{FeNi}} + x_{\text{Cr}} x_{\text{Ni}} V^{\text{CrNi}} \tag{25}$$

where the V^{ij}coefficients (in m³ mol⁻¹) correspond to constant binary excess volumes derived from Brillo [21] and converted from cm³ mol⁻¹:

$V^{\text{FeCr}} = 0.28 \times 10^{-6}$,
$V^{\text{FeNi}} = 0.51 \times 10^{-6}$,
$V^{\text{CrNi}} = 0.74 \times 10^{-6}$.

The inclusion of these terms increases V^E, resulting in a slight decrease in predicted density relative to the ideal case. This formulation was implemented in *FeCrNi_PMV_Export.m* (Appendix G).

For Ni–Cr–Mo alloys (TA-625Mo), experimental and thermodynamic data on excess volumes remain limited; therefore, the ideal PMV formulation was used ($V^E = 0$).

3.3 Theoretical Framework for Surface Tension Modelling

This section introduces the thermodynamic models used in this study to predict the surface tension of multicomponent liquid solutions, with particular emphasis on nickel-based alloys. These models extend the general principles of thermodynamics to incorporate interfacial phenomena by treating the surface as a distinct thermodynamic phase. The discussion begins with the Conventional Butler Model and its application to binary alloys, followed by its extension to ideal and regular solutions, and finally to ternary alloy systems.

The approaches adopted here are largely based on the work of Kaptay and others, who refined the Butler framework by introducing the concept of partial surface area. This parameter allows the influence of atomic coordination and interfacial segregation to be more accurately quantified, making the model especially useful for predicting surface properties of technologically relevant alloy systems.

3.3.1 Conventional Binary Butler Model

The Butler Model has long served as a foundational tool for describing the surface tension of liquid alloys. Unlike Gibbs' unified treatment of surface tension as a derivative of free energy, the Butler Model treats the surface as a separate thermodynamic phase characterized by its own composition and chemical potential. The model assumes equilibrium between surface and bulk phases, enabling the systematic derivation of relationships between their properties.

The equilibrium condition for the chemical potential of component *i* in the surface and bulk phases introduces an additional surface-specific term to the chemical potential expression. To capture the reduction in atomic coordination at the interface, a coordination factor β (where $0 < \beta \leq 1$) is introduced.

For a binary liquid solution, A–B, the resulting expression for the surface tension is [22]:

$$\gamma(T) = \gamma_{\mathrm{A}} + \frac{RT}{S_{\mathrm{A}}} \ln\left(\frac{a_A^S}{a_A^B}\right) = \gamma_{\mathrm{B}} + \frac{RT}{S_{\mathrm{B}}} \ln\left(\frac{a_B^S}{a_B^B}\right) \tag{26}$$

where:

$\gamma_{\mathrm{A}}$and γ_{B} are the surface tension of pure components A and B,

S_{A} and S_{B} are the molar surface areas of A and B,

a_A^S and a_B^S are the activities of A and B in the surface phase,

a_A^B and a_B^B are the activities of A and B in the bulk phase.

To account for non-ideal interactions, the surface tension equation may be extended by introducing excess Gibbs free energy contributions:

$$\gamma(T) = \gamma_{\mathrm{A}} + \frac{RT}{S_{\mathrm{A}}} \ln\left(\frac{x_A^S}{x_A^B}\right) + \frac{1}{S_{\mathrm{A}}} (G_A^{E,S}(T, x_i^S) - G_A^{E,B}(T, x_i^B)) \tag{27}$$

Here, $G_A^{E,S}$ and $G_A^{E,B}$ denote the excess Gibbs free energies of component *A* in the surface and bulk phases, respectively. The surface excess Gibbs free energy is modelled by [22]:

$$G_A^{E,S} = \beta \sum_{i<j} x_i^S x_j^S \sum_{v} L_{i,j}^{(v)}\,(T)\left(x_i^S - x_j^S\right)^v \tag{28}$$

Where $L_{i,j}^{(v)}$ are the binary interaction parameters, and β is the coordination factor (commonly set to 0.83, 0.75, or 1) [12].

3.3.2 Ideal and Regular Solution Model

The distinction between ideal and regular solutions is critical in applying the Butler framework.

A. Ideal solutions [23]**:**

- ($\Delta H_{mix} = 0$) and ($G^E = 0$).
- Mixing is driven purely by entropy.
- The surface tension equation reduces to:

$$\gamma = \gamma_A + \frac{RT}{S} ln\left(\frac{x_A^S}{x_A^B}\right) = \gamma_B + \frac{RT}{S} ln\left(\frac{1 - x_B^S}{1 - x_B^B}\right) \tag{29}$$

with equal molar surface areas $S_A = S_B = S$.

The surface mole fraction of component A x_A^S can be analytically expressed as:

$$x_A^S = \frac{x_A^B}{x_A^B + (1 - x_A^B)S_e(T)} \tag{30}$$

where the segregation factor S_e is defined as:

$$S_e = \exp\left(\frac{(\gamma_A - \gamma_B)S}{RT}\right) \tag{31}$$

This segregation factor reflects the natural tendency of the component with lower surface tension to enrich at the interface, thereby minimizing the system's free energy.

B. Regular solutions [23]**:**

- ($\Delta H_{mix} \neq 0$) and ($G^E \neq 0$).
- Excess Gibbs free energy terms in Eq. (19) remain active.
- First-order terms ($v = 1$) of the Redlich–Kister expansion are usually sufficient.
- Segregation behavior reflects both entropic and enthalpic contributions.

3.3.3 Segregation Effects

Segregation is the preferential enrichment of one component at the liquid surface. It occurs because the system minimizes its total free energy by enriching the surface with the component of lower surface tension.

- In ideal solutions, segregation is entropy-driven and controlled by surface tension differences.
- In regular solutions, segregation is amplified (or suppressed) by enthalpy of mixing and excess Gibbs free energy contributions.

This framework explains why alloys with large surface tension mismatches exhibit stronger surface segregation and why the effects are composition- and temperature-dependent [24].

3.3.4 Extension to Ternary Alloys

As seen before, the expanded formulation of the Butler Model for binary alloys is expressed as:

$$\gamma_{\mathrm{FeNi}}(T) \begin{aligned} &= \gamma_{\mathrm{Fe}} + \frac{RT}{S_{\mathrm{Fe}}} \ln\left(\frac{1-x_{\mathrm{Ni}}^{S}}{1-x_{\mathrm{Ni}}^{B}}\right) + \frac{1}{S_{\mathrm{Fe}}}\left\{G_{Fe}^{E,S}\left(T, x_i^{S}\right) - G_{Fe}^{E,B}\left(T, x_i^{B}\right)\right\} \\ &= \gamma_{\mathrm{Ni}} + \frac{RT}{S_{\mathrm{Ni}}} \ln\left(\frac{x_{\mathrm{Ni}}^{S}}{x_{\mathrm{Ni}}^{B}}\right) + \frac{1}{S_{\mathrm{Ni}}}\left\{G_{Ni}^{E,S}\left(T, x_i^{S}\right) - G_{Ni}^{E,B}\left(T, x_i^{B}\right)\right\} \end{aligned} \quad (32)$$

where R is the universal gas constant, T is the temperature, S_i is the surface area in a monolayer of pure liquid i, x_i^{B} is the mole fraction of component i in the bulk phase, and x_i^{S} is the mole fraction of component i in the surface phase. $G_i^{E,B}$ denotes the partial excess Gibbs free energy in the bulk and $G_i^{E,S}$ the partial excess Gibbs free energy of component i in the surface layer.

For ternary alloys, the expanded model becomes [25]:

Fe based (33)

$$\gamma_{\mathrm{FeCrNi}}(T) \begin{aligned} &= \gamma_{\mathrm{Fe}} + \frac{RT}{S_{\mathrm{Fe}}} \ln\left(\frac{1-x_{\mathrm{Cr}}^{S}-x_{\mathrm{Ni}}^{S}}{1-x_{\mathrm{Cr}}^{B}-x_{\mathrm{Ni}}^{B}}\right) + \frac{1}{S_{\mathrm{Fe}}}\left\{G_{Fe}^{E,S}\left(T, x_i^{S}\right) - G_{Fe}^{E,B}\left(T, x_i^{B}\right)\right\} \\ &= \gamma_{\mathrm{Cr}} + \frac{RT}{S_{\mathrm{Cr}}} \ln\left(\frac{x_{\mathrm{Cr}}^{S}}{x_{\mathrm{Cr}}^{B}}\right) + \frac{1}{S_{\mathrm{Cr}}}\left\{G_{Cr}^{E,S}\left(T, x_i^{S}\right) - G_{Cr}^{E,B}\left(T, x_i^{B}\right)\right\} \\ &= \gamma_{\mathrm{Ni}} + \frac{RT}{S_{\mathrm{Ni}}} \ln\left(\frac{x_{\mathrm{Ni}}^{S}}{x_{\mathrm{Ni}}^{B}}\right) + \frac{1}{S_{\mathrm{Ni}}}\left\{G_{Ni}^{E,S}\left(T, x_i^{S}\right) - G_{Ni}^{E,B}\left(T, x_i^{B}\right)\right\} \end{aligned}$$

Cr-based

$$
\begin{aligned}
&= \gamma_{\mathrm{Fe}} + \frac{RT}{S_{\mathrm{Fe}}} \ln\left(\frac{x_{\mathrm{Fe}}^{S}}{x_{\mathrm{Fe}}^{B}}\right) + \frac{1}{S_{\mathrm{Fe}}}\left\{G_{Fe}^{E,S}\left(T, x_i^{S}\right) - G_{Fe}^{E,B}\left(T, x_i^{B}\right)\right\} \\
\gamma_{\mathrm{FeCrNi}}(T) \quad &= \gamma_{\mathrm{Cr}} + \frac{RT}{S_{\mathrm{Cr}}} \ln\left(\frac{1 - x_{\mathrm{Fe}}^{S} - x_{\mathrm{Ni}}^{S}}{1 - x_{\mathrm{Fe}}^{B} - x_{\mathrm{Ni}}^{B}}\right) + \frac{1}{S_{\mathrm{Cr}}}\left\{G_{Cr}^{E,S}\left(T, x_i^{S}\right) - G_{Cr}^{E,B}\left(T, x_i^{B}\right)\right\} \\
&= \gamma_{\mathrm{Ni}} + \frac{RT}{S_{\mathrm{Ni}}} \ln\left(\frac{x_{\mathrm{Ni}}^{S}}{x_{\mathrm{Ni}}^{B}}\right) + \frac{1}{S_{\mathrm{Ni}}}\left\{G_{Ni}^{E,S}\left(T, x_i^{S}\right) - G_{Ni}^{E,B}\left(T, x_i^{B}\right)\right\}
\end{aligned}
$$

Ni-based

$$
\begin{aligned}
&= \gamma_{\mathrm{Fe}} + \frac{RT}{S_{\mathrm{Fe}}} \ln\left(\frac{x_{\mathrm{Fe}}^{S}}{x_{\mathrm{Fe}}^{B}}\right) + \frac{1}{S_{\mathrm{Fe}}}\left\{G_{Fe}^{E,S}\left(T, x_i^{S}\right) - G_{Fe}^{E,B}\left(T, x_i^{B}\right)\right\} \\
\gamma_{\mathrm{FeCrNi}}(T) \quad &= \gamma_{\mathrm{Cr}} + \frac{RT}{S_{\mathrm{Cr}}} \ln\left(\frac{x_{\mathrm{Cr}}^{S}}{x_{\mathrm{Cr}}^{B}}\right) + \frac{1}{S_{\mathrm{Cr}}}\left\{G_{Cr}^{E,S}\left(T, x_i^{S}\right) - G_{Cr}^{E,B}\left(T, x_i^{B}\right)\right\} \\
&= \gamma_{\mathrm{Ni}} + \frac{RT}{S_{\mathrm{Ni}}} \ln\left(\frac{1 - x_{\mathrm{Cr}}^{S} - x_{\mathrm{Fe}}^{S}}{1 - x_{\mathrm{Cr}}^{B} - x_{\mathrm{Fe}}^{B}}\right) + \frac{1}{S_{\mathrm{Ni}}}\left\{G_{Ni}^{E,S}\left(T, x_i^{S}\right) - G_{Ni}^{E,B}\left(T, x_i^{B}\right)\right\}
\end{aligned}
$$

The Butler model can be written in several algebraic forms, described as Fe based, Cr based, or Ni based expressions in Eqn. 33. All these forms represent the same thermodynamic condition, which is that the chemical potential of each element at the surface must equal the chemical potential of that element in the bulk. The differences between the expressions come only from algebraic rearrangement of the mole fraction relation that the surface fractions of Fe, Cr, and Ni must sum to one. These rearrangements do not change the physics of the model.

When any two of the three Butler equations are solved together with the composition constraint, the results for the surface tension and the surface mole fractions are identical. The numerical solution is therefore independent of the chosen reference element. This means that the form used in this work is fully equivalent to the longer expanded form, and there is no difference in the predicted surface tension that comes from selecting an Fe based, Cr based, or Ni based version of the Butler model.

3.3.5 Surface Tension Modelling Methodology

The Butler model was implemented to calculate the temperature-dependent surface tension and surface compositions of Ni–Cr–Fe and Ni–Cr–Mo ternary analog alloys. This approach establishes thermodynamic equilibrium between bulk and surface phases based on chemical potential balance, incorporating both ideal and excess Gibbs energy contributions. The model accounts for temperature-dependent surface tension, molar volume, and binary interactions derived from CALPHAD assessments, allowing a physically consistent prediction of surface

segregation and liquid surface tension across the composition range of interest. The MATLAB code for implementation of this computation is found in Appendix H and Appendix I.

1. **Concentration Range Definition**

The ternary alloy systems investigated include Ni–Cr–Fe and Ni–Cr–Mo, which correspond to simplified analogs of the industrial superalloys Inconel 718 and Inconel 625, respectively. Each system satisfies the bulk compositional constraint:

$$\sum_i x_i^{bulk} = 1 \tag{34}$$

The Ni–Cr–Fe system included three compositions representative of analog alloys:

- TA-625Fe: $x_{\mathrm{Fe}} = 0.05$, $x_{\mathrm{Cr}} = 0.26$, $x_{\mathrm{Ni}} = 0.69$
- TA-718Ni: $x_{\mathrm{Fe}} = 0.20$, $x_{\mathrm{Cr}} = 0.22$, $x_{\mathrm{Ni}} = 0.58$
- TA-718Fe: $x_{\mathrm{Fe}} = 0.34$, $x_{\mathrm{Cr}} = 0.18$, $x_{\mathrm{Ni}} = 0.48$

For the Ni–Cr–Mo system, a single Ni-rich alloy was modeled:

- TA-625Mo: $x_{\mathrm{Ni}} = 0.69$, $x_{\mathrm{Cr}} = 0.26$, $x_{\mathrm{Mo}} = 0.05$

All alloys were evaluated over the liquid-state temperature range 1500–1900 K in 50 K intervals.

2. Temperature-Dependent Pure Element Properties

For each constituent element ($i =$ Fe, Cr, Ni, Mo), the surface tension (γ_i) and molar volume (V_i) were expressed as temperature-dependent functions:

$$\gamma_i(T) = {\gamma_i}^L + \frac{d\gamma}{dT}(T - T_L) \tag{35}$$

$$V_i(T) = {V_i}^L[1 + \alpha_i(T - T_L] \tag{36}$$

where T_L is the liquidus temperature, γ_i^L is the surface tension at T_L, and α_i is the volumetric thermal expansion coefficient. These parameters were taken from Table 3, which lists the liquid-state constants for Fe, Ni, Cr, and Mo.

Table 3: Partial molar volumes for Fe, Ni, Cr and Mo.

Element	T_{L}(K)	$\gamma_i(\mathrm{N \cdot m^{-1}})$	$V_i(\mathrm{m^3 \cdot mol^{-1}})$	Ref.
Fe	1808	$1.872 + [-0.49 \times 10^{-3}(T - T_{\mathrm{L}})]$	$7.94 \times 10^{-6}[1 + 1.30 \times 10^{-4}(T - T_{\mathrm{L}})]$	[26]
Ni	1728	$1.778 + [-0.38 \times 10^{-3}(T - T_{\mathrm{L}})]$	$7.43 \times 10^{-6}[1 + 1.51 \times 10^{-4}(T - T_{\mathrm{L}})]$	[26]
Cr	2178	$1.700 + [-0.32 \times 10^{-3}(T - T_{\mathrm{L}})]$	$8.27 \times 10^{-6}[1 + 1.10 \times 10^{-4}(T - T_{\mathrm{L}})]$	[26]
Mo	2895	$2.250 + [-0.30 \times 10^{-3}(T - T_{\mathrm{L}})]$	$10.30 \times 10^{-6}[1 + 0.53 \times 10^{-4}(T - T_{\mathrm{L}})]$	[26]

The molar surface area S_i for each component was calculated using Avogadro's number (N_A) following Eq. (30):

$$S_i = 1.091\ \mathrm{N_A^{\frac{1}{3}}} V_i^{\frac{2}{3}} \tag{37}$$

3. Excess Gibbs Free Energy of Mixing

Temperature-dependent expressions for binary systems Fe–Ni, Fe–Cr, and Ni–Cr were taken from CALPHAD-based assessments (Table 4).

Thermodynamic non-ideality within the molten ternary alloys was incorporated through Redlich–Kister binary interaction models for each pair of elements. The excess Gibbs energy for the bulk phase was expressed as:

$$G_i^{E,B} = x_A^{\mathrm{bulk}} x_B^{\mathrm{bulk}} [L_0 + L_1 (x_A^{\mathrm{bulk}} - x_B^{\mathrm{bulk}})] \tag{38}$$

where $L_0 = (A + B)/2$ and $L_1 = (A - B)/2$.

The temperature-dependent parameters A and B for each binary pair were obtained from CALPHAD-based assessments (see Table 4):

Table 4: Temperature-dependent Redlich–Kister parameters for binary subsystems.

Composition	A ($\mathrm{J \cdot mol^{-1}}$)	B ($\mathrm{J \cdot mol^{-1}}$)	Ref.
Fe-Ni	$-8368 + 2.72T$	$-32217 + 9.205T$	[23]
Fe-Cr	$20794 - 10.46T$	20794−10.46T	[23]

Ni-Cr	-8368	-8368	[23]
Cr-Mo	$25522 + 11.30T$	$12552 + 5.86T$	[27]
Ni-Mo	$-17573 - 13.807T$	$-17573 - 13.807T$	[28]

The Redlich–Kister coefficients A and B define the temperature-dependent binary excess Gibbs-energy terms used in the Butler surface-tension calculations. For symmetric systems (Fe–Cr, Ni–Cr, Ni–Mo), $A = B$, yielding $L_1 = 0$. For asymmetric systems (Fe–Ni, Cr–Mo), both $L_0 = (A + B)/2$ and $L_1 = (A - B)/2$ were evaluated at each temperature to capture enthalpic asymmetry.

4. Bulk and Surface Gibbs Energy Relationships

For each component i, the partial Gibbs free energies for the bulk ($G_i^{E,B}$) and surface ($G_i^{E,S}$) phases were evaluated using Eqn. (31):

$$G_i^{E,S} \approx \beta G_i^{E,B}, G_i^{E,B} = \Delta G + \left(1 - x_i^{\text{bulk}}\right) \frac{\partial \Delta G}{\partial x_i^{\text{bulk}}} \tag{39}$$

where:

- $\beta = 0.83$ represents the coordination factor between surface and bulk atoms,

These relationships ensure thermodynamic consistency between the interfacial and bulk environments. [25].

5. Butler Model Formulation and Numerical Solution

At thermodynamic equilibrium, the chemical potentials of each species in the bulk and surface phases are equal. The corresponding Butler relations for each component i are:

$$\gamma = \gamma_i(T) + \frac{RT}{S_i} \ln \left(\frac{x_i^S}{x_i^{\text{bulk}}}\right) + \frac{G_i^{E,S} - G_i^{E,B}}{S_i} \tag{40}$$

where R is the universal gas constant and S_i is the molar surface area. The system of equations was solved iteratively for x_i^S and γ using a nonlinear least-squares solver (lsqnonlin, MATLAB Optimization Toolbox) with convergence tolerances of 10^{-14}. The residual function minimized the difference between the three Butler equations for each alloy, subject to the normalization constraint $\sum x_i^S = 1$. Initial guesses for surface compositions were taken near the

bulk values, and physically valid bounds were imposed ($0 < x_i^S < 1$) to ensure numerical stability.

6. Computational Outputs and Data Visualization

The equilibrium surface mole fractions (x_i^S) and total surface tension (γ) were computed at each temperature increment for all alloy systems. The results were tabulated and exported to Excel workbooks:

- Ni–Cr–Fe alloys: FeCrNi_Butler_Tsweep.xlsx
- Ni–Cr–Mo alloys: NiCrMo_Butler_Tsweep.xlsx

Each workbook contains:

- Sheet 1: Surface tension values, $\gamma(T)$
- Sheets 2–4: Surface mole fractions, $x_i^S(T)$

Scatter plots of surface tension versus temperature were generated to illustrate the predicted temperature dependence for all alloys

3.4 Chapter Summary

In summary, this chapter developed the thermodynamic framework for modelling density and surface tension in multicomponent alloys. The formalism for excess volume provided a basis for understanding mixing effects in binary and ternary systems, while the Butler approach captured surface segregation and interfacial behavior. These models serve as essential tools for linking experimental measurements with predictive thermodynamic descriptions.

CHAPTER 4. Results

This chapter presents experimental results for the temperature-dependent density and surface tension of Inconel 625, Inconel 718, and their ternary analogues (TA 625-Mo, TA 625-Fe, TA 718-Ni, TA 718-Fe) measured using ESL and EML techniques. These properties are essential for modelling fluid flow, droplet oscillations, and solidification in containerless environments. The results highlight how Fe, Mo, and Ni substitutions influence thermophysical behaviour compared to the industrial alloys. The reporting of uncertainty for all results involves 1-σ deviation.

4.1 Density

The density of the investigated Inconel superalloys and their ternary analogues was measured over the liquid and undercooled temperature ranges. The results show a linear decrease in density with temperature for all compositions, consistent with metallic liquid behaviour. The fitted parameters were obtained from electrostatic levitation (ESL) experiments and are summarized below.

To accurately calibrate the temperature scale and validate the thermodynamic predictions, both the solidus (T_S) and liquidus (T_L) temperatures of the investigated alloys were determined using two independent approaches:

i. Thermo-Calc modeling, employing the TCNI12 database to predict equilibrium phase boundaries.
ii. Differential Scanning Calorimetry (DSC) experiments, performed for the ternary analog alloys at the University of Alberta under the supervision of Dr. Jonas Valloton, providing experimental solidus and liquidus onset temperatures.

The results are summarized in Table 5. The measured DSC values show strong agreement (within ±5 K) with the Thermo-Calc predictions. The consistency across both methods confirms that the selected calibration standards accurately represent the equilibrium liquidus points for each composition.

Table 5: Solidus and liquidus temperatures obtained from Thermo-Calc and DSC analysis.

Alloy	ThermoCalc model T_S [K]	ThermoCalc model T_L [K]	DSC experiment T_S [K]	DSC experiment T_L [K]
TA625-Fe	1679.5	1682.4	1679.5	1687.7
TA625-Mo	1660.2	1670.3	1664.9	1675.3
TA718-Fe	1688.2	1689.6	1684.2	1691.1
TA718-Ni	1680.0	1681.4	-	1686.7

The pyrometric readings were corrected to obtain true liquidus temperatures. Figure 13 and Figure 14 present the measured temperature-dependent density for the industrial superalloys Inconel 625 and Inconel 718, while Figure 15 through Figure 17 show corresponding results for their ternary analogues (TA 625-Mo, TA 625-Fe, TA 718-Ni, and TA 718-Fe) obtained using electrostatic levitation (ESL).

In all cases, the density decreases linearly with increasing temperature, consistent with the volumetric thermal expansion characteristic of metallic liquids.

The temperature dependence of density is expressed by the linear relation:

$$\rho = \rho_0 + \frac{d\rho}{dT}(T - T_L) \tag{41}$$

where ρ_o is the density at the liquidus temperature (T_L) and ($d\rho/dT$) represents the temperature coefficient of density. The fitted parameters are summarized in

Table 6.

Table 6:Regression fit parameters for Density of Superalloys and ternary alloys

Material	ρ_0 [kg m^{-3}]	dρ/dT [kg m^{-3} K^{-1}]
Inconel 625	7819.43 ± 1.15	−1.07 ± 0.002
Inconel 718	7496.26 ± 0.53	−1.03 ± 0.006
TA625-Mo	7769.96 ± 1.27	−1.96 ± 0.017
TA625-Fe	7536.92 ± 1.12	−1.00 ± 0.010
TA718-Ni	7374.10 ± 0.51	−0.59 ± 0.011
TA718-Fe	7312.80 ± 1.13	−0.87 ± 0.019

Table 6 gives the regression fit for each alloy and shows how well a straight line can represent the overall trend of density with temperature. The fit uncertainty tells us only how confident we are in the slope and intercept of that line. It does not tell us how accurate each individual measurement is. In Figure 13 we see that the data have visible scatter around the fit line. The GUM uncertainty method addresses this by tracing uncertainty back to the actual measured inputs such as mass volume and temperature. It then propagates those errors to each calculated density value so that every point has its own uncertainty. In short, the regression fit describes how well one line represents the group of data while the GUM method shows how reliable each data point is. Both are needed to report uncertainty in a complete and transparent way.

In Figure 13, the references shown are the best available because very few high-temperature studies exist for Inconel alloys, and Phillips et al. [6] provide the most recent and reliable containerless ESL/EML density measurements. These data are trusted because they use calibrated levitation platforms, compare multiple vendor alloys, and avoid container-related errors. We assume the measurements are accurate, the alloy compositions represent typical Inconel 718, and that oxidation and evaporation were negligible during processing. Overall, this study offers the most dependable dataset currently available.

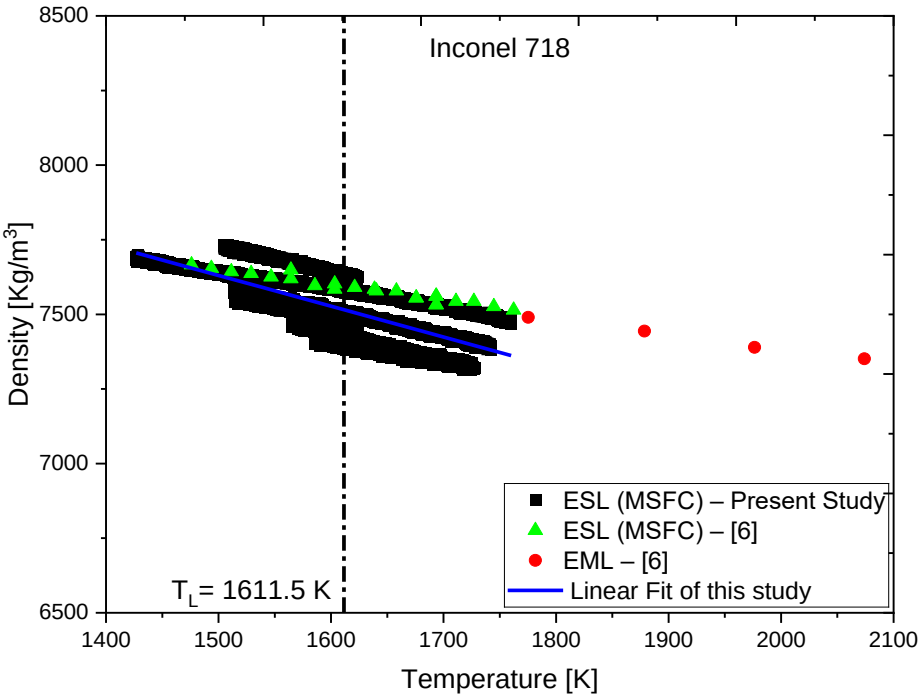

Figure 13: Density for Inconel 718 (ESL Data)

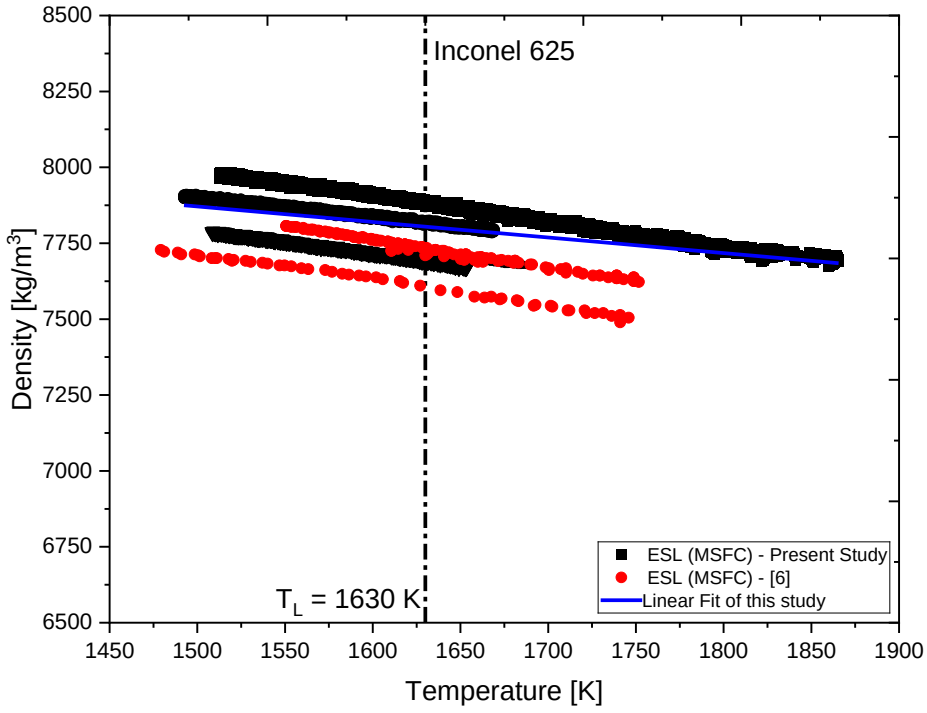

Figure 14: Density for Inconel 625 (ESL Data)

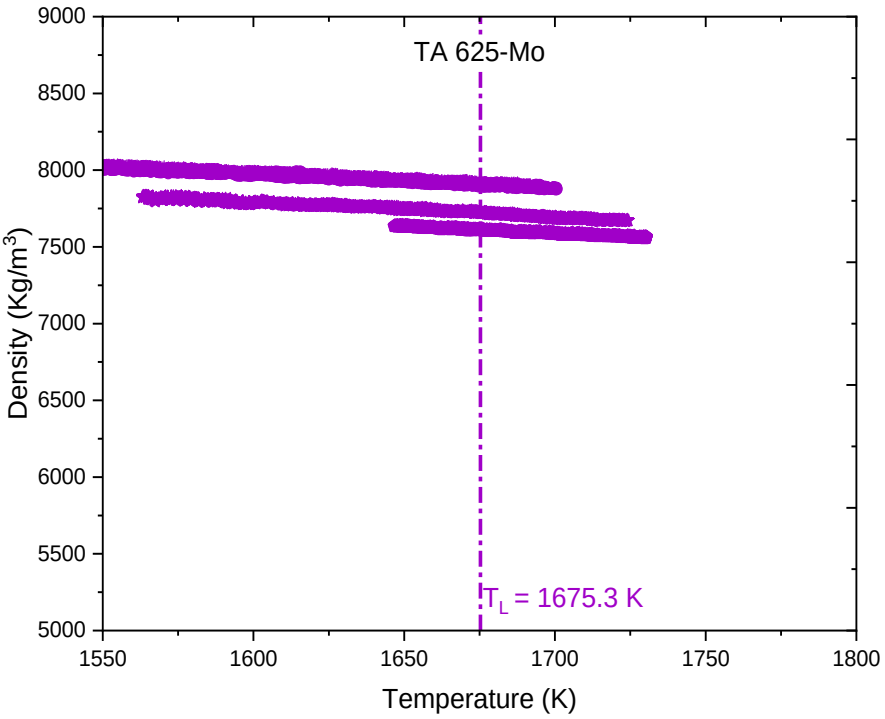

Figure 15: Density for TA625-Mo (ESL Data)

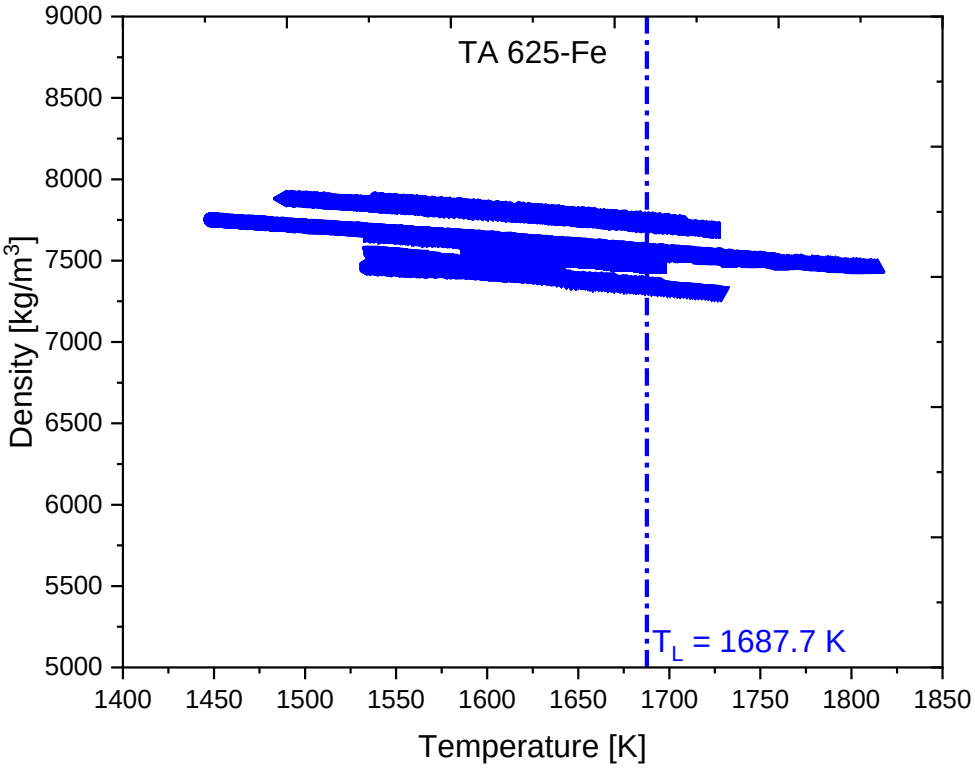

Figure 16: Density for TA625-Fe (ESL Data)

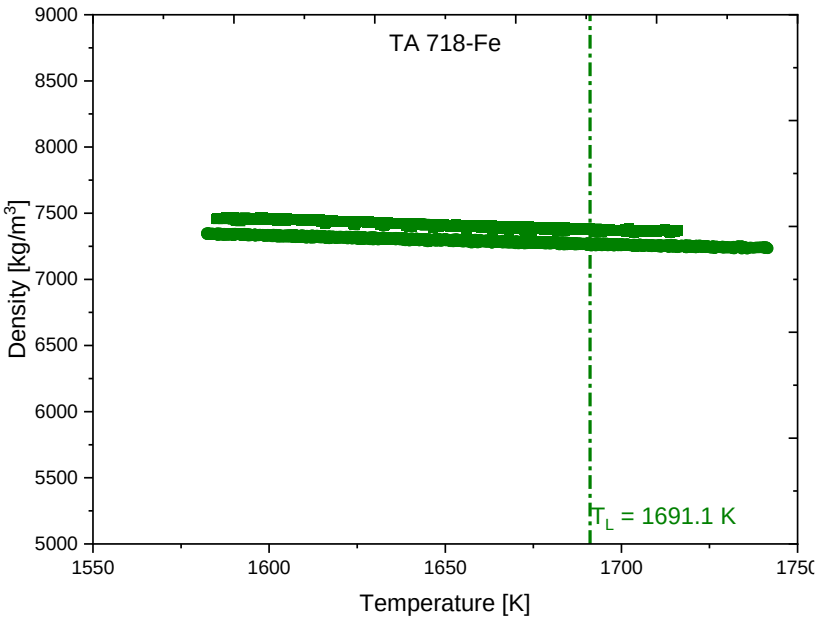

Figure 17: Density for TA718-Fe (ESL Data)

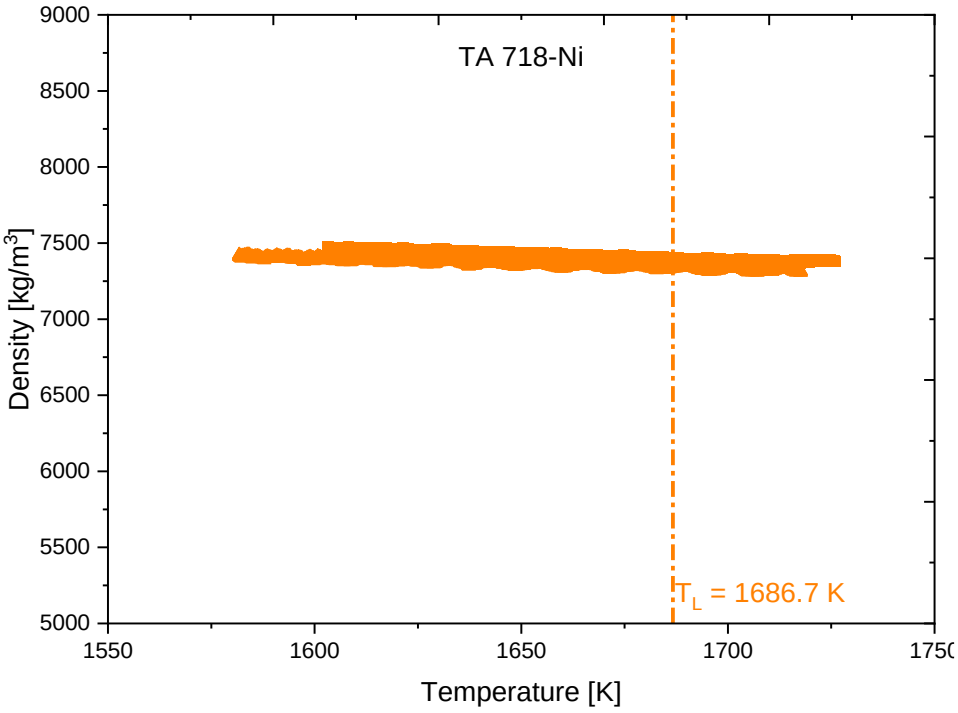

Figure 18: Density for TA718-Ni (ESL Data)

4.2 Surface Tension

In this study, surface tension was measured for the industrial superalloys Inconel 625 (Appendix D) and Inconel 718 (Appendix E), together with their ternary analogues. The measurements were performed using the oscillating drop method, which determines surface tension from the natural oscillation frequency of a levitated droplet.

To illustrate the methodology, frequency identification techniques were applied to several oscillation cycles of MAT-2062 (Inconel 625) at 1696 K. Independent methods including inverted period measurement, cycle counting, and Fast Fourier Transform (FFT) analysis were used to extract the dominant oscillation frequency.

Table 7 provides an example comparison, where inverted period measurement, cycle counting, and FFT yield frequencies in close agreement with the expected natural frequency of 208.59 Hz.

Table 7: Frequency identification methods compared for MAT-2062 Inconel 625.

MAT-2062 Inconel 625 Hold_1696K 201, 202, 203, 204, 205, 206, 207, 208, 209, 2011							
Pulse 1 (201 Hz)							
Bandpass filter range (Hz)	Method 1: Inverted period measurement (Hz)		Method 2: Count number of cycles in known time (Hz)		FFT (Hz)		Delta (%)
	Forced	Damped	Forced	Damped	Forced	Damped	
150-300	208.589	209.302	210.366	210.425	201.172	201.172	0.998
160-280	205.521	209.302	207.317	210.425	201.172	201.172	1.006
170-250	205.521	205.426	207.317	206.564	201.172	201.172	0.983
170-230	202.454	203.488	204.268	204.633	201.172	201.172	1.005
180-230	202.454	201.55	204.268	202.703	201.172	201.172	0.984
180-210	202.454	201.55	204.268	202.703	201.172	201.172	0.981
190-205	202.454	201.55	204.268	202.703	201.172	201.172	0.967

A bandpass filter is applied to isolate the dominant second mode, but the selected filter range introduces measurable shifts in the extracted frequency.

As shown in Table 7, wider filter ranges such as 150–300 Hz retain more of the oscillation content but also allow unwanted components to remain in the signal. These include higher order oscillation modes (such as small contributions from the third and fourth modes), electronic noise from the camera, and low amplitude disturbances from residual jitter in the levitation field. Their presence slightly distorts the droplet oscillation and leads to higher extracted frequencies when using inverted period measurement and cycle counting.

Narrower ranges such as 190–205 Hz remove a larger fraction of these unwanted components, resulting in a cleaner second mode signal. Across all filter choices, the variation in the time domain-based methods is approximately 1%, confirming that filtering directly influences the determination of the oscillation period.

FFT based frequencies remain nearly constant because the dominant spectral peak of the droplet oscillation waveform is stable and less sensitive to small waveform modifications. However, the FFT still operates within the defined passband, so the filter determines which spectral components are available for peak detection. Therefore, the variability seen in the other methods represents a real and quantifiable contribution to the total frequency uncertainty.

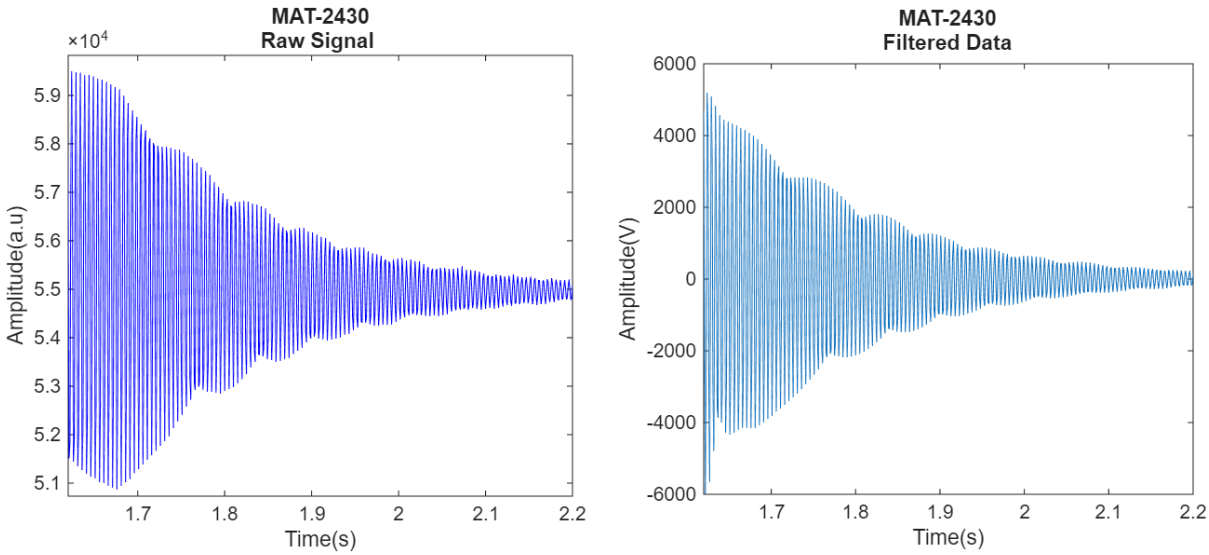

Figure 19: Raw Signal and Filtered droplet oscillation.

Figure 19 compares the raw droplet oscillation waveform with the band-pass-filtered signal centered on the dominant oscillation mode. Although the two traces appear visually similar, this is expected because the raw data are already dominated by a strong ~200 Hz mode that lies entirely within the selected 190–205 Hz passband. The raw signal therefore contains the correct oscillatory shape but also includes a large background offset, slow baseline drift, and minor contributions from higher-order modes and electronic noise. The filtering step suppresses these secondary components while preserving the fundamental oscillation, yielding a waveform that is cleaner, centered around zero, and more sinusoidal. This improved clarity enhances the reliability of peak detection and enables more accurate extraction of the natural frequency and damping behavior from the decaying oscillation envelope.

Two complementary approaches were applied to select the natural frequency. The Maximum Amplitude (MA) Method identifies the frequency at the peak of the fitted deformation curve, corresponding to the maximum oscillation response with varying excitation frequency. In contrast, the Frequency Crossover (CO) Method determines the natural frequency at the intersection of forced and damped response frequencies, where the oscillation stabilizes [19]. As shown in Figure 20, the two methods give closely matching results, with only a 0.25% difference, thereby providing independent confirmation of the natural frequency.

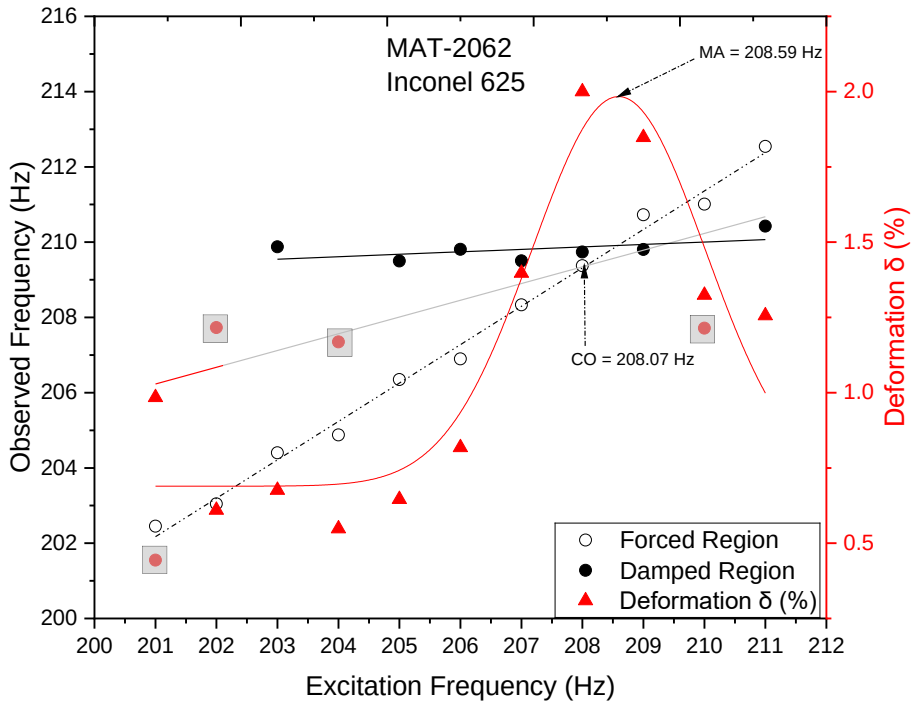

Figure 20: Peak of fitted deformation curve (MA) and crossover of forced/damped frequencies (CO).

In Figure 20, several damped frequency points at 201 Hz, 202 Hz, 204 Hz, and 210 Hz fall noticeably below the expected damped response curve. These points are boxed on the figure and represent cycles where the droplet oscillation signal was affected by issues such as mode mixture, or transient noise. Because these low outliers steepen the (Grey) trend, the resulting curve underestimates the true value of the decaying response and shifts the crossover point lower than expected.

To improve the curve fit, these points should be removed during curve fitting. Excluding these outliers restores the correct upward (Black) trend of the damped curve toward the deformation maximum and produces a flat, more realistic curve shape. This adjustment yields a more pronounced intersection between the forced and damped curves and results in a crossover

frequency that aligns closely with the maximum amplitude value. In this dataset, removing the 201 Hz, 202 Hz, 204, and 210 Hz damped points shifts the crossover from approximately 208.07 Hz to a 208.56 Hz which is consistent with the MA value of 208.59 Hz, improving consistency between the 2 independent frequency selection methods.

After determining the natural frequency (f_n), the surface tension (γ) of each composition was calculated using Equation (8). The measured temperature-dependent surface-tension data are presented in Figure 21 through Figure 26. Figure 21 and Figure 22 show the surface-tension variation for the industrial superalloys Inconel 718 and Inconel 625, respectively. Figure 23 and Figure 24 illustrate the corresponding results for the TA 625-Mo and TA 625-Fe analogues, while Figure 25 and Figure 26 display the surface-tension trends for TA 718-Fe and TA 718-Ni.

Across all systems, the surface tension decreases linearly with increasing temperature, consistent with the thermodynamic weakening of metallic bonds at elevated temperatures. The ternary analogues generally exhibit slightly lower surface-tension magnitudes than their industrial counterparts, indicating the influence of substitutional alloying elements on surface energetics and atomic cohesion at the liquid interface.

The temperature dependence of surface tension follows the linear relation:

$$\gamma(T) = \gamma_o + \frac{d\gamma}{dT}(T - T_L) \tag{42}$$

where γ_o is the surface tension at the liquidus temperature (T_l) and ($d\gamma/dT$) represents the temperature coefficient of surface tension. The fitted parameters obtained from ESL and EML measurements are summarized in Table 8.

Table 8: Regression Fit Parameters for Surface-Tension of Superalloys and Ternary Analogues

Material	γ_o	$\frac{d\gamma}{dT}$
Inconel 625	1.83±0.03	-3.42E-04±1.96E-04
Inconel 718	1.72±0.07	-2.38E-05±6.14E-05
TA 625-Mo	1.71±0.17	-3.19E-03±5.47E-03
TA 625-Fe	1.76±0.02	-3.29E-04±4.47E-04
TA 718-Ni	1.65±0.05	-5.58E-04±5.45E-04
TA 718-Fe	1.65±0.06	-8.68E-04±1.35E-04

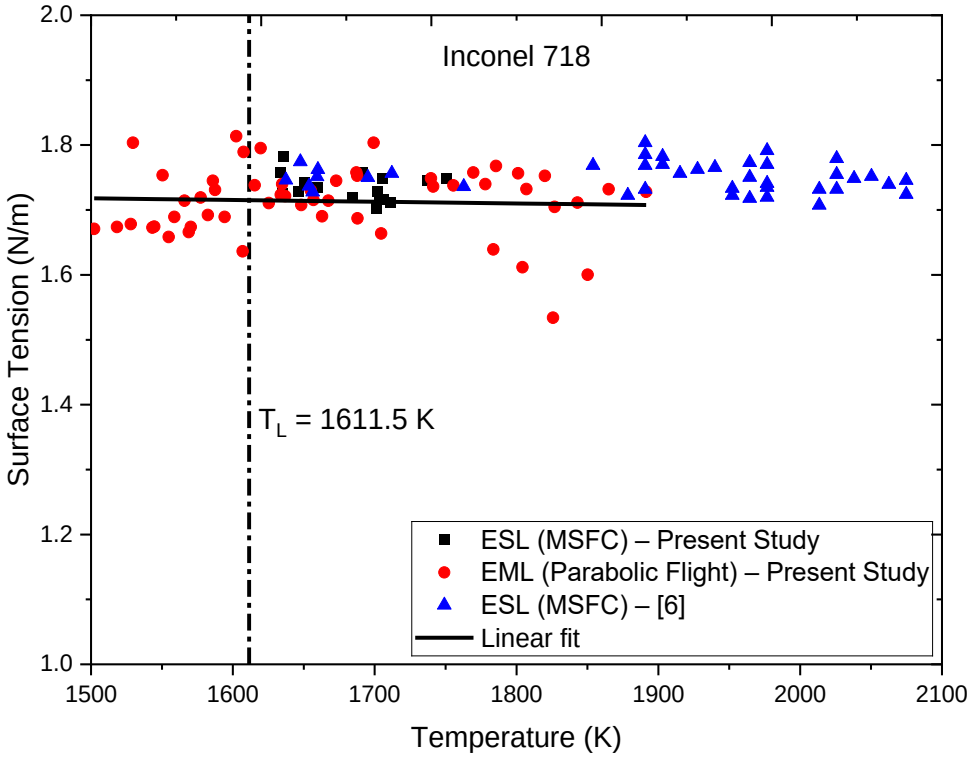

Figure 21: Surface Tension for Inconel 718

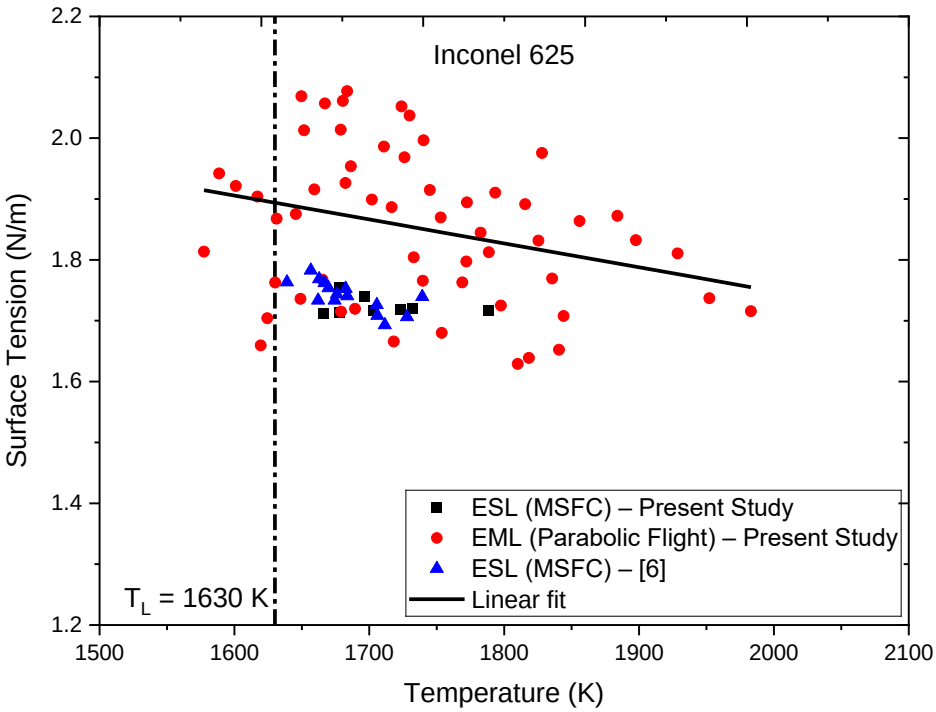

Figure 22: Surface Tension for Inconel 625

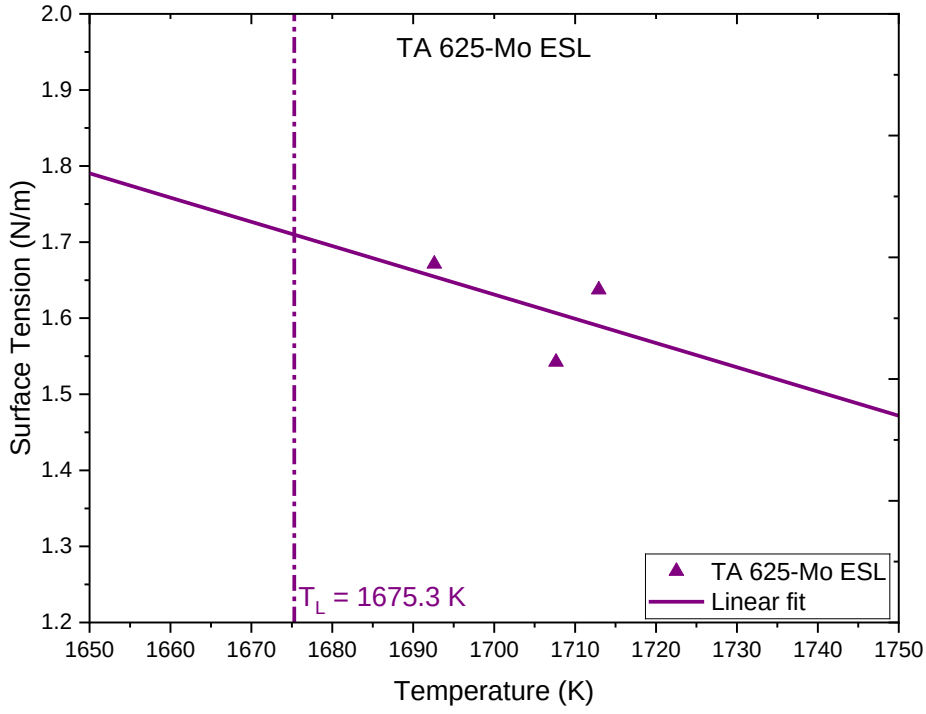

Figure 23: Surface Tension for TA625-Mo

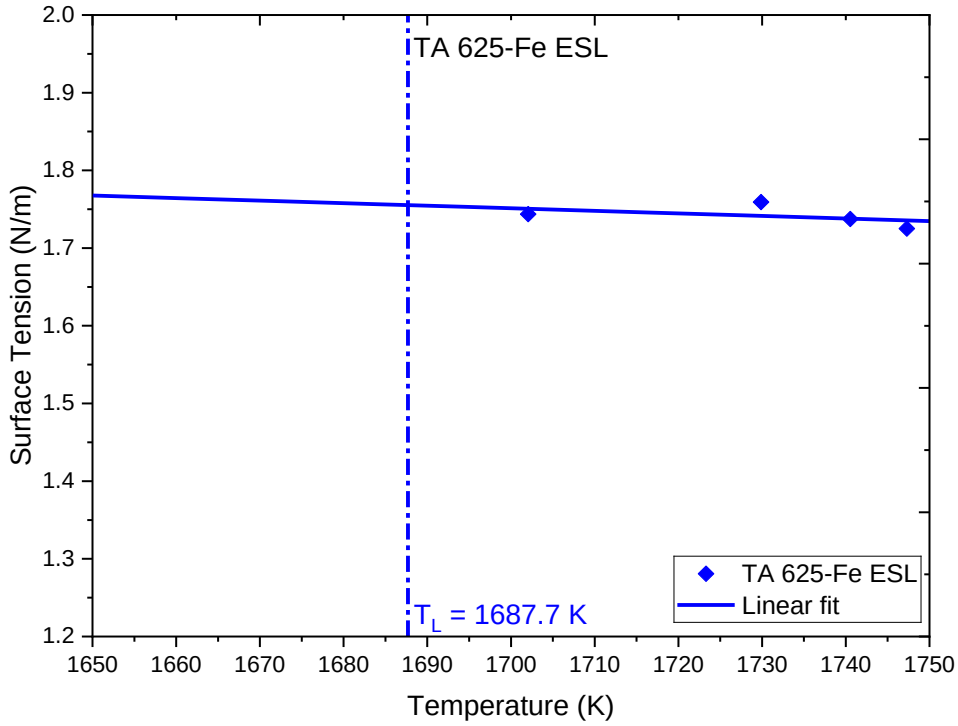

Figure 24: Surface Tension for TA625-Fe

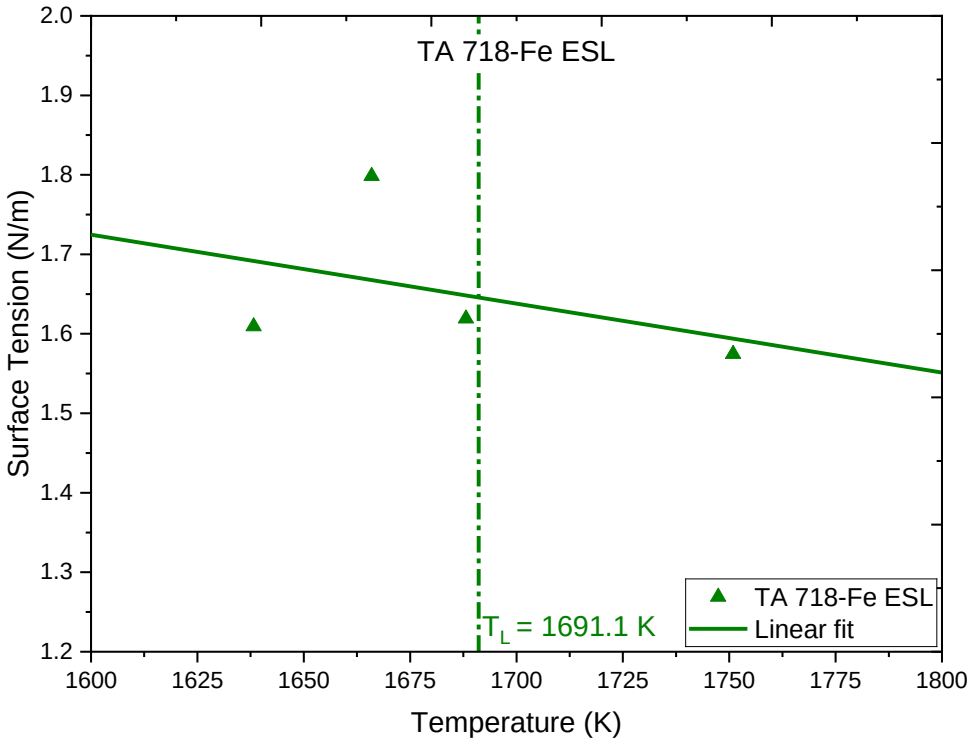

Figure 25: Surface Tension for TA718-Fe

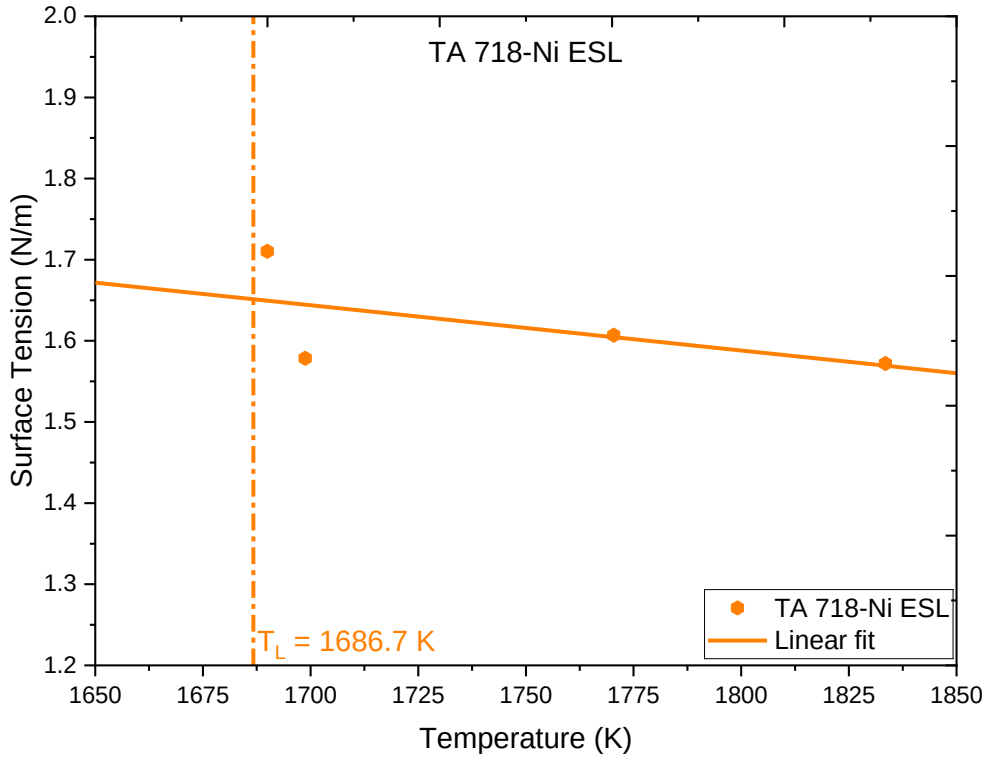

Figure 26: Surface Tension for TA718-Ni

4.3 Chapter Summary

This chapter presented experimental results for the density and surface tension of Inconel 625, Inconel 718, and their ternary analogues measured using ESL and EML techniques. Both properties showed a linear decrease with temperature, typical of metallic liquids. The ternary analogues exhibited slightly lower density and surface tension values than the industrial alloys, reflecting the influence of Fe, Mo, and Ni substitutions. These results provide essential data for validating thermodynamic models and understanding melt behaviour in containerless environments.

CHAPTER 5. Discussion

5.1 Modelled Results

This section presents the thermophysical behaviour of the ternary analog alloys as predicted from computational modelling. Two properties are examined: density, evaluated using the partial-molar-volume (PMV) model under both ideal and non-ideal mixing conditions, and surface tension, evaluated using the Butler thermodynamic framework. With the modelling approach established, the discussion proceeds first with the prediction of liquid density for the ternary analog systems.

5.1.1 Density

The liquid densities of the four ternary analog alloys were predicted using the Partial-Molar-Volume (PMV) model under both ideal and non-ideal mixing conditions. In the ideal formulation ($V^E = 0$), the alloy volume was calculated as the composition-weighted sum of the temperature-dependent partial molar volumes of the constituent elements. The predicted density–temperature relationships (Figure 27) show a linear decrease with increasing temperature for all compositions, consistent with the thermal expansion behaviour typical of metallic liquids.

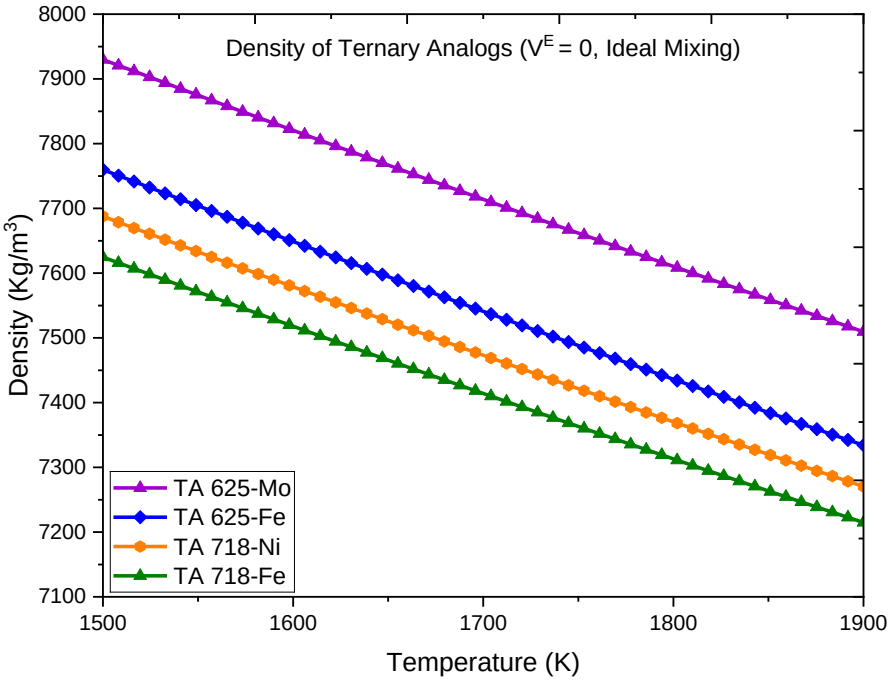

Figure 27: Modelled density ($V^E = 0$) computed using the ideal PMV model

Among the four systems, TA 625-Mo exhibits the highest density due to the combined effect of molybdenum's high atomic weight and low liquid molar volume. Within the Ni-Cr-Fe systems, density decreases systematically with increasing Fe content, reflecting Fe's lower molar mass and larger atomic volume compared with Ni. These results confirm that, even under ideal conditions, the PMV model captures physically consistent, composition-dependent density trends across the ternary analogs.

The non-ideal PMV formulation (Figure 28) extends this model by incorporating a positive excess molar volume term derived from Redlich–Kister binary interaction parameters for Fe–Ni, Fe–Cr, and Cr–Ni. This term accounts for atomic size mismatch and local structural disorder within the melt, slightly reducing the predicted densities (~2%) without altering the overall temperature or compositional trends. Including this correction improves agreement with experimental results and provides a more realistic thermodynamic description of the liquid phase.

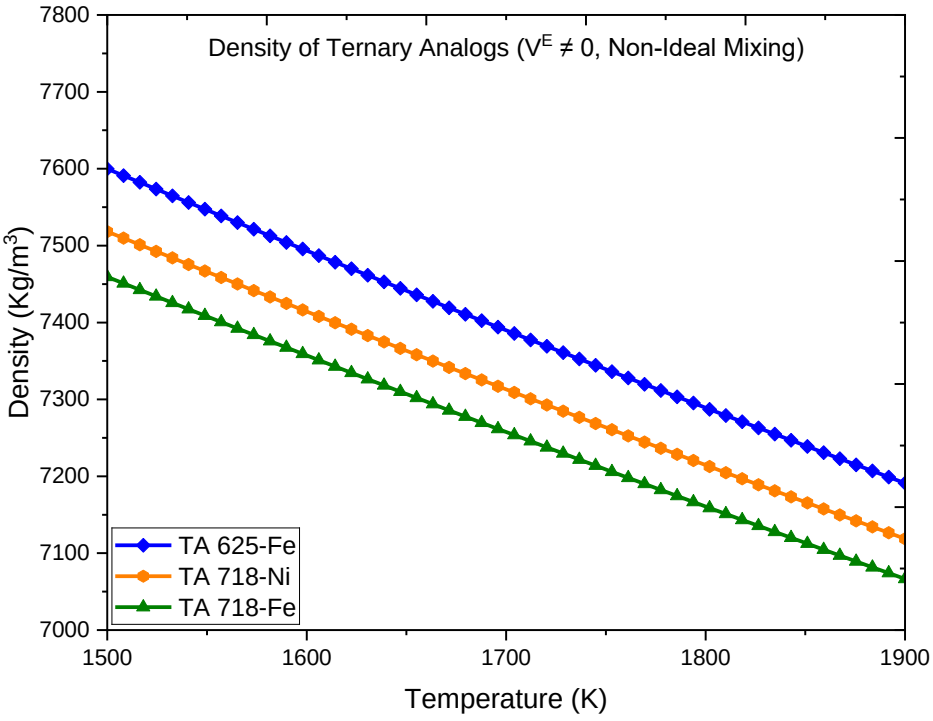

Figure 28: Modelled density ($V^E \neq 0$) computed using the non-ideal PMV model

The TA 625-Mo alloy shows a clear linear decrease in density with temperature (Figure 29). The ESL measurements yield a slope of -1.964×10^3 kg·m^{-3}·K^{-1} and a liquidus density of 7769.97 kg·m^{-3} at 1675.3 K. The ideal PMV prediction (7741.92 kg·m^{-3}) differs by only 0.36%, confirming excellent agreement at the liquidus. This small deviation indicates minimal

non-ideal mixing effects, consistent with the weak atomic size mismatch and strong solubility among Ni, Cr, and Mo atoms. Although the experimental slope is approximately 46% steeper than the model prediction, the PMV framework successfully reproduces the equilibrium liquid density.

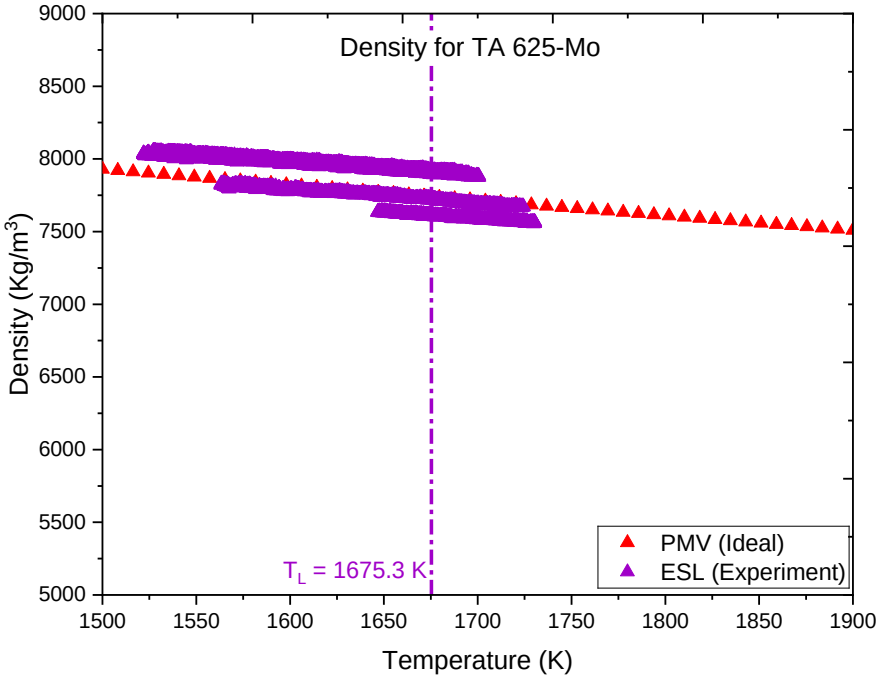

Figure 29: Experimental and modelled liquid density of TA 625-Mo

For TA 625-Fe, the measured density decreases nearly linearly with increasing temperature (Figure 30). The ESL-derived slope is -1.009×10^3 kg·m^{-3}·K^{-1}, and the liquidus density is 7536.92 kg·m^{-3} at 1687.7 K. The ideal PMV model predicts 7556.11 kg·m^{-3} (0.26% higher), while the non-ideal form gives 7404.42 kg·m^{-3} (1.76% lower). Both values lie within 2% of experiment, validating the PMV model for Fe-containing Ni–Cr systems. The small difference between ideal and non-ideal predictions reflects limited excess volume effects from Fe–Ni and Fe–Cr interactions. Compared with TA 625-Mo, this Fe-rich alloy exhibits a lower overall density, as expected from the substitution of lighter Fe atoms with larger atomic volumes.

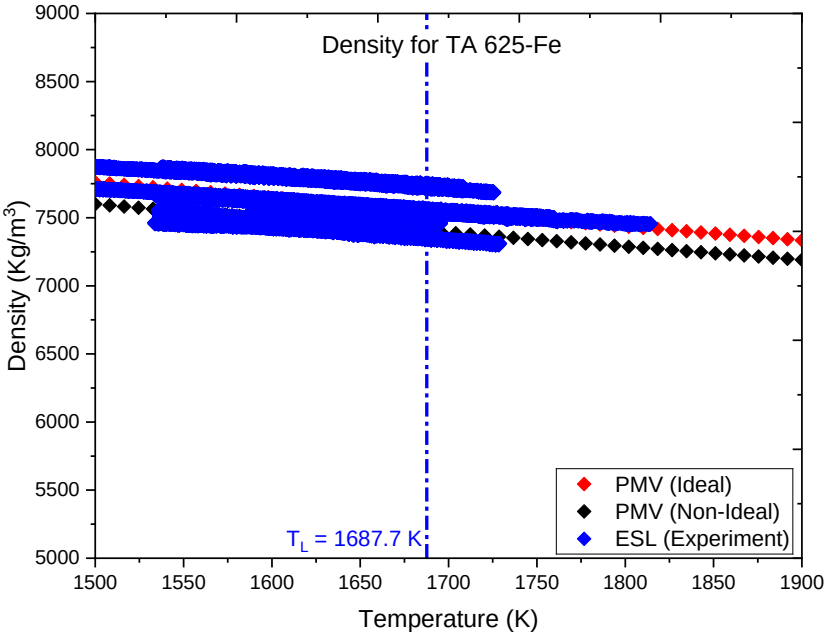

Figure 30: Experimental and modelled liquid density of TA 625-Fe

The TA 718-Fe alloy also exhibits a linear density–temperature relationship (Figure 31), with an experimental slope of -0.867×10^3 kg·m^{-3}·K^{-1} and a liquidus density of 7312.81 kg·m^{-3} at 1891.1 K. The ideal PMV model predicts 7425.14 kg·m^{-3} (1.54% higher), while the non-ideal version gives 7268.22 kg·m^{-3} (0.61% lower). Agreement within 2% demonstrates the PMV model's robustness for Fe-rich Ni–Cr systems.

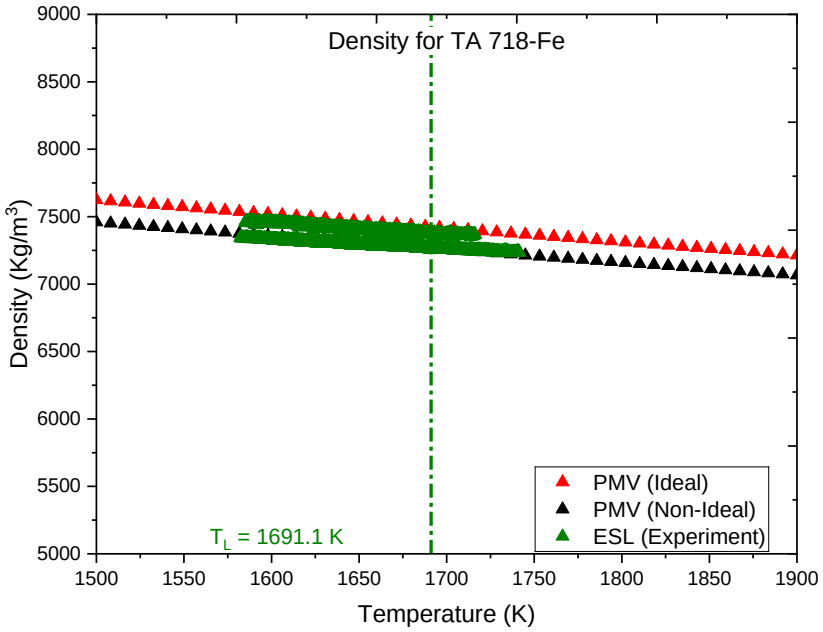

Figure 31: Experimental and modelled liquid density of TA 718-Fe

The TA 718-Ni alloy shows a clear linear decline in density with temperature (Figure 32). The ESL results give a slope of -0.589×10^3 kg·m^{-3}·K^{-1} and a liquidus density of 7374.11 kg·m^{-3} at 1696.7 K. The ideal PMV model predicts 7489.01 kg·m^{-3} (1.56% higher), and the non-ideal form yields 7328.25 kg·m^{-3} (0.62% lower). Both predictions reproduce the experimental density within ±2 %, confirming the reliability of the PMV framework for Ni-rich Ni–Cr–Fe systems. The slightly closer match from the non-ideal model implies minor but non-negligible excess volume effects, even in Ni-dominant compositions. Compared with TA 718-Fe, this Ni-rich alloy shows higher density and a smaller thermal expansion slope, consistent with Ni's higher atomic mass and smaller molar volume.

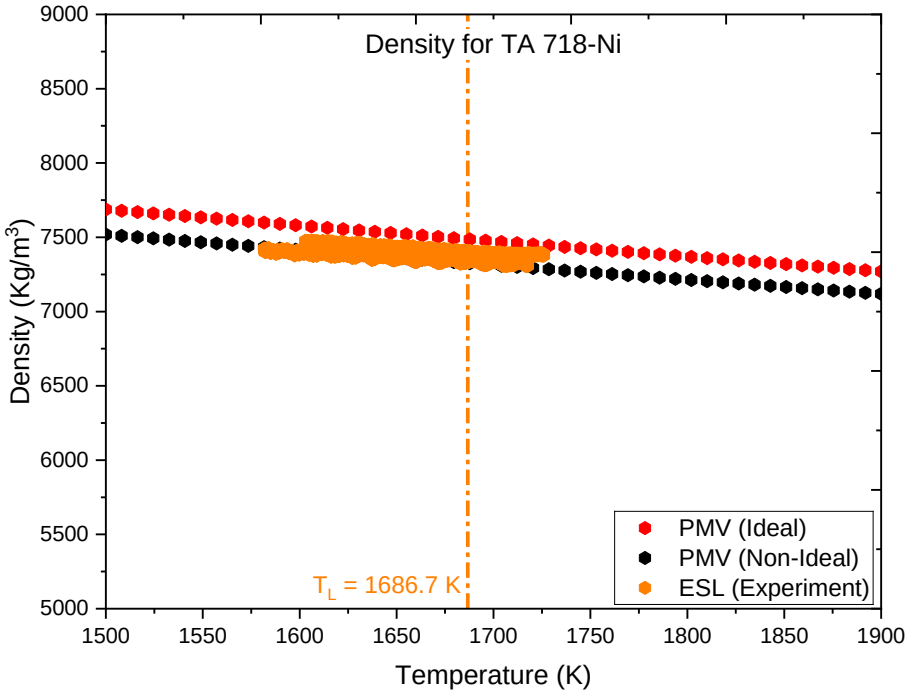

Figure 32: Experimental and modelled liquid density of TA 718-Ni

Across all four ternary systems, the PMV model (both ideal and non-ideal) accurately captures the magnitude and temperature dependence of liquid density, with deviations from experiment remaining within approximately 2%. The inclusion of the non-ideal term marginally improves accuracy, particularly for Fe-rich alloys, confirming its physical relevance. These findings demonstrate that the PMV framework provides a reliable and thermodynamically consistent foundation for modelling the temperature-dependent thermophysical behaviour of Ni–Cr–(Fe, Mo) alloy systems.

5.1.2 Surface Tension

The Butler-model predictions shown in Figure 33 exhibit a linear decrease in surface tension with temperature for all four ternary analogs across the 1500 – 1900 K range, consistent with the characteristic behaviour of metallic liquids. Among the alloys, TA 718-Fe displays the highest surface tension, followed by TA 718-Ni, TA 625-Mo, and TA 625-Fe. Across all alloys, surface tension decreases linearly with increasing temperature, consistent with the weakening of metallic bonds at elevated temperatures. The Butler model successfully reproduces this temperature dependence, though its absolute predictions are systematically higher (by 5–15%) than the experimental ESL data. The full implementation code of the Butler framework, including all computational formulations, is provided in Appendix H and Appendix I.

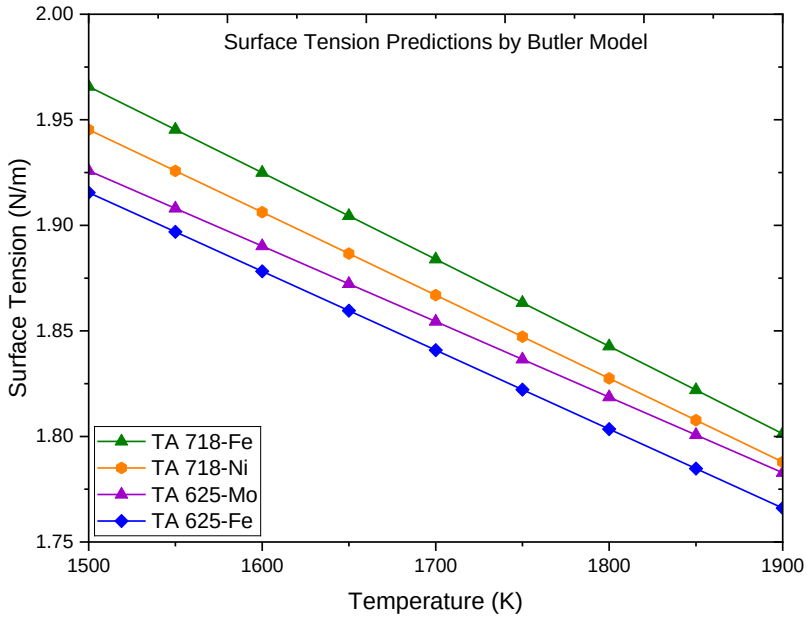

Figure 33: Surface tension for ternary analogs predicted by the Butler model

5.1.2.1 Comparison with Experimental ESL Results

Figure 34 shows that the Butler model predicts surface-tension values approximately 9% higher than those measured experimentally. This difference arises because the model assumes complete surface equilibrium, allowing atoms to fully rearrange and minimize surface energy. In contrast, during ESL experiments, the droplet remains molten for only a short time, preventing full equilibration. As a result, the experimentally measured surface tension is slightly lower. The Butler model thus captures the overall temperature trend but overestimates the absolute magnitude of γ due to transient, non-equilibrium conditions.

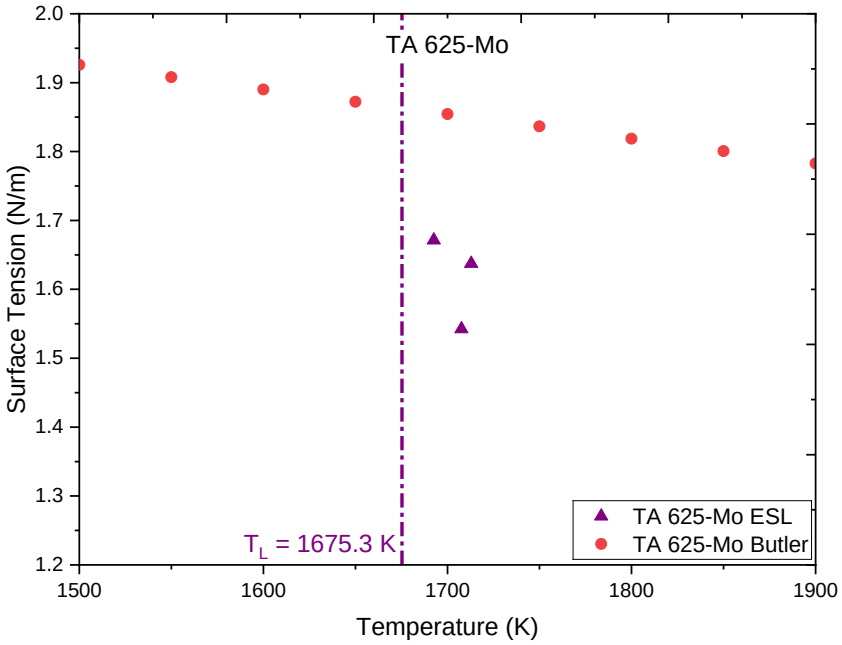

Figure 34: Experimental and modelled Surface tension of TA 625-Mo

In TA 625-Fe (Figure 35), the deviation between Butler predictions and ESL measurements is smaller, around 5%. This improved agreement reflects the lower surface activity of Fe compared to Mo. Iron atoms migrate more slowly toward the surface and possess a weaker segregation driving force, resulting in a near-equilibrium surface during ESL measurement. Consequently, Fe-containing alloys exhibit better correspondence between modelled and experimental γ values.

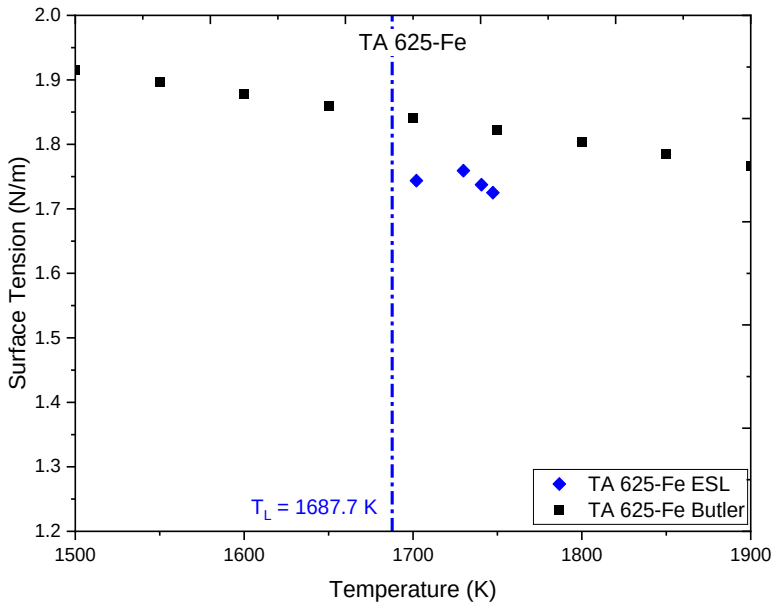

Figure 35: Experimental and modelled Surface tension of TA 625-Fe

For TA 718-Fe (Figure 36), he Butler-predicted values remain about 15% higher than the ESL data. However, both datasets exhibit nearly identical temperature slopes ($\partial\gamma/\partial T$), confirming that the Butler model accurately represents the temperature dependence of surface tension. The main difference lies in the absolute magnitude of γ, not its slope. The upward offset of the Butler curve arises from its equilibrium assumption, while the ESL data reflect non-equilibrium surfaces limited by the short experimental timescale for segregation.

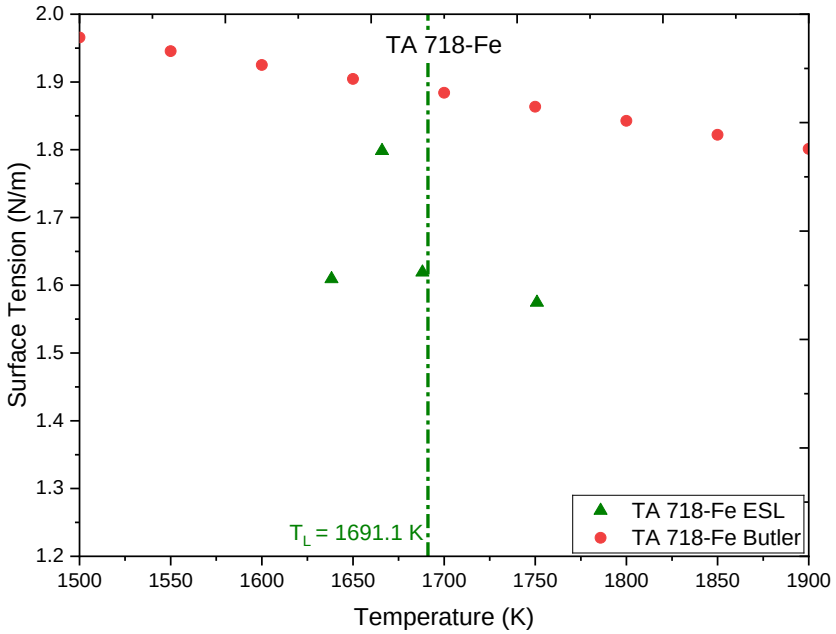

Figure 36: Experimental and modelled Surface tension of TA 718-Fe

Similarly, for TA 718-Ni (Figure 37), the offset between model and experiment is about 13%, slightly smaller than that of TA 718-Fe. Both datasets display the expected negative temperature coefficient, demonstrating that the Butler model captures the correct thermodynamic trend. The smaller offset is attributed to Ni's stronger surface affinity and faster diffusion, which enable partial equilibration even during the short duration of the ESL experiment.

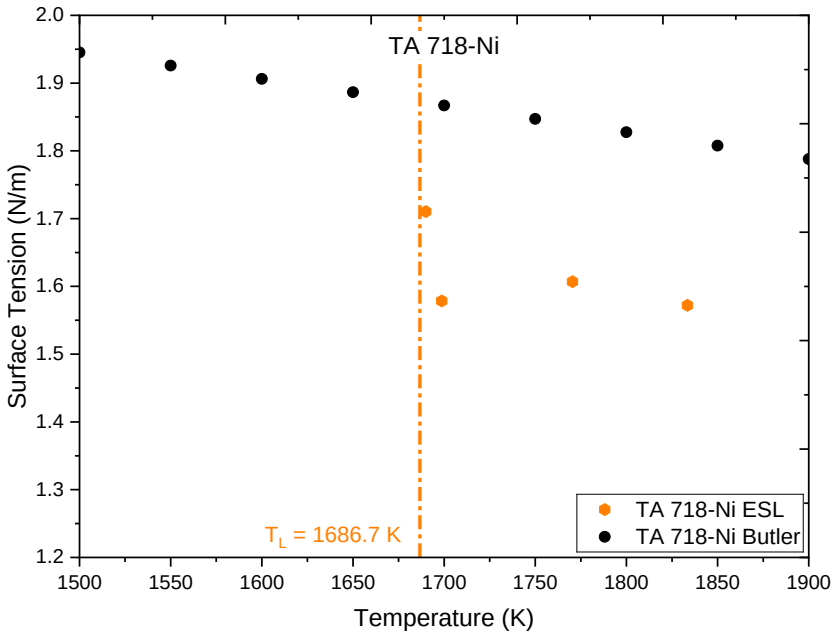

Figure 37: Experimental and modelled Surface Surface tension of TA 718-Ni

5.1.2.2 Interpretation of Butler–Experiment Deviation

Across all four ternary analog systems, Butler model predictions overestimate the experimental surface tension by about 5–15%. This systematic overprediction is consistent with behaviour reported previously for levitated metallic systems. Xiao and Brillo [25] showed that even under highly purified conditions (oxygen content below 0.003 at. % O), measured surface tensions of Fe–Ni, Fe–Cr, and Ni–Cr binary alloys remained 10–20% below equilibrium Butler predictions. They attributed this difference to minor oxygen adsorption and incomplete surface equilibration, which drive preferential enrichment of surface-active elements such as Ni and Cr at the liquid–vapour interface. This enrichment lowers the effective interfacial free energy and therefore reduces the measured surface tension. Their physics-informed statistical modelling further demonstrated that trace oxygen contents in the range 0.03–0.10 at.% can reduce γ by as much as 40% and, in extreme cases, can even reverse the sign of $\partial\gamma/\partial T$ from negative to positive [25].

The present ternary analogs follow a similar hierarchy of deviations. Fe-rich systems (TA 718-Fe and TA 625-Fe) display the largest offsets between Butler predictions and ESL data, which is consistent with the strong oxygen affinity of Fe and its slower diffusion, both of which hinder complete surface equilibration during the short levitation experiments. In contrast, the Mo-containing alloy TA 625-Mo shows a smaller discrepancy, reflecting Mo's weak surface activity and limited interaction with adsorbed oxygen. These trends support the interpretation

that the magnitude of the Butler–experiment deviation is controlled mainly by kinetic limitations and impurity adsorption rather than by deficiencies in the underlying thermodynamic formalism.

5.1.2.3 Surface Segregation Behaviour at 1890 K

To better understand the relationship between composition and surface energy, the Butler model was used to calculate surface and bulk atomic fractions at 1890 K. The results (Figures 38–41) compare the surface atomic fraction (x_s) with the corresponding bulk fraction (x_{bulk}). The dashed 45° line represents the condition of no segregation ($x_s = x_{\text{bulk}}$); points above this line indicate surface enrichment, while those below indicates surface depletion.

The measured XPS compositions in Appendix L show very good agreement with the trends predicted by these figures. The XPS data confirm strong nickel enrichment at the surface of all alloys in agreement with Figure 38 which predicts nickel as the most surface-active element. The measured chromium depletion corresponds to the mild negative segregation trend predicted in Figure 39. For alloys that contain iron, the XPS results show clear surface depletion of iron which matches the predicted behavior illustrated in Figure 40. Although molybdenum was not directly quantified by XPS, the chromium enrichment observed in the TA 625-Mo analogs is consistent with the extreme molybdenum depletion predicted in Figure 41 which reduces the ability of molybdenum to occupy surface sites.

This agreement between model and experiment demonstrates that the thermodynamic driving forces included in the Butler formulation accurately describe the segregation behavior of these ternary analog alloys. The alignment between predicted and measured trends also strengthens the use of Butler model calculations as a reliable tool for interpreting high temperature surface tension measurements in nickel-based systems.

A. Nickel (Ni)

Nickel is the most surface-active element in all alloys (Figure 38). All data points lie above the no-segregation line, with a linear fit slope of 1.072 ± 0.088, indicating an average 7 % enrichment relative to the bulk. The highest enrichment occurs in TA 625-Mo and TA 625-Fe, which contain higher bulk Ni content. This Ni accumulation at the interface lowers the overall surface energy, explaining the smaller surface-tension (γ) values observed experimentally and predicted by the Butler model.

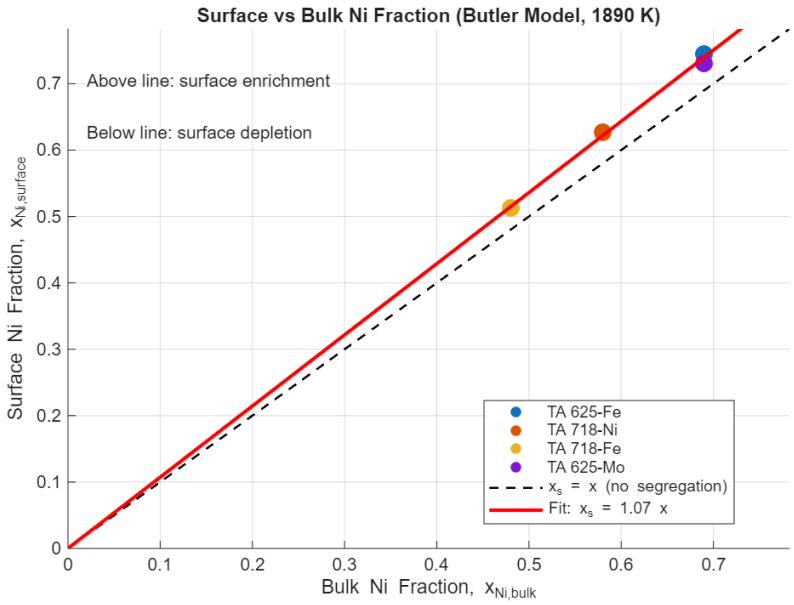

Figure 38: Surface versus bulk Ni fraction

B. Chromium (Cr)

Chromium exhibits mild depletion (Figure 39). The slope of 0.941 ± 0.078 suggests a 6 % average surface depletion. Most alloys plot close to the $x_s = x_{bulk}$ line, showing only minor deviations. A slight enrichment in TA 625-Mo is attributed to Cr–Mo interactions, which suppress Mo at the interface. Overall, Cr maintains a balanced surface presence, exerting minimal influence on total surface tension among the alloys.

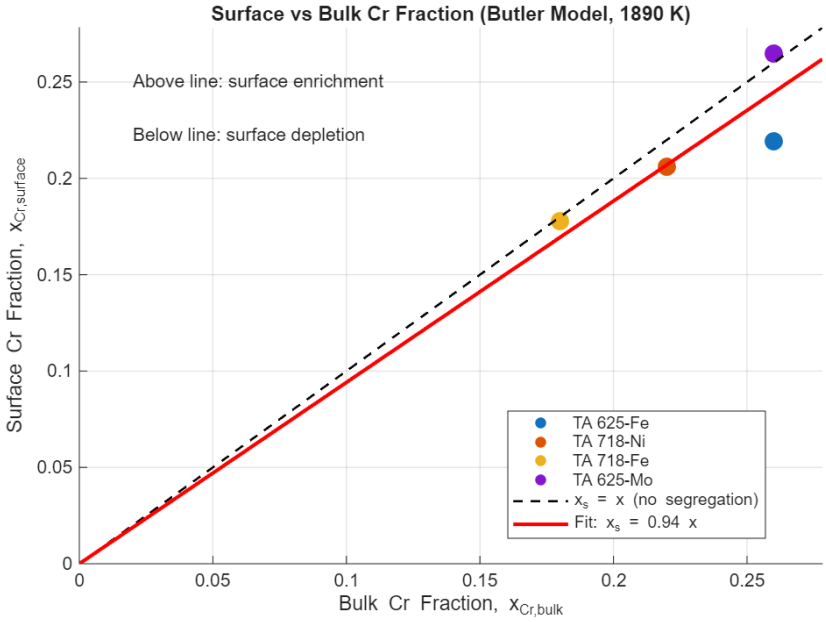

Figure 39: Surface versus bulk Cr fraction.

C. Iron (Fe)

Iron is consistently depleted from the surface in Fe-containing alloys (Figure 40), with a fit slope of 0.887 ± 0.334, corresponding to about 11 % depletion relative to bulk composition. The strongest depletion occurs in TA 625-Fe, where Ni dominates surface sites due to its higher surface activity. This Fe depletion correlates with higher surface-tension values and larger model-experiment deviations observed for Fe-rich alloys.

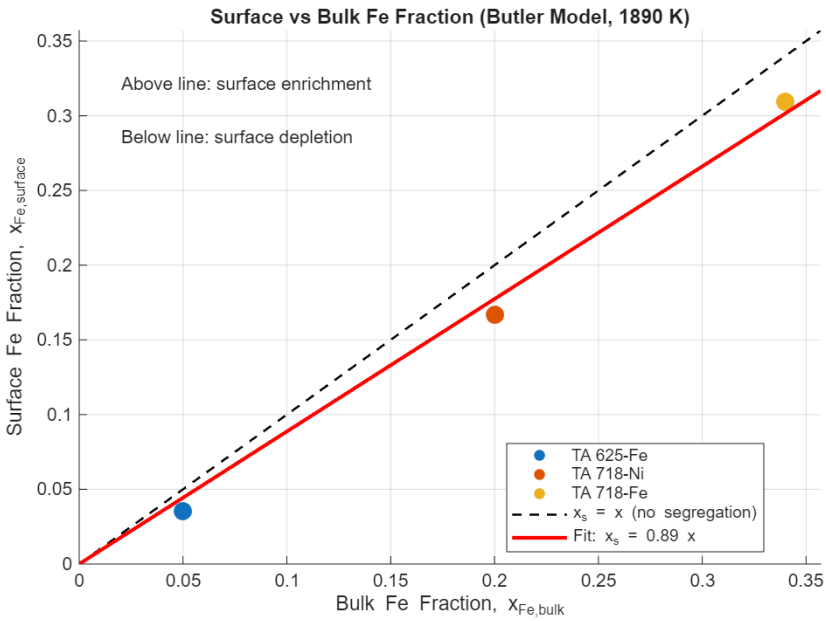

Figure 40: Surface versus bulk Fe fraction.

D. Molybdenum (Mo)

Molybdenum shows the strongest surface depletion (Figure 41). The slope of 0.08 indicates that only 8 % of the bulk Mo concentration appears at the surface, confirming Mo's very low surface activity. Because of its high surface tension, Mo remains largely in the bulk phase. However, its presence enhances Ni enrichment through Ni–Mo interactions, indirectly contributing to the reduction of surface tension in Ni–Mo alloys.

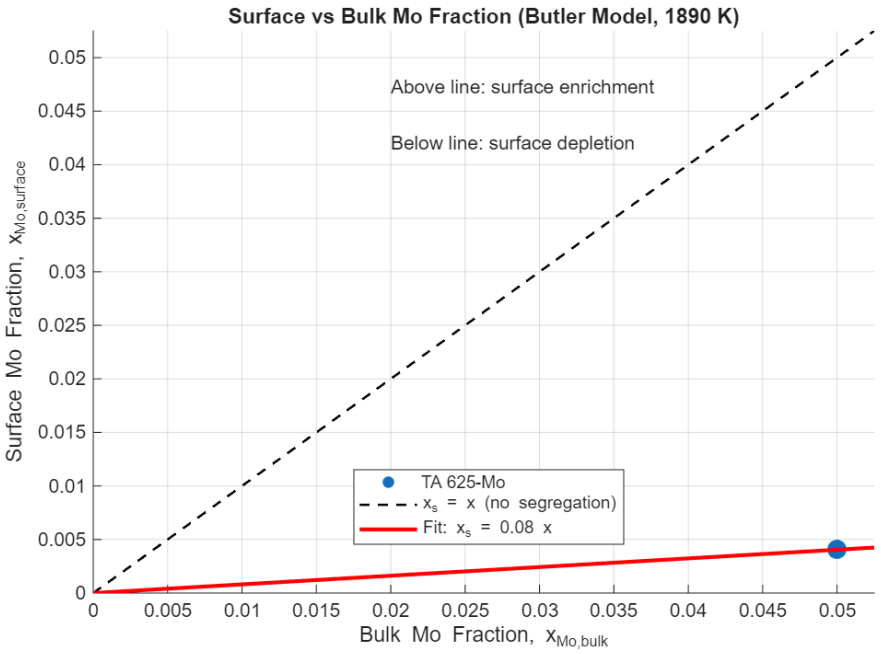

Figure 41: Surface versus bulk Mo fraction.

5.1.2.4 Comparison with Previous Studies

The present findings on surface segregation align closely with the experimental observations reported by Fu [7], who analysed post-test surface and bulk compositions of the ternary analog alloys using X-ray Photoelectron Spectroscopy (XPS) and Energy Dispersive X-ray Spectroscopy (EDS). Fu [7] observed chromium enrichment and nickel depletion at the surface of TA 718-Ni samples, whereas TA 625-Fe specimens exhibited inconsistent segregation trends for Ni and Cr but clear Fe depletion from the surface. To quantify these effects, Fu introduced empirical segregation coefficients of 0.976 (Ni), 1.137 (Cr), and 0.880 (Fe) as correction factors in his mass-loss model, improving the agreement between predicted and experimental results.

The thermodynamic predictions in the present study complement Fu's empirical observations by offering an equilibrium-based explanation for the same behaviour. The Butler-model calculations show that Ni is the most surface-active element, enriching at the liquid surface, while Fe and Mo are depleted and Cr remains nearly neutral. This hierarchy—Ni (enriched) > Cr (nearly neutral) > Fe (depleted) > Mo (strongly depleted)is consistent with Fu's finding that Fe remains in the bulk while Ni and Cr dominate near the surface. Moreover, the Butler model clarifies that the extent of segregation depends on both thermodynamic driving forces and kinetic constraints during levitation, confirming that compositional segregation governs surface-tension trends and evaporation kinetics in Ni–Cr–(Fe, Mo) alloy systems.

5.2 Experimental Results

The ternary analog (TA) systems were designed to reproduce the main alloying features of Inconel 625 and Inconel 718 while simplifying their multicomponent chemistries. Comparing density and surface-tension behaviour among these systems provides insight into how elemental substitutions, particularly Fe, Mo, and Ni, influence liquid-phase thermophysical properties. The following sections discuss these effects based on the ESL and EML measurements obtained in this study.

5.2.1 Inconel 625 vs TA 625-Mo / TA 625-Fe

Figure 14, Figure 15, Figure 16, Figure 22, Figure 23 and Figure 24 and shows the temperature-dependent density and surface-tension trends for Inconel 625 and its ternary analogues TA 625-Mo and TA 625-Fe.

A. **Density:**

TA 625-Mo exhibits the highest thermal expansivity, with a density slope nearly twice that of Inconel 625 (-1.96×10^{-3} kg m^{-3} K^{-1} compared to -1.07×10^{-3} kg m^{-3} K^{-1}). The pronounced decrease is attributed to the substitution of Mo for Nb and Cr, which reduces atomic packing efficiency and increases the molar volume of the liquid. TA 625-Fe shows a slightly lower density than Inconel 625 but retains a similar slope, indicating that Fe can act as an acceptable analog element for replicating thermal-expansion behavior in the liquid state.

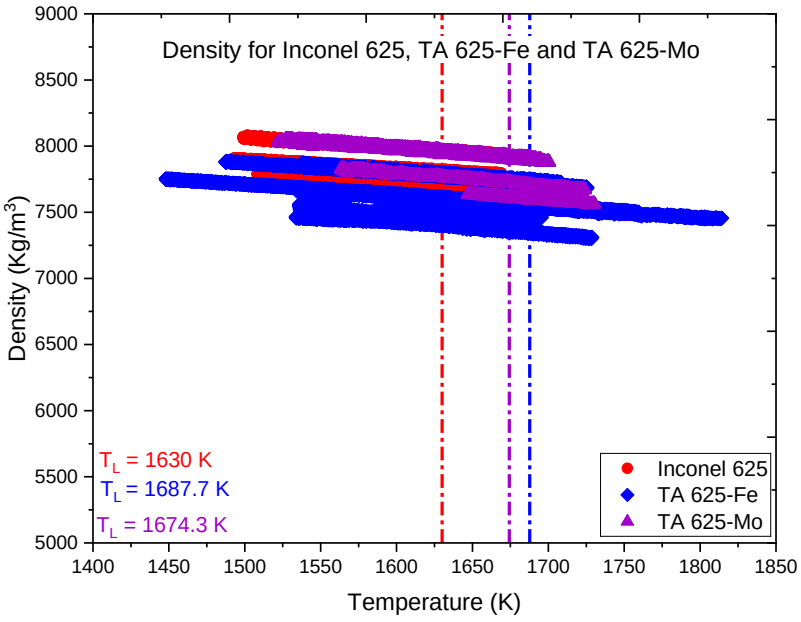

Figure 42: Density for Inconel 625, TA625-Mo and TA625-Fe (ESL Data)

B. Surface Tension:

The surface tension of TA 625-Fe (1.76 N m^{-1} at T_L) is comparable to that of Inconel 625 (1.83 N m^{-1}), whereas TA 625-Mo displays a marginally lower γ_0 (1.71 N m^{-1}) and a steeper temperature coefficient (-3.19×10^{-3} N m^{-1} K^{-1}). The reduction in γ_0 for the Mo-containing alloy can be linked to enhanced surface segregation of Mo atoms, which locally decreases surface-bond strength and lowers cohesive energy.

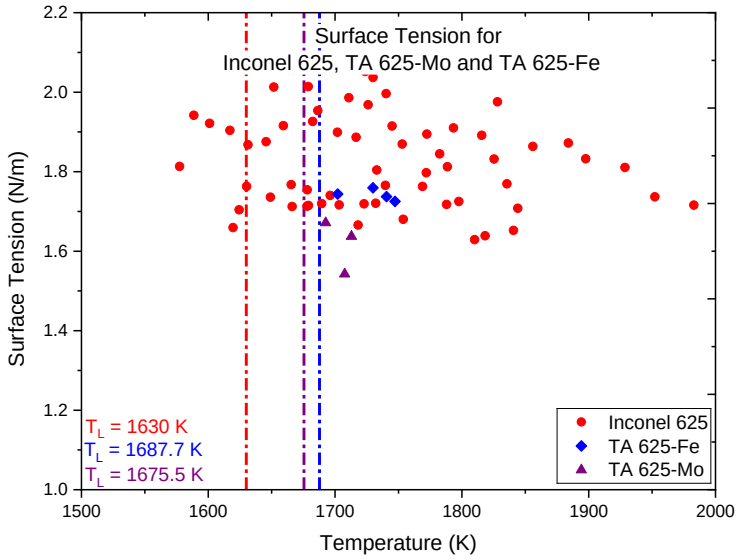

Figure 43: Surface Tension for Inconel 625, TA625-Mo and TA625-Fe

Overall, Fe substitution preserves both the density and surface-tension characteristics of Inconel 625 within experimental uncertainty, while Mo addition increases thermal expansivity and decreases surface cohesion

5.2.2 Inconel 718 vs TA 718-Ni/ TA 718-Fe

Figure 13, Figure 17, Figure 18, Figure 25 and Figure 26 illustrate the temperature-dependent density and surface-tension variations for Inconel 718 and its ternary analogues TA 718-Ni in Figure 18 and TA 718-Fe in Figure 17 obtained from electrostatic levitation (ESL) measurements.

A. Density

All three compositions exhibit a linear decrease in density with increasing temperature, characteristic of metallic liquids. Inconel 718 serves as the baseline, with a fitted liquid density ($\rho_0 = 7496.26 \pm 0.53$ kg m^{-3}) and a temperature coefficient of -1.03×10^{-3} kg m^{-3} K^{-1}.

TA 718-Ni exhibits the lowest slope (-0.59×10^{-3} kg m^{-3} K^{-1}) and a slightly reduced liquid density ($\rho_0 = 7374.10 \pm 0.51$ kg m^{-3}), indicating a lower thermal expansivity. This effect is linked to the replacement of Nb with Ni, which decreases atomic mass but increases local packing uniformity.

Conversely, TA 718-Fe shows a similar density-temperature relationship to the parent alloy ($\rho_0 = 7312.80 \pm 1.13$ kg m^{-3}; $\partial\rho/\partial T = -0.87 \times 10^{-3}$ kg m^{-3} K^{-1}), suggesting that Fe substitution preserves volumetric thermal expansion behavior within experimental uncertainty.

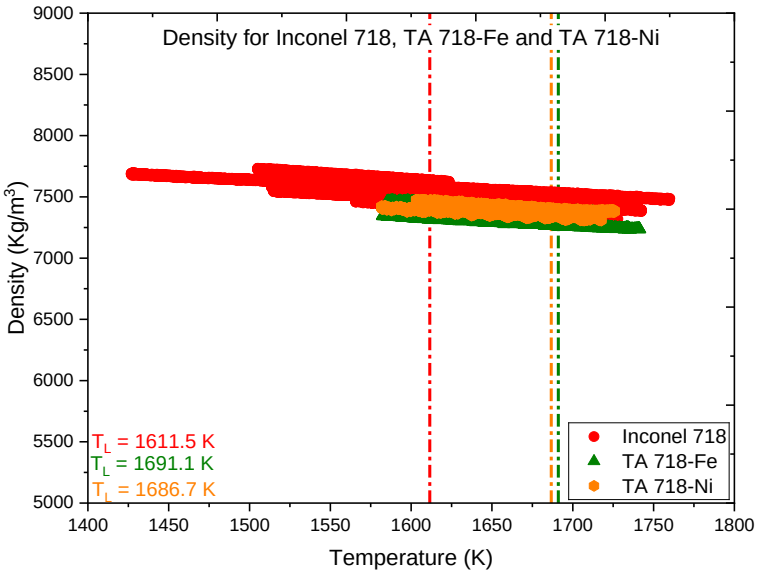

Figure 44: Density for Inconel 718, TA 718-Ni and TA 718-Fe

B. Surface Tension

The surface-tension trends exhibit similar linearity with temperature. Inconel 718 has a surface tension of $\gamma_o = 1.72 \pm 0.07$ N m^{-1} and $\partial\gamma/\partial T = -2.38 \times 10^{-5}$ N m^{-1} K^{-1}. TA 718-Fe retains nearly identical surface cohesion ($\gamma_o = 1.65 \pm 0.06$ N m^{-1}) but with a stronger temperature dependence ($\partial\gamma/\partial T = -8.68 \times 10^{-4}$ N m^{-1} K^{-1}), implying modestly enhanced surface activity of Fe atoms.

TA 718-Ni shows a comparable γ_o (1.65 ± 0.05 N m^{-1}) yet a steeper temperature coefficient (-5.58×10^{-3} N m^{-1} K^{-1}), suggesting more pronounced surface segregation of Ni and a corresponding reduction in cohesive energy at elevated temperatures.

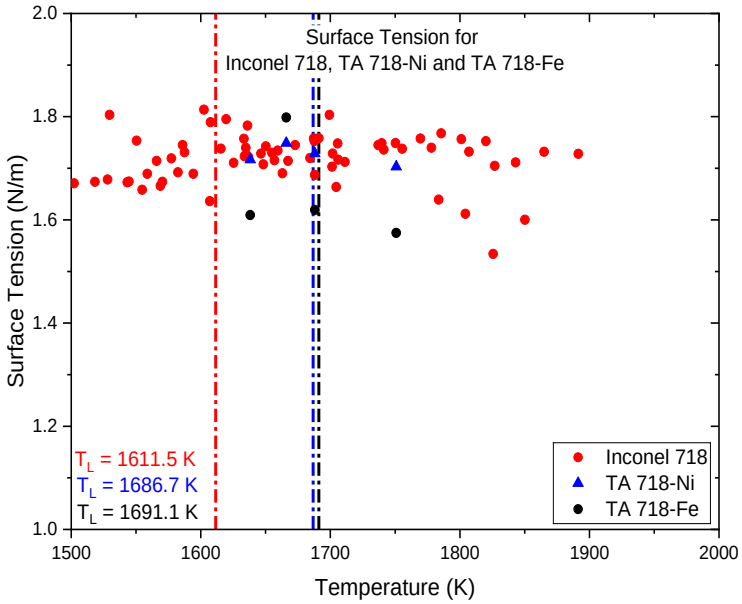

Figure 45: Surface Tension for Inconel 718, TA 718-Ni and TA 718-Fe

Summary

This chapter compared the modeled and experimental results for the thermophysical properties of Ni–Cr–(Fe, Mo) ternary analog alloys, which were developed as simplified versions of Inconel 625 and Inconel 718. Two main liquid-state properties were studied: density, using the Partial-Molar-Volume (PMV) model, and surface tension, using the Butler model. The model predictions were compared with experimental data obtained from electrostatic levitation (ESL) and electromagnetic levitation (EML) techniques.

The PMV model accurately represented how density changes with both temperature and composition. In all cases, the predicted density decreased linearly as temperature increased, which is typical for metallic liquids. The non-ideal PMV model, which includes small positive excess volume corrections, improved agreement with experiment, especially for alloys containing more iron. Across all alloys, the difference between model and experiment remained within about two %. This shows that the PMV model gives reliable predictions of liquid density for Ni–Cr–based systems.

The Butler model correctly predicted a linear decrease in surface tension with temperature and the correct order of magnitude among the alloys (TA 718-Fe highest, followed by TA 718-Ni, TA 625-Mo, and TA 625-Fe). However, the predicted values were generally 5 to 15 % higher than the ESL measurements. This difference is expected because the Butler model assumes the

surface is in full equilibrium, while ESL experiments capture a transient state that may not allow complete surface segregation. Studies by Xiao and Brillo [25] reported similar results for Fe–Ni, Fe–Cr, and Ni–Cr alloys, where the measured surface tension was lower than the predicted value due to small amounts of oxygen adsorption and limited surface equilibration. The larger deviations seen in Fe-rich alloys compared to Mo-containing ones are consistent with stronger oxygen affinity and slower diffusion of Fe atoms, which delay full surface adjustment.

When comparing the ternary analogs with the industrial superalloys, Fe substitution was found to preserve both density and surface tension within experimental uncertainty. Mo addition slightly reduced surface cohesion and increased thermal expansivity. These results show that the ternary analog systems are suitable simplified models for studying the behavior of complex superalloys.

In summary, the PMV and Butler models, supported by high-temperature levitation data, describe the temperature-dependent behavior of density and surface tension in these alloy systems with good accuracy. The results confirm that the ternary analog approach can be used to understand the key factors controlling the liquid-state properties of nickel-based superalloys.

CHAPTER 6. Uncertainty Analysis

An uncertainty analysis is fundamental to validating thermophysical property measurements in containerless materials processing. In the absence of physical contact and under extreme temperature conditions, even small measurement deviations can significantly affect the calculated density and surface tension. Therefore, the credibility of any dataset obtained through levitation techniques must be anchored in a well-established uncertainty framework.

Although no new numerical propagation is derived in this study, the reliability of the results is interpreted through the Guide to the Expression of Uncertainty in Measurement (GUM, 1995) and previously published benchmark analyses by Nawer et al. [29] [30] [5] provide benchmark analyses of the precision and uncertainty sources associated with the NASA Marshall Space Flight Center Electrostatic Levitation (MSFC ESL) facility and the TEMPUS Electromagnetic Levitation (EML) facility. Together, these facilities form the benchmark basis for quantifying the uncertainty ranges associated with the present study's surface-tension and density results.

6.1 Standard Uncertainty and Propagation

Evaluation of uncertainty follows the framework recommended by GUM (1995). If a measured quantity y is determined from several independent input quantities $x_1, x_2, \ldots . x_n$ through a functional relationship $y = f(x_1, x_2, \ldots . x_n)$, the combined standard uncertainty is obtained by the law of propagation of uncertainty [19]:

$$u_c(y) = \sqrt{\sum_{i=1}^{n} \left(\frac{\partial f}{\partial x_i}\right)^2 u^2(x_i)} \tag{43}$$

- Type A uncertainty: estimated statistically from repeated measurements.
- Type B uncertainty: evaluated from calibration data, manufacturer specifications, or prior knowledge.

6.2 Temperature

Temperature in levitation experiments is measured using a two-colour (ratio) pyrometer, which calculates temperature from two radiance signals corresponding to distinct wavelengths. The true temperature *T* can be expressed as:

$$T = \left(\frac{1}{T_P} + \frac{1}{T_L} - \frac{1}{T_{PL}}\right)^{-1} \tag{44}$$

where: T_P is apparent temperature, T_{PL} is the apparent liquidus, and T_L the true liquidus, all in Kelvin.

Taking partial derivatives with respect to T_P, T_L and T_{PL}:

$$\frac{\partial T}{\partial T_P} = \frac{T^2}{{T_P}^2}, \qquad \frac{\partial T}{\partial T_L} = \frac{T^2}{{T_L}^2} \quad \text{and} \quad \frac{\partial T}{\partial T_{PL}} = \frac{T^2}{{T_{PL}}^2} \tag{45}$$

By applying standard uncertainty propagation, the combined uncertainty in the calculated temperature is given by:

$$\frac{u_c(T)}{T} = T\sqrt{\left(\frac{1}{T_P}\left(\frac{u(T_A)}{T_P}\right) + \frac{1}{T_{PL}}\left(\frac{u(T_{LA})}{T_{PL}}\right)\right)^2 + \frac{1}{{T_L}^2}\left(\frac{u(T_L)}{T_L}\right)^2} \tag{46}$$

Typical temperature uncertainties are 0.7–0.8% (MSFC ESL) [29]and ≈ 0.4% (TEMPUS EML) [31]. In this study, temperature uncertainties were evaluated for both the MSFC ESL TA625-Fe alloy and the TEMPUS EML Inconel 625 alloy. Figure 46 illustrates the apparent liquidus and apparent temperature regions used for the Type A uncertainty analysis.

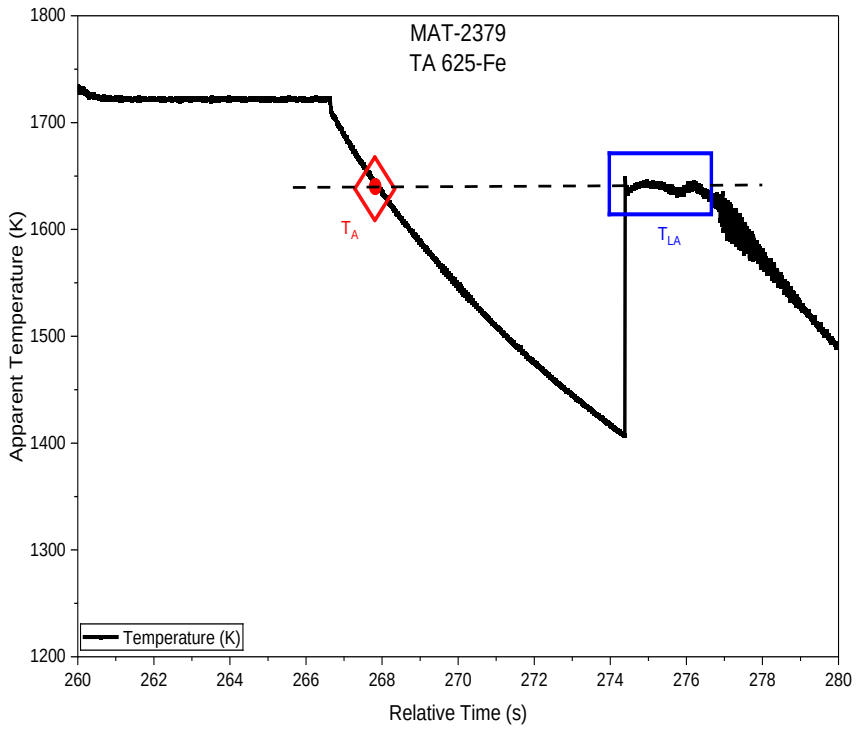

Figure 46: A typical melt cycle showing the time temperature profile during containerless processing of TA 625-Fe alloy using electrostatic levitation

The dashed line marks the apparent liquidus following recalescence. Averaging the data within the blue rectangle yields an apparent liquidus temperature of

$$T_{PL} = 1639.40 \pm 3.00\,\mathrm{K}$$

based on $N = 160$ points.

The red rectangle identifies the region used to determine the apparent temperature near the liquidus. Fitting the data within this region and evaluating the deviation of the selected point from the fitted curve give

$$T_P = 1635.42 \pm 4.55\,\mathrm{K}$$

for a sample size of $N = 31$.

The true liquidus temperature for this alloy was measured independently using differential scanning calorimetry (DSC), resulting in

$$T_L = 1687.7 \pm 5.0\,\mathrm{K}$$

Type A uncertainties are obtained directly from the standard deviations of $T_P$and T_{PL}:

$$\frac{u_c(T_P)}{T_P} = \frac{4.55}{1635.42}, \frac{u_c(T_{PL})}{T_{PL}} = \frac{3.00}{1639.40}$$

and are combined with the Type B uncertainty associated with the DSC liquidus measurement,

$$\frac{u_c(T_L)}{T_L} = \frac{5.0}{1687.7}$$

Applying the analytic GUM propagation formula (Eq. 46), the combined effect of these three uncertainty sources yields an overall temperature uncertainty of

$$u_c(T) \approx 6.71K$$

corresponding to a relative uncertainty of

$$\frac{u_c(T)}{T} \approx 0.403\%.$$

Thus, the uncertainty at the liquidus for this data point is approximately 6.71 K, or 0.403%

A similar temperature uncertainty analysis was performed for the TEMPUS electromagnetic levitation (EML) measurements of the Inconel 625 alloy obtained during parabolic flight experiments. The apparent temperature T_P was determined from the data segment immediately preceding nucleation. Averaging the values within this region yielded

$$T_P = 1628.71 \pm 14.52\ \text{K}$$

based on a sample size of $N = 354$.

The apparent liquidus temperature T_{PL} was extracted from the recalescence plateau following recalescence, where the temperature signal becomes nearly stationary. The mean and standard deviation of the points in this region were

$$T_{PL} = 1626.60 \pm 0.44\ \text{K}$$

for a sample size of $N = 132$.

The true liquidus temperature for this alloy, determined independently using DSC, was

$$T_L = 1630 \pm 5\ \text{K}$$

The Type A uncertainties are obtained from the measured standard deviations of T_P and T_{PL}, while the Type B uncertainty is provided by the manufacturer. These three contributions were combined using the analytic GUM propagation approach (Eq. 46). The resulting true temperature for this data point is

$$T = 1632.12\ \text{K}$$

with a combined standard uncertainty of

$$u_c(T) \approx 15.5\ \text{K}, \frac{u_c(T)}{T} \approx 0.97\%$$

Using the corrected temperature value $T = 1632.12\ \text{K}$ the resulting combined standard uncertainty is

$$u_c(T) = 15.8\ \text{K}.$$

6.3 Surface tension

Surface tension (γ) is obtained from the natural oscillation frequency of a levitated droplet using the Rayleigh relation:

$$\gamma = \frac{3\pi m f^2}{8} \tag{47}$$

Applying Eq. (5.1) yields the propagated uncertainty:

$$\frac{u_c(\gamma)}{\gamma} = \sqrt{(\frac{u(m)}{m})^2 + 4(\frac{u(f)}{f})^2} \tag{48}$$

At the MSFC ESL, sub-pixel imaging gives $u(r)/r \approx 0.48\%$ and $u(fn)/fn \approx 0.7\%$ producing a total surface-tension uncertainty of ≈ 1.4% [29].

At the TEMPUS EML, the shorter oscillation window and microgravity turbulence raise this value to ≈ 3.9% [31].

6.4 Density

The liquid density is determined from droplet mass and instantaneous volume:

$$\rho = \frac{m}{V} \tag{49}$$

Propagation of uncertainty gives

$$\frac{u(\rho)}{\rho} = \sqrt{\left(\frac{u(V)}{V}\right)^2 + \left(\frac{u(m)}{m}\right)^2} \tag{50}$$

Measured uncertainties are ≈ 1.81% (MSFC ESL) [29] and ≈ 1.8% (TEMPUS EML) [31], consistent with published results by Nawer et al.

6.5 Summary of Facility Performance

The uncertainty values summarized in Table 9 are based on measurements using liquid Pt, liquid Au, and CMSX-4® Plus under comparable levitation conditions. Although this study investigates different alloy systems, the same measurement principles and error sources apply. Therefore, these published benchmarks are used as reference uncertainty ranges for interpreting the present density and surface-tension results obtained from the MSFC ESL and TEMPUS EML facilities.

Table 9: Summary of Relative and Combined Standard Uncertainties for MSFC ESL (Pt), TEMPUS EML (Au), and CMSX-4® Plus (SLS)

Contributing Factors (%)	NASA MSFC ESL (Pt) [29]	NASA MSFC ESL (TA625-Fe)	NASA MSFC ESL (CMSX-4® Plus) [30]	TEMPUS EML (Au) [31]	TEMPUS EML (Inconel 625)
Uncertainty of temperature, $u(T)/T$	0.76	0.45	0.66	0.42	0.95
Uncertainty of mass, $u(m)/m$	0.33		0.93	0.01	
Uncertainty of radius, $u(r)/r$	0.48		0.51	3.68	
Uncertainty of volume, $u(V)/V$	1.46		1.55	11.04	
Uncertainty of frequency, $u(f_n)/f_n$	0.67		0.26	1.95	
Combined uncertainty of density, $u_c(\rho)/\rho$	1.49		1.81	1.36	
Combined uncertainty of surface tension, $u_c(\gamma)/\gamma$	1.38		1.06	3.91	

6.6 Evaporation of Sample Material

Evaporation was controlled operationally and treated as a data-quality gate. For every run, pre-/post-test masses were recorded; datasets were accepted only when total mass loss was < 5% of the initial mass, and any run exceeding this limit was excluded to avoid composition drift in the derived density and surface-tension results.

This practice is consistent with prior containerless studies by Nawer [29] [31] and Fu [7]. Nawer and co-workers (ISS-EML) showed that processing in inert shielding gas keeps losses small and predictable: mission totals for Ni-based superalloys were on the order of 0.24–0.25 mg, with near-real-time Tox-Tracker control (empirical, conservative) agreeing with

Langmuir-based post-analysis and deposited-layer estimates on facility hardware [7]. Elemental partitioning (Fe/Cr/Ni) from SEM/EDX matched model predictions, confirming that evaporation remained well below toxicity thresholds and did not compromise property measurements. In complementary ESL work on Ni-Cr-Fe analogs, Fu [7] implemented a Langmuir + CALPHAD framework and quantified model inputs and per-step combined uncertainty (≈ 9.03% at a time step). Experimentally, microbalance precision gave an absolute mass-loss uncertainty of ≈ 0.0007 mg for ~40 mg samples, while observed total losses for most samples were ~2.8–4.5%; an outlier at 7.1% illustrates why a 5% acceptance threshold is appropriate.

Guided by these findings, the present study reports only datasets acquired under low-evaporation conditions (< 5%), ensuring that the measured density and surface tension reflect alloy behaviour rather than evaporation-induced composition change.

6.7 Summary of Surface, Bulk, and Wet-Chemistry Composition Analyses

To assess potential composition changes arising from arc melting, electrostatic levitation (ESL), and associated high-temperature mass loss, three complementary analytical techniques were employed (Appendix L): X-ray Photoelectron Spectroscopy (XPS) for surface chemistry, Energy Dispersive X-ray Spectroscopy (EDS) for bulk composition, and Direct Current Plasma Emission Spectroscopy (DCPES) for high-accuracy wet-chemistry verification. XPS (ESCA) measurements were performed on five droplets (MAT-2351, MAT-2353, MAT-2378, MAT-2379, and MAT-2380) using a Kratos Ultra DLD system operated under ultra-high vacuum. After removing ~20 nm of surface contamination with Ar^+ sputtering, quantification of Ni 3p, Cr 2p, and Fe 3p peaks revealed clear evidence of surface segregation: TA-718-Ni samples consistently exhibited surface Ni enrichment and Cr depletion, consistent with Cr's higher volatility at molten temperatures, while TA-625-Fe samples showed more variable behavior, including cases of Cr-rich surface layers (Appendix L).

Bulk composition was evaluated using SEM-EDS on polished cross sections. The EDS results showed excellent internal uniformity, with standard deviations generally below 2 wt%, and compositions that remained close to their intended ternary formulations. TA-718-Ni droplets maintained approximately 60–65 wt% Ni, 14–19 wt% Cr, and ~21 wt% Fe, while the TA-625-Fe droplets remained within 73–78 wt% Ni, 5–5.5 wt% Fe, and 17–22 wt% Cr (Appendix L). These results indicate that measured mass-loss levels (<5%) introduced only minimal changes

to the bulk alloy chemistry, consistent with the predicted small composition drift from the non-ideal Langmuir evaporation model.

Finally, wet-chemistry analysis via DCPES (ASTM E1097-12) provided the most accurate benchmark of the overall alloy composition, independent of surface effects. Although obtained later in the analysis sequence, these measurements serve as the highest-confidence reference for initial input compositions and for validating model-predicted changes in elemental concentrations.

Taken together, the XPS, EDS, and DCPES results present a good picture: surface chemistry is sensitive and undergoes measurable Ni/Cr redistribution, whereas the bulk alloy composition remains stable and within uncertainty limits. This convergence of surface, bulk, and wet-chemistry evidence confirms that limited evaporation during ESL processing does not significantly alter the internal alloy chemistry, supporting the accuracy and assumptions of the evaporation modeling presented in this thesis.

6.8 Chapter Summary

This chapter validated the reliability of the measured thermophysical properties through established uncertainty frameworks. Using GUM (1995) and benchmark analyses by Nawer [29] , uncertainty in temperature, mass, radius, and frequency was shown to remain within 1–4%, aligning with results from MSFC ESL and TEMPUS EML facilities.

Evaporation effects were minimal, consistent with Nawer [32] and Fu [7], where total mass losses remained below 5% under inert-gas conditions. Overall, the uncertainty evaluation confirms that the measured density and surface tension accurately represent the behaviour of the studied Ni-Cr-Fe and Ni-Cr-Mo based alloys.

CHAPTER 7. Conclusion and Future Work

This thesis presented an integrated experimental and computational study of the thermophysical properties of Ni–Cr–(Fe, Mo) ternary analog alloys, designed as simplified representations of the industrial superalloys Inconel 625 and Inconel 718. The work aimed to establish reliable models and experimental data for liquid-state density and surface tension, properties that critically influence melt behavior, defect formation, and solidification processes in advanced alloy manufacturing and space-based materials processing.

Containerless experiments were conducted using electrostatic levitation (ESL) at NASA's Marshall Space Flight Center and electromagnetic levitation (EML) during parabolic flights, allowing property measurement under both normal and reduced-gravity conditions without contamination or convection. The data were analyzed using the Partial-Molar-Volume (PMV) model for density and the Butler thermodynamic model for surface tension, creating a consistent framework for direct comparison between experimental observations and thermodynamic predictions.

7.1 Key Findings

The key findings in this work are:

1. Accurate Representation of Density Behavior
   The PMV model successfully reproduced the temperature dependence of liquid density for all ternary analog alloys. The predicted densities decreased linearly with increasing temperature, reflecting the thermal expansion of metallic liquids. This behavior was consistent across all compositions and confirmed the predictive accuracy of the PMV approach.
2. Impact of Non-Ideal Mixing
   Incorporating positive excess-volume terms into the PMV formulation improved agreement with experimental data, particularly for Fe-rich alloys where atomic size differences and weak interactions cause small deviations from ideal mixing. The resulting difference between modeled and experimental values was within approximately 2 %, confirming the model's robustness for practical thermophysical predictions.
3. Temperature and Composition Dependence of Surface Tension

The Butler thermodynamic model predicted a linear decrease in surface tension with increasing temperature, consistent with experimental observations. The correct ordering of alloys (TA 718-Fe > TA 718-Ni > TA 625-Mo > TA 625-Fe) was obtained, reflecting how the addition of Fe and Mo modifies the cohesive forces at the liquid surface.

4. Model–Experiment Agreement and Surface Effects

   The Butler model generally overestimated the measured surface tension by 5–15%, which is attributed to incomplete surface equilibration in ESL experiments. Xiao and Brillo [25] reported similar discrepancies (10–20 %) for binary Fe–Ni, Fe–Cr, and Ni–Cr systems at 0.03–0.10 at. % O_2. In this study, wet-chemical analysis (Appendix K) confirmed oxygen levels < 0.05 at. %, placing our samples within the same trace-oxygen range and validating that the observed 5–15 % offset is consistent with prior findings. The predicted surface segregation behavior from the Butler model is consistent with the experimentally observed segregation trends, confirming that the model captures the essential interfacial chemistry of the alloys.

5. Model–Experiment Agreement and Surface Effects

   The Butler model correctly predicts the segregation order at 1890 K, with nickel enriched, chromium nearly neutral, iron depleted, and molybdenum strongly depleted. XPS measurements in Appendix L follow the same hierarchy, confirming that the predicted interfacial composition is realized during levitation. This agreement shows that surface segregation controls the effective surface chemistry and that the Butler formulation provides a reliable basis for interpreting the measured surface tension and evaporation behaviour.

6. Validation of the Analog Alloy Approach

   The ternary analog systems effectively reproduced the dominant thermophysical behavior of the complex industrial alloys. This confirms that simplified analog compositions can be used to study fundamental mechanisms such as temperature dependence, mixing effects, and surface segregation without the interference of minor alloying elements present in full superalloys. It should be noted that although the ternary analog approach is extremely beneficial for benchmarking and predicting the behaviour of complex industrial alloys, these simplified compositions are not intended for commercial production and will not be manufactured or sold for industrial use.

7. Weaknesses of the Analog-Alloy Approach

Despite accurately reproducing major thermophysical trends, the analog systems remain highly sensitive to trace oxygen. Even at O < 0.05 at. %, oxygen adsorption caused 5–15 % reductions in measured surface tension, outweighing effects from alloying variations. This confirms that oxygen contamination dominates surface behavior more strongly than composition, representing the main limitation of the analog-alloy approach under containerless conditions

8. Contribution to ICME and Space Materials Research

   The combined ESL–EML data and modelling form a validated framework that supports the Integrated Computational Materials Engineering (ICME) approach by linking thermodynamic models, experimental data, and processing conditions. The results also provide benchmark values for future microgravity experiments and process simulations, contributing to the broader database of reference thermophysical properties for Ni-based alloys.

7.2 Future Work

While the objectives of this thesis have been met, several research directions can further advance understanding of thermophysical behavior and extend the applicability of the models developed.

1. Extension to Quaternary and Quinary Systems

   Future studies should investigate higher-order derivatives such as Ni–Cr–Fe–Mo and Ni–Cr–Fe–Nb to account for multi-solute interactions that occur in real superalloy chemistries. These systems will provide a more complete picture of how combined solute effects influence density and surface tension and will serve as direct validation points for CALPHAD-based thermodynamic predictions.

2. Comprehensive Property Database Development

   Additional high-temperature properties, including viscosity, thermal diffusivity, and electrical conductivity, should be measured using oscillating-drop and modulation-calorimetry techniques. A complete thermophysical dataset will enable accurate input for computational simulations of solidification and additive manufacturing, improving process control and defect prediction.

3. Long-Duration Microgravity Experiments

   Conducting extended experiments aboard the International Space Station (ISS) using the MSL-EML facility will provide data free from convection and container effects.

Such measurements will refine temperature-dependent coefficients in the PMV and Butler models and help isolate thermodynamic contributions from external effects.

4. Langmuir Adsorption Model for Multicomponent Systems

   A major future research direction involves extending the Langmuir adsorption model, originally proposed by Xiao et al. [25] for binary liquid alloys, to ternary and quaternary systems. Xiao's Langmuir–Butler hybrid framework treats surface segregation as a dynamic adsorption process where solute atoms compete for a finite number of surface sites.

5. Controlled Oxygen-Level Experiments

   To quantify the influence of oxygen on surface tension, systematic ESL and EML experiments should be performed at varying oxygen partial pressures (10^{-6}–10^{-3} atm). These studies will identify threshold concentrations where oxygen adsorption overtakes compositional effects, helping decouple chemical and environmental contributions to surface energy. Such results will provide critical input for refining the Butler–Langmuir model and improving reproducibility in containerless measurements.

7.3 Closing Remarks

This research has advanced the understanding of thermophysical properties in Ni–Cr–Fe and Ni–Cr–Mo ternary alloys through a combination of precise containerless experiments and thermodynamic modeling. The agreement between the partial molar volume framework and the Butler model with experimental measurements confirms their suitability for describing high temperature liquid behavior in Ni based systems. The methodologies and results presented here contribute to both scientific and industrial progress. Scientifically, they provide validated data for model development and calibration. Industrially, they support more accurate simulations of alloy solidification, welding, and additive manufacturing.

A final reflection concerns the industrial relevance of studying ternary analog alloys. Although commercial superalloys contain many alloying elements and complex interactions, ternary systems allow the fundamental thermodynamic behavior of key constituents to be isolated and understood with clarity. Demonstrating that thermodynamic frameworks such as activity modeling, partial molar volume theory, and interfacial models remain accurate in these simplified Ni–Cr–Fe and Ni–Cr–Mo systems establish the scientific foundation needed to extend these models to full industrial compositions. In practice, this means that validated behavior observed in ternaries strengthens confidence in predictive simulations used for

welding, casting, additive manufacturing, and high temperature design. By confirming that core thermodynamic theories hold under controlled ternary conditions, this work supports the development of reliable computational tools and process models for the advanced materials that power aerospace, energy, and space technologies.

An important question is whether ternary analogs will continue to be used. The answer is yes. Ternary systems remain essential because they offer controlled compositions that reveal the fundamental thermodynamic and interfacial interactions that govern the behavior of more complex superalloys. They enable clear validation of theoretical models, provide reliable high temperature data, and serve as practical testbeds for exploring evaporation, surface segregation, and liquid structure. Although industrial applications ultimately rely on multicomponent alloys, the accuracy of those large-scale simulations depends heavily on validated behavior in simplified systems. Therefore, ternary analogs will continue to serve as a scientific bridge that connects theory, modeling, and full-scale alloy design.

Looking forward, the incorporation of Langmuir adsorption-based modelling for ternary systems represents a transformative step toward understanding interfacial phenomena at a molecular level. When combined with data driven and atomistic approaches, this will enable next generation to predictive models that link alloy composition, thermophysical behavior, and process performance, thereby supporting the design of sustainable, high-performance materials for aerospace, energy, and space applications.

Appendix A. Experimental Data Collection Timeline

Date	Name	Alloy Name	Method
2020-09-23	01_20200923_SCE	Inconel 625	Parabolic Flight
2020-09-23	02_20200923_SCE	Inconel 625	Parabolic Flight
2020-09-23	04_20200923_SCE	Inconel 625	Parabolic Flight
2020-09-23	05_20200923_SCE	Inconel 625	Parabolic Flight
2020-09-23	09_20200923_SCE	Inconel 625	Parabolic Flight
2020-09-23	10_20200923_SCE	Inconel 625	Parabolic Flight
2023-09-12	10_20230912_SCE	Inconel 718	Parabolic Flight
2023-09-12	11_20230912_SCE	Inconel 718	Parabolic Flight
2023-09-12	12_20230912_SCE	Inconel 718	Parabolic Flight
2023-09-12	13_20230912_SCE	Inconel 718	Parabolic Flight
2023-09-12	14_20230912_SCE	Inconel 718	Parabolic Flight
2023-09-12	30_20230912_SCE	Inconel 718	Parabolic Flight
2024-09-19	07_20240919_SCE	TA625-Mo	Parabolic Flight
2024-09-19	08_20240919_SCE	TA625-Mo	Parabolic Flight
2024-09-19	09_20240919_SCE	TA625-Mo	Parabolic Flight
2024-09-19	10_20240919_SCE	TA625-Mo	Parabolic Flight
2024-09-19	11_20240919_SCE	TA718-Ni	Parabolic Flight
2024-09-19	12_20240919_SCE	TA718-Ni	Parabolic Flight
2024-09-19	13_20240919_SCE	TA718-Ni	Parabolic Flight
2024-09-19	15_20240919_SCE	TA718-Ni	Parabolic Flight
2024-01-26	MAT-2038	Inconel 625	ESL
2024-01-26	MAT-2039	Inconel 625	ESL
2024-01-31	MAT-2059	Inconel 625	ESL
2024-02-05	MAT-2079	Inconel 625	ESL
2024-06-06	MAT-2220	Inconel 625	ESL
2024-06-06	MAT-2226	Inconel 625	ESL
2024-08-28	MAT-2291	Inconel 625	ESL
2024-01-24	MAT-2030	Inconel 718	ESL
2024-01-24	MAT-2031	Inconel 718	ESL

2024-02-01	MAT-2049	Inconel 718	ESL
2024-02-05	MAT-2085	Inconel 718	ESL
2024-02-05	MAT-2087	Inconel 718	ESL
2024-02-05	MAT-2094	Inconel 718	ESL
2024-06-05	MAT-2204	Inconel 718	ESL
2024-08-29	MAT-2278	Inconel 718	ESL
2024-11-18	MAT-2351	TA625-Fe	ESL
2024-11-18	MAT-2379	TA625-Fe	ESL
2024-11-21	MAT-2417	TA625-Fe	ESL
2024-11-21	MAT-2418	TA625-Fe	ESL
2024-11-21	MAT-2420	TA625-Fe	ESL
2024-12-18	MAT-2428	TA625-Fe	ESL
2024-12-17	MAT-2430	TA625-Fe	ESL
2024-12-17	MAT-2431	TA625-Fe	ESL
2024-12-17	MAT-2432	TA625-Fe	ESL
2025-05-06	MAT-2501	TA625-Fe	ESL
2025-05-06	MAT-2503	TA625-Fe	ESL
2024-10-31	MAT-2339	TA625-Mo	ESL
2024-11-21	MAT-2424	TA625-Mo	ESL
2024-11-21	MAT-2425	TA625-Mo	ESL
2024-12-18	MAT-2433	TA625-Mo	ESL
2024-12-18	MAT-2434	TA625-Mo	ESL
2024-12-18	MAT-2435	TA625-Mo	ESL
2024-12-18	MAT-2436	TA625-Mo	ESL
2024-12-18	MAT-2437	TA625-Mo	ESL
2024-11-18	MAT-2376	TA718-Fe	ESL
2024-11-19	MAT-2377	TA718-Fe	ESL
2024-11-19	MAT-2381	TA718-Fe	ESL
2024-11-20	MAT-2413	TA718-Fe	ESL
2025-05-08	MAT-2483	TA718-Fe	ESL
2024-11-18	MAT-2349	TA718-Ni	ESL
2024-11-18	MAT-2350	TA718-Ni	ESL
2024-11-20	MAT-2407	TA718-Ni	ESL

2024-11-20	MAT-2411	TA718-Ni	ESL
2025-05-06	MAT-2473	TA718-Ni	ESL

Appendix B. Sample Acceptance Data Packages

DLR / ISS USOC / MUSC	Historical Record - Lebenslaufkarte			
TEMPUS Parabolic flight, 2020	Science team Sample composition **Inconel 625** Sample ID / # 1		Priority	
	Mass [g] **1.0435** Average diameter [mm] 6.0		Minimal diameter [mm] Maximal diameter [mm]	6.58 4.96
Requirements for storage				
Requirements for handling before and during integration				

Date	Activity, Procedure	Remarks	performed by
10.2.20	Arc furnace		Xiao Xiao
22.9.20	integrated in chamber #2 Pos #1		C. Dreißigacker
22.11.20	shipped to L. Lichler (TU Graz)		M. Beckers

DLR / ISS USOC / MUSC	Historical Record - Lebenslaufkarte			
TEMPUS Parabolic flight, 2020	Science team Sample composition **Inconel 625** Sample ID / # 2		Priority	
	Mass [g] **1.0081** Average diameter [mm] 6.0		Minimal diameter [mm] Maximal diameter [mm]	6.65 4.84
Requirements for storage				
Requirements for handling before and during integration				

Date	Activity, Procedure	Remarks	performed by
10.2.20	Arc furnace		Xiao Xiao
10.9.18	Integrated to lock #8, shaft in Graz (Tr)		M. Beckers
22.9.20	Integrated to chamber #2 Pos #1		C. Dreißigacker
2.10.20	Deintegrated and stored in cabinet (locked) ~Incoral Lft #2 1,008 g		M. Beckers
22.10.20	shipped to L. Lichler (TU Graz)		M. Beckers

The sample labelled #120-PF-IN718#A was processed on day 1, parabolas 10-14 (14 was SCE) and parabola 30.
The undercooling in the final parabola was ~120°C (superheat to 1650°C).

The other sample was not processed but integrated to the sample chamber as a backup.

	Historical Record Sheet
TEMPUS Parabolic flight, 2022 2022 Covid cancelled Run in PF2023	Science team Matson Sample composition **Inconel 718** Sample ID: #120-PF-IN718#A Priority: 1 Mass [g] 1.1802 Minimal diameter [mm] 6.46 Average diameter [mm] 6.50 Maximal diameter [mm] 6.76
Requirements for storage	The samples were placed in the bottles labelled with sample ID.
Requirements for handling before and during integration	Default procedure

Date	Activity, Procedure	Remarks	performed by
03.05.2022	Cut from IN718 rod		Xiao
06.05.2022	Processed by arc-melter		Xiao
13.05.2022	EML processed for 1 minute	1.1802 g	Xiao
10.08.2022	Delivered to MUSC		Xiao
11.8.22	Received, stored under Ar		Beckers
2.9.22	Re-integrated in Rack #5 core #32, stored inside under Vacuum, Ar		—
07.09.22	Integrated to SCH#1 pos. 8		YANG
12.9.22	Deintegrated @DLR		Beckers
29.8.23	Re-Integrated to Rack #5 ; stored under Ar		—
7.9.23	Integrated to SCH 2 Pos #4		—
12.9.23	Processed on day 1 Par #10-14, #30		TBeckers
5.10.23	Deintegrated from SCH2 Sample passed to M. Kolbe (DLR)		Beckers

	Historical Record Sheet
TEMPUS Parabolic flight, 2022	Science team Matson Sample composition **Inconel 718** Sample ID: #120-PF-IN718#B Priority: 2 Mass [g] 1.1836 Minimal diameter [mm] 6.38 Average diameter [mm] 6.51 Maximal diameter [mm] 6.74
Requirements for storage	The samples were placed in the bottles labelled with sample ID.
Requirements for handling before and during integration	Default procedure

Date	Activity, Procedure	Remarks	performed by
03.05.2022	Cut from IN718 rod		Xiao
06.05.2022	Processed by arc-melter		Xiao
13.05.2022	EML processed for 1 minute	1.1836 g	Xiao
10.08.2022	Delivered to MUSC		Xiao
11.8.22	Received, stored under Ar		Beckers
2.9.22	Re-integrated to Rack #5 (silver) core #12, stored inside under Ar		Yang
07.09.22	Integrated to SCH #1 pos. 9		YANG
12.9.22	Deintegrated @DLR		Beckers
29.8.23	Re-Integrated to Rack #5 ; stored under		—
7.9.23	Integrated to SCH 2 Pos #5 ; stored under Vac		—
12.9.23	Deintegrated from SCH 2 and stored		—
5.10.23	Sample passed to M. Kolbe for analysis		—

Appendix C. ESL Experimental Dataset Summary

MAT Number	Alloy System	Mass (mg)	Holding Temperature (K)	Natural Frequency (Hz)	Surface Tension (N/m)
MAT-2061	Inconel 625	35.2866	1677.99	203.003	1.713152
MAT-2062	Inconel 625	33.9511	1696.19	208.59	1.740291
MAT-2065	Inconel 625	38.3626	1787.995	194.946	1.717583
MAT-2078	Inconel 625	34.577	1666.165	205.017	1.712175
MAT-2079	Inconel 625	36.9111	1732.11	198.914	1.720556
MAT-2081	Inconel 625	35.7238	1678.03	204.163	1.754256
MAT-2082	Inconel 625	38.3982	1722.87	194.946	1.719177
MAT-2083	Inconel 625	36.0866	1703.32	200.928	1.716359
MAT-2034	Inconel 718	35.2606	1701.77	203.979	1.72839
MAT-2036	Inconel 718	36.8062	1706	198.975	1.716719
MAT-2046	Inconel 718	38.2633	1750.305	196.96	1.748717
MAT-2047	Inconel 718	37.2156	1701.325	197.083	1.70296
MAT-2048	Inconel 718	39.0246	1711.265	192.993	1.71239
MAT-2067	Inconel 718	35.8346	1705.705	203.491	1.748132
MAT-2068	Inconel 718	34.326	1636.043	209.961	1.782714
MAT-2069	Inconel 718	34.6948	1659.5	205.994	1.734422
MAT-2070	Inconel 718	36.4989	1646.45	200.5	1.728581
MAT-2071	Inconel 718	35.3768	1650.26	204.468	1.74241
MAT-2072	Inconel 718	35.4467	1684.31	202.942	1.719891
MAT-2073	Inconel 718	35.0429	1635.2	204.468	1.725965
MAT-2087	Inconel 718	36.9237	1633.29	200.989	1.757239
MAT-2088	Inconel 718	35.5764	1737.01	204.041	1.74493
MAT-2090	Inconel 718	35.3645	1691.1	205.444	1.758473
MAT-2430	TA-625 Fe	36.2496	1747.3	200.989	1.725158
MAT-2431	TA-625 Fe	34.6103	1740.53	206.421	1.737378
MAT-2432	TA-625 Fe	42.7678	1702.06	186.035	1.743763
MAT-2503	TA-625 Fe	38.878	1729.88	195.984	1.759245
MAT-2433	TA-625 Mo	36.9164	1712.94	194.031	1.637355

MAT-2434	TA-625 Mo	40.8044	1692.6	186.462	1.671355
MAT-2495	TA-625 Mo	34.4286	1707.65	195.007	1.542414
MAT-2480	TA-718 Fe	38.068	1688.12	190.002	1.61904
MAT-2483	TA-718 Fe	38.6545	1638.21	187.988	1.609316
MAT-2484	TA-718 Fe	38.9391	1665.95	197.998	1.79841
MAT-2487	TA-718 Fe	35.5018	1750.92	194.031	1.574613
MAT-2378	TA-718 Ni	37.3983	1770.43	190.979	1.606957
MAT-2381	TA-718 Ni	39.1497	1698.74	184.998	1.578497

Appendix D. Surface Tension Measurements of Inconel 625 during Parabolic Flights

Parabola #	Parabola Year	Temperature (K)	Surface Tension (N/m)
1	01_20200923_SCE_extended	1844.10	1.71
		1825.45	1.83
		1793.45	1.91
		1828.10	1.98
		1740.30	2.00
		1723.90	2.05
		1729.95	2.04
		1683.60	2.08
		1667.20	2.06
		1680.45	2.06
2	02_20200923_SCE_extended	1840.75	1.65
		1818.35	1.64
		1797.60	1.73
		1769.05	1.76
		1753.00	1.87
		1732.95	1.80
		1718.20	1.67
		1689.50	1.72
		1679.10	1.71
		1659.30	1.92
		1645.65	1.88
		1631.35	1.87
4	04_20200923_SCE_extended	1810.10	1.63
		1782.55	1.84
		1772.40	1.89
		1744.95	1.91

		1726.10	1.97
		1710.90	1.99
		1686.40	1.95
		1678.85	2.01
		1651.70	2.01
		1649.70	2.07
		1624.35	1.70
		1619.55	1.66
5	05_20200923_SCE_extended	1982.95	1.72
		1952.20	1.74
		1928.65	1.81
		1897.75	1.83
		1884.00	1.87
		1856.00	1.86
		1835.60	1.77
		1815.65	1.89
		1788.65	1.81
		1772.00	1.80
		1753.80	1.68
		1739.75	1.77
		1716.60	1.89
		1701.90	1.90
		1682.40	1.93
		1665.40	1.77
		1649.05	1.74
		1630.30	1.76
		1617.10	1.90
		1601.05	1.92
		1588.70	1.94
		1577.45	1.81

Appendix E. Surface Tension Measurements of Inconel 718 during Parabolic Flights

Parabola #	Parabola Year	Temperature (K)	Surface Tension (N/m)
11	11_20230912_SCE_extended	1850.20	1.60
		1826.90	1.70
		1807.05	1.73
		1785.60	1.77
		1769.55	1.76
		1753.70	1.80
		1726.85	1.79
		1715.70	1.81
		1687.70	1.75
		1672.90	1.74
		1656.85	1.72
		1636.90	1.72
		1625.35	1.71
		1606.95	1.64
		1594.25	1.69
		1582.40	1.69
		1568.90	1.67
		1554.80	1.66
13	13_20230912_SCE_extended	1891.45	1.73
		1865.00	1.73
		1843.00	1.71
		1820.10	1.75
		1801.15	1.76
		1778.05	1.74
		1755.50	1.74
		1739.75	1.75
		1717.80	1.75

		1704.60	1.66
		1687.95	1.69
		1667.40	1.71
		1654.95	1.73
		1634.80	1.74
		1619.60	1.80
		1607.55	1.79
		1587.45	1.73
		1577.35	1.72
		1565.90	1.71
		1550.45	1.75
		1544.60	1.67
		1528.05	1.68
14	14_20230912_SCE_extended	1825.75	1.53
		1804.25	1.61
		1783.65	1.64
		1757.75	1.82
		1741.30	1.74
		1720.40	1.75
		1699.35	1.80
		1687.20	1.76
		1663.00	1.69
		1648.30	1.71
		1633.75	1.72
		1615.50	1.74
		1602.45	1.81
		1585.95	1.74
		1570.40	1.67
		1558.75	1.69
		1543.30	1.67
		1529.65	1.80

		1518.30	1.67
		1502.20	1.67

Appendix F. TernaryAnalogs_PMV_Ideal_All

```
%  TernaryAnalogs_PMV_Ideal_All.m
%  ------------------------------------------------------------------------
%  PURPOSE:
%    Compute and export the temperature-dependent liquid densities (ρ_mix)
%    of four ternary analog alloys using the Partial-Molar-Volume (PMV)
%    model under IDEAL mixing (excess volume V^E = 0).
%
%  ALLOYS MODELED:
%    • TA-625Mo  : Cr–Ni–Mo   (Mo-containing analog of IN625)
%    • TA-625Fe  : Fe–Cr–Ni   (Fe-containing analog of IN625)
%    • TA-718Ni  : Fe–Cr–Ni   (Ni-rich analog of IN718)
%    • TA-718Fe  : Fe–Cr–Ni   (Fe-rich analog of IN718)
%
%  PMV MODEL FORM:
%      V_i(T)   = V0_i · [ 1 + a_i · ( T − T_ref,i ) ]
%      V_mix(T) = Σ x_i · V_i(T)                              (IDEAL: V^E = 0)
%      ρ_mix(T) = M_mix / V_mix(T)
%
%  NOTES:
%    • Pure-component V0_i (m^3/mol), a_i (1/K), and T_ref,i (K)
%    • No excess-volume / Redlich–Kister terms are applied in this file.
%    • Outputs a single Excel sheet {AllAlloys} with all alloys combined.
%    • Saves a PNG plot comparing all four ρ(T) curves.
%

clear; clc; close all;

%% ------------------------------ Controls --------------------------------
T = linspace(1500, 1900, 50)';   % Temperature grid [K], column vector for easy
table export
outFile = 'TernaryAnalogs_Density_PMV_Ideal.xlsx';
figFile = 'TernaryAnalogs_Density_PMV_Ideal.png';

%% ---------------------- Element properties --------------------
% Molar masses [kg/mol]
M.Fe = 55.845e-3;    % Iron
M.Cr = 52.000e-3;    % Chromium
M.Ni = 58.693e-3;    % Nickel
M.Mo = 95.950e-3;    % Molybdenum

% Pure liquid molar volumes in PMV model:
%   V_i(T) = V0_i * (1 + a_i * (T - Tref_i))
% Units: V0 [m^3/mol], a [1/K], Tref [K]
V0.Fe   = 7.94e-6;   a.Fe   = 1.30e-4;   Tref.Fe   = 1808;   % Fe
V0.Ni   = 7.43e-6;   a.Ni   = 1.51e-4;   Tref.Ni   = 1728;   % Ni
V0.Cr   = 8.27e-6;   a.Cr   = 1.10e-4;   Tref.Cr   = 2178;   % Cr
V0.Mo   = 10.30e-6;  a.Mo   = 0.53e-4;   Tref.Mo   = 2895;   % Mo

%% --------------------------- Alloy definitions -------------------------
% NOTE: Each composition row is normalized inside the loop.
% TA-625Mo: Ni 0.69, Cr 0.26, Mo 0.05 -> system Cr–Ni–Mo with [Cr Ni Mo]
% TA-625Fe: Ni 0.69, Cr 0.26, Fe 0.05 -> system Fe–Cr–Ni with [Fe Cr Ni]
% TA-718Ni: Ni 0.58, Cr 0.22, Fe 0.20 -> system Fe–Cr–Ni with [Fe Cr Ni]
% TA-718Fe: Ni 0.48, Cr 0.18, Fe 0.34 -> system Fe–Cr–Ni with [Fe Cr Ni]
alloys = struct( ...
  'name',   {'TA-625Mo (Cr-Ni-Mo)','TA-625Fe (Fe-Cr-Ni)','TA-718Ni (Fe-Cr-
Ni)','TA-718Fe (Fe-Cr-Ni)'}, ...
```

```
  'system', {'CrNiMo',              'FeCrNi',             'FeCrNi',
'FeCrNi'}, ...
  'x',      { [0.26 0.69 0.05],     [0.05 0.26 0.69],     [0.20 0.22 0.58],
[0.34 0.18 0.48] } ...
);

%% ----------------------------- Plot setup -----------------------------
figure('Color','w'); hold on; box on;
set(gca, 'FontSize', 12, 'LineWidth', 1.1);
title('Density of Ternary Analogs (PMV, Ideal Mixing)');
xlabel('Temperature (K)');
ylabel('\rho_{mix} (kg/m^3)');
colors = lines(numel(alloys));

%% ------------------------- Compute + combine table ----------------------
allTables = table();   % Will accumulate all four alloys here

for k = 1:numel(alloys)
    sys = alloys(k).system;      % 'FeCrNi' or 'CrNiMo'
    x   = alloys(k).x(:);        % composition row as column vector
    x   = x / sum(x);            % normalize to ensure sum(x)=1

    switch sys
        % ------------------------- Fe-Cr-Ni ternary ----------------------
        case 'FeCrNi'
            % Unpack mole fractions
            xFe = x(1); xCr = x(2); xNi = x(3);

            % Pure-component molar volumes over T
            VFe = V0.Fe .* (1 + a.Fe .* (T - Tref.Fe));
            VCr = V0.Cr .* (1 + a.Cr .* (T - Tref.Cr));
            VNi = V0.Ni .* (1 + a.Ni .* (T - Tref.Ni));

            % IDEAL mixture molar volume (no excess term)
            Vmix = xFe .* VFe + xCr .* VCr + xNi .* VNi;          % [m^3/mol]

            % Mixture molar mass (mole-fraction average)
            Mmix = xFe * M.Fe + xCr * M.Cr + xNi * M.Ni;          % [kg/mol]

        % ------------------------- Cr-Ni-Mo ternary ----------------------
        case 'CrNiMo'
            % Unpack mole fractions
            xCr = x(1); xNi = x(2); xMo = x(3);

            % Pure-component molar volumes over T
            VCr = V0.Cr .* (1 + a.Cr .* (T - Tref.Cr));
            VNi = V0.Ni .* (1 + a.Ni .* (T - Tref.Ni));
            VMo = V0.Mo .* (1 + a.Mo .* (T - Tref.Mo));

            % IDEAL mixture molar volume (no excess term)
            Vmix = xCr .* VCr + xNi .* VNi + xMo .* VMo;          % [m^3/mol]

            % Mixture molar mass (mole-fraction average)
            Mmix = xCr * M.Cr + xNi * M.Ni + xMo * M.Mo;          % [kg/mol]
    end

    % ------------------------ Density over temperature ------------------
    % ρ_mix(T) = M_mix / V_mix(T)
    rho = Mmix ./ Vmix;   % [kg/m^3], vector over T
```

```
    % ------------------------------ Plotting -----------------------------
    plot(T, rho, 'LineWidth', 1.6, 'Color', colors(k,:), 'DisplayName',
alloys(k).name);

    % --------------------------- Append to table -------------------------
    AlloyName = repmat(string(alloys(k).name), numel(T), 1);
    Ti = table(AlloyName, T, rho, ...
        'VariableNames', {'Alloy','Temperature_K','Density_kgm3'});
    allTables = [allTables; Ti]; %#ok<AGROW>
end

legend('Location', 'best'); grid on;

%% ------------------------------ Export ---------------------------------
% Write a SINGLE combined sheet with all alloys
if exist(outFile, 'file'), delete(outFile); end
writetable(allTables, outFile, 'Sheet', 'AllAlloys');

% Save a high-resolution PNG of the figure
print(gcf, figFile, '-dpng', '-r300');

% Console summary
fprintf('☑ Exported one-sheet file: %s\n', outFile);
fprintf('🖼  Saved plot: %s\n', figFile);

%% ------------------------------ END ------------------------------------
```

Appendix G. FeCrNi_PMV_Export

```
%% ================================================================

%  FeCrNi_PMV_Export.m
%  Density of Fe-Cr-Ni alloys via PMV with binary excess volumes.
%  Uses Table 3 (pure V_i(T)) and Table 2 (V^{ij} in cm^3/mol).
%  ================================================================
clear; clc; close all;

%% Temperature grid
T = linspace(1500,1900,50)';   % K

%% Compositions [Fe Cr Ni]
compositions = [
    0.05  0.26  0.69;   % TA-625Fe
    0.20  0.22  0.58;   % TA-718Ni
    0.34  0.18  0.48;   % TA-718Fe
];
labels = { 'TA 625-Fe', 'TA-718Ni', 'TA 718-Fe' };
compositions = compositions ./ sum(compositions,2);

%% Molar masses (kg/mol)
MFe = 55.845e-3; MCr = 52.000e-3; MNi = 58.693e-3;

%% Pure liquid molar volumes V_i(T)
VFe0 = 7.94e-6;  aFe = 1.30e-4;  TrefFe = 1808;  % m^3/mol, 1/K, K
VNi0 = 7.43e-6;  aNi = 1.51e-4;  TrefNi = 1728;
VCr0 = 8.27e-6;  aCr = 1.10e-4;  TrefCr = 2178;

%% Binary excess volume parameters V^{ij} (m^3/mol)
V_FeCr = 0.28e-6;   % Cr-Fe  (0.28 cm^3/mol)
V_FeNi = 0.51e-6;   % Fe-Ni  (0.51 cm^3/mol)
V_CrNi = 0.74e-6;   % Cr-Ni  (0.74 cm^3/mol)

%% Vectorized helper
compute_rho = @(Tvec,xFe,xCr,xNi) pmv_FeCrNi(Tvec,xFe,xCr,xNi, ...
    MFe,MCr,MNi, VFe0,VCr0,VNi0, aFe,aCr,aNi, TrefFe,TrefCr,TrefNi, ...
    V_FeCr,V_FeNi,V_CrNi);

%% Plot + export
f = figure('Color','w'); hold on; box on;
set(gca,'FontSize',12,'LineWidth',1.1);
title('Density of Fe-Cr-Ni Alloys (PMV with V^E)'); xlabel('T (K)'); ylabel('\rho
(kg/m^3)');
colors = lines(size(compositions,1));

outFile = 'FeCrNi_Density_PMV.xlsx'; if exist(outFile,'file'), delete(outFile);
end
allTables = table();

for i = 1:size(compositions,1)
    xFe = compositions(i,1); xCr = compositions(i,2); xNi = compositions(i,3);
    rho = compute_rho(T, xFe, xCr, xNi);

    plot(T, rho, 'LineWidth',1.6, 'Color', colors(i,:), 'DisplayName', labels{i});

    AlloyName = repmat(string(labels{i}), numel(T), 1);
```

```
    Ti = table(AlloyName, T, rho, 'VariableNames',
{'Alloy','Temperature_K','Density_kgm3'});
    writetable(Ti, outFile, 'Sheet', sprintf('Alloy_%d',i));
    allTables = [allTables; Ti]; %#ok<AGROW>
end

legend('Location','best'); grid on;
writetable(allTables, outFile, 'Sheet', 'AllAlloys');
print(f,'FeCrNi_Density_PMV.png','-dpng','-r300');
fprintf('☑ Exported %s and FeCrNi_Density_PMV.png\n', outFile);

%% ---------- Local function ----------
function rho = pmv_FeCrNi(T,xFe,xCr,xNi, MFe,MCr,MNi, VFe0,VCr0,VNi0, aFe,aCr,aNi,
TFe,TCr,TNi, VFeCr,VFeNi,VCrNi)
    T = T(:);
    VFe = VFe0*(1 + aFe*(T - TFe));
    VCr = VCr0*(1 + aCr*(T - TCr));
    VNi = VNi0*(1 + aNi*(T - TNi));

    Videal = xFe*VFe + xCr*VCr + xNi*VNi;
    Vex    = xFe*xCr*VFeCr + xFe*xNi*VFeNi + xCr*xNi*VCrNi;   % scalar
    Vmix   = Videal + Vex;

    Mmix = xFe*MFe + xCr*MCr + xNi*MNi;
    rho  = Mmix ./ Vmix;
end
```

```
% Fe–Cr–Ni Ternary Surface Tension for Specific Alloys over Temperature Range

% Butler-style model with γ_i(T), w_i(T), binary Redlich–Kister (L0/L1).
% Alloys (no Mo): TA-625Fe, TA-718Ni, TA-718Fe
% Outputs:
%   • Console tables
%   • Scatter plot (γ vs T) — no lines
%   • Excel file with γ(T) and surface compositions (xsFe, xsCr, xsNi)

clc; clear;

%% ===== Controls =====
T_list = 1500:50:1900;        % K
beta   = 0.83;                % surface/bulk scaling
lamb   = 0.5;                 % surface excess scaling
epsx   = 1e-8;                % small guard for logs
xlsx_out = 'FeCrNi_Butler_Tsweep.xlsx';

%% ===== Constants =====
R  = 8.314;                   % J/mol/K
Na = 6.02214076e23;           % 1/mol

%% ===== Pure-element parameters (from tables) =====
%  TL (K), gamma_L (N/m), dgamma_dT (N/(m·K)), Vm_L (m^3/mol), alpha (1/K)
Fe.TL = 1808;  Fe.gamma_L = 1.872; Fe.dgamma_dT = -0.49e-3; Fe.Vm_L = 7.94e-6;
Fe.alpha = 1.30e-4;
Cr.TL = 2178;  Cr.gamma_L = 1.700; Cr.dgamma_dT = -0.32e-3; Cr.Vm_L = 8.27e-6;
Cr.alpha = 1.10e-4;
Ni.TL = 1728;  Ni.gamma_L = 1.778; Ni.dgamma_dT = -0.38e-3; Ni.Vm_L = 7.43e-6;
Ni.alpha = 1.51e-4;

gamma_of_T = @(q,Tin) q.gamma_L + q.dgamma_dT*(Tin - q.TL);
Vm_of_T    = @(q,Tin) q.Vm_L * (1 + q.alpha*(Tin - q.TL));
w_of_T     = @(q,Tin) 1.091 * Na^(1/3) * (Vm_of_T(q,Tin)).^(2/3);   % molar
surface area

%% ===== Custom compositions (atomic fraction) =====
% Table 2 (Batch 5) — excluding TA-625Mo (has Mo)
alloys = {
    'TA-625Fe', struct('xNi',0.69,'xCr',0.26,'xFe',0.05)
    'TA-718Ni', struct('xNi',0.58,'xCr',0.22,'xFe',0.20)
    'TA-718Fe', struct('xNi',0.48,'xCr',0.18,'xFe',0.34)
};
n = numel(alloys(:,1));

%% ===== Solver options =====
options = optimoptions('lsqnonlin','Display','off', ...
    'FunctionTolerance',1e-14,'OptimalityTolerance',1e-14,'StepTolerance',1e-14,
...
    'MaxFunctionEvaluations', 3e4, 'MaxIterations', 2e3);

%% ===== Preallocate (rows = alloys, cols = temperatures) =====
nT = numel(T_list);
gammaMatrix = nan(n, nT);
xsFeMat     = nan(n, nT);
xsCrMat     = nan(n, nT);
xsNiMat     = nan(n, nT);
```

```
%% ===== Main loop over temperature and alloys =====
for j = 1:nT
    T = T_list(j);

    % --- Temperature-dependent pure-element values
    yFe = gamma_of_T(Fe,T);  wFe = w_of_T(Fe,T);
    yCr = gamma_of_T(Cr,T);  wCr = w_of_T(Cr,T);
    yNi = gamma_of_T(Ni,T);  wNi = w_of_T(Ni,T);

    % --- Interaction parameters (Table 4 → L0/L1), J/mol
    % Form: x_A x_B [A x_A + B x_B]  ↔  x_A x_B [L0 + L1(x_A − x_B)]
    % L0 = (A+B)/2, L1 = (A−B)/2
    A_FeNi = (-8368 + 2.727*T);      B_FeNi = (-32217 + 9.205*T);
    A_FeCr = ( 20794 -10.46*T);      B_FeCr = ( 20794 -10.46*T);
    A_NiCr = (-8368);                B_NiCr = (-8368);

    LFeNi0 = 0.5*(A_FeNi + B_FeNi);  LFeNi1 = 0.5*(A_FeNi - B_FeNi);
    LFeCr0 = 0.5*(A_FeCr + B_FeCr);  LFeCr1 = 0.5*(A_FeCr - B_FeCr);  % = 0 here
    LNiCr0 = 0.5*(A_NiCr + B_NiCr);  LNiCr1 = 0.5*(A_NiCr - B_NiCr);  % = -8368, 0

    for iAlloy = 1:n
        comp = alloys{iAlloy,2};
        xFe = comp.xFe; xCr = comp.xCr; xNi = comp.xNi;
        s = xFe + xCr + xNi; xFe=xFe/s; xCr=xCr/s; xNi=xNi/s; % renormalize

        % Initial guess (surface comps near bulk; gamma weighted by pure γ)
        gamma_guess = yFe*xFe + yCr*xCr + yNi*xNi;
        guess = [max(xFe,1e-4), max(xCr,1e-4), gamma_guess];
        lb=[0,0,0.3]; ub=[1,1,3.0]; dx=1e-5;

        fun = @(pp) errorFunction(pp, xFe, xCr, xNi, dx, R, T, ...
            wFe, wCr, wNi, yFe, yCr, yNi, beta, lamb, ...
            LFeCr0, LFeCr1, LFeNi0, LFeNi1, LNiCr0, LNiCr1, epsx);

        sol = lsqnonlin(fun, guess, lb, ub, options);

        xsFe = sol(1); xsCr = sol(2); xsNi = 1 - xsFe - xsCr;
        gamma = sol(3);

        xsFeMat(iAlloy,j) = xsFe;
        xsCrMat(iAlloy,j) = xsCr;
        xsNiMat(iAlloy,j) = xsNi;
        gammaMatrix(iAlloy,j) = gamma;
    end
end

%% ===== Console tables =====
RowNames = string(alloys(:,1));
disp("Gamma (N/m) by Alloy and Temperature:");
GammaTable = array2table(gammaMatrix, ...
    'VariableNames', compose("T_%dK", T_list), ...
    'RowNames', RowNames);
disp(GammaTable);

disp("Surface fractions x_S^{Fe}:");
disp(array2table(xsFeMat,'VariableNames',compose("T_%dK",T_list),'RowNames',RowNam
es));
disp("Surface fractions x_S^{Cr}:");
```

```
disp(array2table(xsCrMat,'VariableNames',compose("T_%dK",T_list),'RowNames',RowNam
es));
disp("Surface fractions x_S^{Ni}:");
disp(array2table(xsNiMat,'VariableNames',compose("T_%dK",T_list),'RowNames',RowNam
es));

%% ===== Scatter plot (γ vs Temperature) — NO LINES =====
figure('Position',[120,120,840,480]); hold on;
for iAlloy = 1:n
    scatter(T_list, gammaMatrix(iAlloy,:), 60, 'filled', 'DisplayName',
alloys{iAlloy,1});
end
xlabel('Temperature (K)');
ylabel('Surface Tension (N/m)');
title('Surface Tension vs Temperature (Fe-Cr-Ni, Butler Model)');
legend('Location','best'); grid on;

%% ===== Export to Excel =====
% Sheet 1: Gamma
GammaTblOut = cell2table([cellstr(RowNames) num2cell(gammaMatrix)], ...
    'VariableNames', ['Alloy', compose("T_%dK",T_list)]);
writetable(GammaTblOut, xlsx_out, 'Sheet', 'Gamma', 'WriteMode',
'overwritesheet');

% Sheet 2-4: Surface compositions
writetable(cell2table([cellstr(RowNames) num2cell(xsFeMat)], ...
    'VariableNames', ['Alloy', compose("T_%dK",T_list)]), xlsx_out, 'Sheet',
'xsFe', 'WriteMode','overwritesheet');
writetable(cell2table([cellstr(RowNames) num2cell(xsCrMat)], ...
    'VariableNames', ['Alloy', compose("T_%dK",T_list)]), xlsx_out, 'Sheet',
'xsCr', 'WriteMode','overwritesheet');
writetable(cell2table([cellstr(RowNames) num2cell(xsNiMat)], ...
    'VariableNames', ['Alloy', compose("T_%dK",T_list)]), xlsx_out, 'Sheet',
'xsNi', 'WriteMode','overwritesheet');

fprintf('Saved results to %s\n', xlsx_out);

%% ===== Model residual function =====
function err = errorFunction(p,xFe,xCr,xNi,dx,R,T,wFe,wCr,wNi,yFe,yCr,yNi, ...
    beta,lamb,LFeCr0,LFeCr1,LFeNi0,LFeNi1,LNiCr0,LNiCr1,epsx)

    xsFe = p(1); xsCr = p(2); gamma = p(3);
    xsNi = 1 - xsFe - xsCr;

    % guard against invalid values before logs
    if any([xsFe, xsCr, xsNi, xFe, xCr, xNi] <= epsx) || any([xsFe, xsCr, xsNi] >=
1-epsx)
        err = [1e6, 1e6, 1e6]; return;
    end

    % binary RK (no ternary term)
    GE = @(xF,xC,xN) ...
        xF.*xC.*(LFeCr0 + LFeCr1*(xF - xC)) + ...   % Fe-Cr
        xF.*xN.*(LFeNi0 + LFeNi1*(xF - xN)) + ...   % Fe-Ni
        xC.*xN.*(LNiCr0 + LNiCr1*(xC - xN)) + ...   % Ni-Cr
        xF.*xC.*xN.*(0);

    GEs = @(a,b,c) lamb * GE(a,b,c);
```

```
    % finite-difference partials
    dGE  = @(f,a,b,c)(f(a+dx,b,c)-f(a,b,c))/dx;
    dGEb = @(f,a,b,c)(f(a,b+dx,c)-f(a,b,c))/dx;
    dGEc = @(f,a,b,c)(f(a,b,c+dx)-f(a,b,c))/dx;

    % Bulk derivatives
    dX  = dGE (GE, xFe, xCr, xNi);
    dXC = dGEb(GE, xFe, xCr, xNi);
    dXN = dGEc(GE, xFe, xCr, xNi);

    % Surface derivatives
    dXS  = dGE (GEs, xsFe, xsCr, xsNi);
    dXSC = dGEb(GEs, xsFe, xsCr, xsNi);
    dXSN = dGEc(GEs, xsFe, xsCr, xsNi);

    % Bulk partial molar Gibbs
    gibbsBFe = GE(xFe,xCr,xNi) + (1 - xFe)*dX - xCr*dXC - xNi*dXN;
    gibbsBCr = GE(xFe,xCr,xNi) - xFe*dX + (1 - xCr)*dXC - xNi*dXN;
    gibbsBNi = GE(xFe,xCr,xNi) - xFe*dX - xCr*dXC + (1 - xNi)*dXN;

    % Surface partial molar Gibbs
    gibbsSFe = beta*( GEs(xsFe,xsCr,xsNi) + (1 - xsFe)*dXS - xsCr*dXSC - xsNi*dXSN
);
    gibbsSCr = beta*( GEs(xsFe,xsCr,xsNi) - xsFe*dXS + (1 - xsCr)*dXSC - xsNi*dXSN
);
    gibbsSNi = beta*( GEs(xsFe,xsCr,xsNi) - xsFe*dXS - xsCr*dXSC + (1 - xsNi)*dXSN
);

    % Residuals for γ-equality of all three components
    err(1) = yNi + R*T/wNi * log(xsNi/xNi) + (gibbsSNi - gibbsBNi)/wNi - gamma;
    err(2) = yCr + R*T/wCr * log(xsCr/xCr) + (gibbsSCr - gibbsBCr)/wCr - gamma;
    err(3) = yFe + R*T/wFe * log(xsFe/xFe) + (gibbsSFe - gibbsBFe)/wFe - gamma;
end
```

Appendix I. Butler_Mo_Cr_Ni_TernaryAnalogs_Range_Of_Temp_Final

```
% Ni–Cr–Mo Ternary Surface Tension for Specific Alloys over Temperature Range

% Butler-style model with γ_i(T), w_i(T), binary Redlich–Kister (L0/L1).
% Alloys (with Mo): TA-625Mo
% Outputs:
%   • Console tables
%   • Scatter plot (γ vs T) — no lines
%   • Excel file with γ(T) and surface compositions (xsNi, xsCr, xsMo)

clc; clear;

%% ===== Controls =====
T_list  = 1500:50:1900;       % K
beta    = 0.83;               % surface/bulk scaling
lamb    = 0.5;                % surface excess scaling
epsx    = 1e-8;               % small guard for logs
xlsx_out = 'NiCrMo_Butler_Tsweep.xlsx';

%% ===== Constants =====
R  = 8.314;                   % J/mol/K
Na = 6.02214076e23;           % 1/mol

%% ===== Pure-element parameters (from tables) =====
%  TL (K), gamma_L (N/m), dgamma_dT (N/(m·K)), Vm_L (m^3/mol), alpha (1/K)
Ni.TL = 1728;  Ni.gamma_L = 1.778; Ni.dgamma_dT = -0.38e-3; Ni.Vm_L = 7.43e-6;
Ni.alpha = 1.51e-4;
Cr.TL = 2178;  Cr.gamma_L = 1.700; Cr.dgamma_dT = -0.32e-3; Cr.Vm_L = 8.27e-6;
Cr.alpha = 1.10e-4;
Mo.TL = 2895;  Mo.gamma_L = 2.250; Mo.dgamma_dT = -0.30e-3; Mo.Vm_L = 10.30e-6;
Mo.alpha = 1.53e-4;

gamma_of_T = @(q,Tin) q.gamma_L + q.dgamma_dT*(Tin - q.TL);
Vm_of_T    = @(q,Tin) q.Vm_L * (1 + q.alpha*(Tin - q.TL));
w_of_T     = @(q,Tin) 1.091 * Na^(1/3) * (Vm_of_T(q,Tin)).^(2/3);   % molar
surface area

%% ===== Custom compositions (atomic fraction) =====
% Add more Ni–Cr–Mo alloys as rows if needed.
alloys = {
    'TA-625Mo', struct('xNi',0.69,'xCr',0.26,'xMo',0.05)
};
n = numel(alloys(:,1));

%% ===== Solver options =====
options = optimoptions('lsqnonlin','Display','off', ...
    'FunctionTolerance',1e-14,'OptimalityTolerance',1e-14,'StepTolerance',1e-14,
...
    'MaxFunctionEvaluations', 3e4, 'MaxIterations', 2e3);

%% ===== Preallocate (rows = alloys, cols = temperatures) =====
nT = numel(T_list);
gammaMatrix = nan(n, nT);
xsNiMat     = nan(n, nT);
xsCrMat     = nan(n, nT);
xsMoMat     = nan(n, nT);

%% ===== Main loop over temperature and alloys =====
```

```
for j = 1:nT
    T = T_list(j);

    % --- Temperature-dependent pure-element values
    yNi = gamma_of_T(Ni,T);  wNi = w_of_T(Ni,T);
    yCr = gamma_of_T(Cr,T);  wCr = w_of_T(Cr,T);
    yMo = gamma_of_T(Mo,T);  wMo = w_of_T(Mo,T);

    % --- Interaction parameters (Table 4 → L0/L1), J/mol
    % Form: x_A x_B [A x_A + B x_B]  ↔  x_A x_B [L0 + L1(x_A − x_B)]
    % L0 = (A+B)/2, L1 = (A−B)/2

    % Ni–Cr
    A_NiCr = (-8368);                 B_NiCr = (-8368);
    LNiCr0 = 0.5*(A_NiCr + B_NiCr);   LNiCr1 = 0.5*(A_NiCr - B_NiCr);   % = -8368,
0

    % Cr–Mo
    A_CrMo = (25522 + 11.30*T);       B_CrMo = (12552 + 5.86*T);
    LCrMo0 = 0.5*(A_CrMo + B_CrMo);   LCrMo1 = 0.5*(A_CrMo - B_CrMo);

    % Ni–Mo
    A_NiMo = (-17573 - 13.807*T);     B_NiMo = (-17573 - 13.807*T);
    LNiMo0 = 0.5*(A_NiMo + B_NiMo);   LNiMo1 = 0.5*(A_NiMo - B_NiMo);   % = same,
0

    for iAlloy = 1:n
        comp = alloys{iAlloy,2};
        xNi = comp.xNi; xCr = comp.xCr; xMo = comp.xMo;
        s = xNi + xCr + xMo; xNi=xNi/s; xCr=xCr/s; xMo=xMo/s; % renormalize

        % Initial guess (surface comps near bulk; gamma weighted by pure γ)
        gamma_guess = yNi*xNi + yCr*xCr + yMo*xMo;
        guess = [max(xNi,1e-4), max(xCr,1e-4), gamma_guess];
        lb=[0,0,0.3]; ub=[1,1,3.0]; dx=1e-5;

        fun = @(pp) errorFunction(pp, xNi, xCr, xMo, dx, R, T, ...
            wNi, wCr, wMo, yNi, yCr, yMo, beta, lamb, ...
            LCrMo0, LCrMo1, LNiMo0, LNiMo1, LNiCr0, LNiCr1, epsx);

        sol = lsqnonlin(fun, guess, lb, ub, options);

        xsNi = sol(1); xsCr = sol(2); xsMo = 1 - xsNi - xsCr;
        gamma = sol(3);

        xsNiMat(iAlloy,j) = xsNi;
        xsCrMat(iAlloy,j) = xsCr;
        xsMoMat(iAlloy,j) = xsMo;
        gammaMatrix(iAlloy,j) = gamma;
    end
end

%% ===== Console tables =====
RowNames = string(alloys(:,1));
disp("Gamma (N/m) by Alloy and Temperature:");
GammaTable = array2table(gammaMatrix, ...
    'VariableNames', compose("T_%dK", T_list), ...
    'RowNames', RowNames);
disp(GammaTable);
```

```
disp("Surface fractions x_S^{Ni}:");
disp(array2table(xsNiMat,'VariableNames',compose("T_%dK",T_list),'RowNames',RowNam
es));
disp("Surface fractions x_S^{Cr}:");
disp(array2table(xsCrMat,'VariableNames',compose("T_%dK",T_list),'RowNames',RowNam
es));
disp("Surface fractions x_S^{Mo}:");
disp(array2table(xsMoMat,'VariableNames',compose("T_%dK",T_list),'RowNames',RowNam
es));

%% ===== Scatter plot (γ vs Temperature) — NO LINES =====
figure('Position',[120,120,840,480]); hold on;
for iAlloy = 1:n
    scatter(T_list, gammaMatrix(iAlloy,:), 60, 'filled', 'DisplayName',
alloys{iAlloy,1});
end
xlabel('Temperature (K)');
ylabel('Surface Tension (N/m)');
title('Surface Tension vs Temperature (Ni–Cr–Mo, Butler Model)');
legend('Location','best'); grid on;

%% ===== Export to Excel =====
% Sheet 1: Gamma
GammaTblOut = cell2table([cellstr(RowNames) num2cell(gammaMatrix)], ...
    'VariableNames', ['Alloy', compose("T_%dK",T_list)]);
writetable(GammaTblOut, xlsx_out, 'Sheet', 'Gamma', 'WriteMode',
'overwritesheet');

% Sheet 2–4: Surface compositions
writetable(cell2table([cellstr(RowNames) num2cell(xsNiMat)], ...
    'VariableNames', ['Alloy', compose("T_%dK",T_list)]), xlsx_out, 'Sheet',
'xsNi', 'WriteMode','overwritesheet');
writetable(cell2table([cellstr(RowNames) num2cell(xsCrMat)], ...
    'VariableNames', ['Alloy', compose("T_%dK",T_list)]), xlsx_out, 'Sheet',
'xsCr', 'WriteMode','overwritesheet');
writetable(cell2table([cellstr(RowNames) num2cell(xsMoMat)], ...
    'VariableNames', ['Alloy', compose("T_%dK",T_list)]), xlsx_out, 'Sheet',
'xsMo', 'WriteMode','overwritesheet');

fprintf('Saved results to %s\n', xlsx_out);

%% ===== Model residual function =====
function err = errorFunction(p,xNi,xCr,xMo,dx,R,T,wNi,wCr,wMo,yNi,yCr,yMo, ...
    beta,lamb,LCrMo0,LCrMo1,LNiMo0,LNiMo1,LNiCr0,LNiCr1,epsx)

    xsNi = p(1); xsCr = p(2); gamma = p(3);
    xsMo = 1 - xsNi - xsCr;

    % guard against invalid values before logs
    if any([xsNi, xsCr, xsMo, xNi, xCr, xMo] <= epsx) || any([xsNi, xsCr, xsMo] >=
1-epsx)
        err = [1e6, 1e6, 1e6]; return;
    end

    % binary RK (no ternary term)
    GE = @(xN,xC,xM) ...
        (xN.*xC).*(LNiCr0 + LNiCr1*(xN - xC)) + ...   % Ni–Cr
        (xC.*xM).*(LCrMo0 + LCrMo1*(xC - xM)) + ...   % Cr–Mo
```

```
        (xN.*xM).*(LNiMo0 + LNiMo1*(xN - xM)) + ...   % Ni–Mo
        (xN.*xC.*xM).*0;

    GEs = @(a,b,c) lamb * GE(a,b,c);

    % finite-difference partials (order: Ni, Cr, Mo)
    dGE_N  = @(f,a,b,c)(f(a+dx,b,c)-f(a,b,c))/dx;
    dGE_C  = @(f,a,b,c)(f(a,b+dx,c)-f(a,b,c))/dx;
    dGE_M  = @(f,a,b,c)(f(a,b,c+dx)-f(a,b,c))/dx;

    % Bulk derivatives
    dN  = dGE_N(GE, xNi, xCr, xMo);
    dC  = dGE_C(GE, xNi, xCr, xMo);
    dM  = dGE_M(GE, xNi, xCr, xMo);

    % Surface derivatives
    dNS = dGE_N(GEs, xsNi, xsCr, xsMo);
    dCS = dGE_C(GEs, xsNi, xsCr, xsMo);
    dMS = dGE_M(GEs, xsNi, xsCr, xsMo);

    % Bulk partial molar Gibbs
    gibbsBNi = GE(xNi,xCr,xMo) + (1 - xNi)*dN - xCr*dC - xMo*dM;
    gibbsBCr = GE(xNi,xCr,xMo) - xNi*dN + (1 - xCr)*dC - xMo*dM;
    gibbsBMo = GE(xNi,xCr,xMo) - xNi*dN - xCr*dC + (1 - xMo)*dM;

    % Surface partial molar Gibbs
    gibbsSNi = beta*( GEs(xsNi,xsCr,xsMo) + (1 - xsNi)*dNS - xsCr*dCS - xsMo*dMS
);
    gibbsSCr = beta*( GEs(xsNi,xsCr,xsMo) - xsNi*dNS + (1 - xsCr)*dCS - xsMo*dMS
);
    gibbsSMo = beta*( GEs(xsNi,xsCr,xsMo) - xsNi*dNS - xsCr*dCS + (1 - xsMo)*dMS
);

    % Residuals for γ-equality of all three components
    err(1) = yNi + R*T/wNi * log(xsNi/xNi) + (gibbsSNi - gibbsBNi)/wNi - gamma;
    err(2) = yCr + R*T/wCr * log(xsCr/xCr) + (gibbsSCr - gibbsBCr)/wCr - gamma;
    err(3) = yMo + R*T/wMo * log(xsMo/xMo) + (gibbsSMo - gibbsBMo)/wMo - gamma;
end
```

Appendix K. Chemical Composition Certification – Ni–Cr–Fe Alloy Samples

Luvak Inc.
722 Main Street
Boylston, MA 01505
Phone 508-869-6401

Analytical report no.
L-4157
Page 1 of 2
www.luvak.com

Requested by:
Tufts University
Dept. of Mechanical Engineering
204 Anderson Hall
Medford, MA 02155

Attention:
Douglas Matson
douglas.matson@tufts.edu

Invoice number: 105966
Customer Purchase Order No: Credit Card

Date received: 05/23/25
Report date: 06/16/25
Invoice date: 06/16/25

Description: Two Ni-Cr-Fe Alloy samples were analyzed as listed below.

Results:

Sample Identification	MAT-2351 TA718Ni	MAT-2378 TA718-Ni	Precision
	Wt %	Wt %	+/- Wt %
Chromium	18.4	17.6	+/- 0.4%
Iron	20.2	19.8	+/- 0.4%
Nickel	61.4	62.6	+/- 1.3%
Scan	-----	-----	-----

Method: Indirect current plasma emission spectroscopy – ASTM E 1479-16

No other elements over 0.05% detected

Luvak Inc. utilizes the ASTM E29 rounding method unless specification or customer designates otherwise.

Luvak Inc.

By Derek Langlois
Derek Langlois
Quality Manager

Luvak Inc.
722 Main Street
Boylston, MA 01505
Phone 508-869-6401

Requested by:
Tufts University
Dept. of Mechanical Engineering
204 Anderson Hall
Medford, MA 02155

Attention:
Douglas Matson
douglas.matson@tufts.edu

Invoice number: 105966
Customer Purchase Order No: Credit Card

Date received: 05/23/25
Report date: 06/16/25
Invoice date: 06/16/25

Description: Two Ni-Cr-Fe Alloy samples were analyzed as listed below.

Results:

Sample Identification	MAT-2353 TA625 Fe	MAT-2379 TA625 Fe	MAT-2380 TA625-Fe mix Ni	Precision
	Wt %	Wt %	Wt %	+/- Wt %
Chromium	22.0	22.6	20.3	+/- 0.5%
Iron	5.13	4.93	4.91	+/- 0.1%
Nickel	72.9	72.5	74.8	+/- 1.5%
Scan	-----	-----	-----	-----

Method: Indirect current plasma emission spectroscopy – ASTM E 1479-16

No other elements over 0.05% detected

Luvak Inc. utilizes the ASTM E29 rounding method unless specification or customer designates otherwise.

Luvak Inc.

By Derek Langlois
Derek Langlois
Quality Manager

Appendix L. Surface, Bulk, and Wet-Chemistry Composition Analyses

Sample Properties During Fabrication

Sample ID	Elements Added (wt%)	Initial Ni Conc (wt%)	Initial Cr Conc (wt%)	Initial Fe Conc (wt%)	Total Mass Before Arc Melting (mg)	Total Mass After Arc Melting (mg)	Total Mass After Processing (mg)
MAT-2351	TA-718-Ni	58.0	21.8	20.2	38.2797	38.2031	37.0152
MAT-2378	TA-718-Ni	58.0	21.8	20.2	37.4452	37.3983	35.6982
MAT-2379	TA-625-Fe	69.3	26.1	4.6	40.9722	40.910	39.750
MAT-2380	TA-625-Fe	69.3	26.1	4.6	40.3846	40.2381	37.3706
MAT-2353	TA-625-Fe	69.3	26.1	4.6	40.8966	40.8336	39.6589

Surface analysis — XPS Xray Photoelectron Spectroscopy
ESCA Electron Spectroscopy for Chemical Analysis

Sample ID	Elements Added (wt%)	XPS Final Ni Conc (wt%)	XPS Final Cr Conc (wt%)	XPS Final Fe Conc (wt%)
MAT-2351	TA-718-Ni	58.10	20.38	21.52
MAT-2378	TA-718-Ni	63.63	17.14	19.23
MAT-2379	TA-625-Fe	78.44	18.27	3.29
MAT-2380	TA-625-Fe	77.13	16.87	4.16
MAT-2353	TA-625-Fe	70.94	23.66	5.50

Bulk analysis		EDS - Energy Dispersive X-ray Spectroscopy				(uses SEM)	
Alloy	File	Average			StDev		
		Cr	**Fe**	**Ni**	**Cr**	**Fe**	**Ni**
TA718-Ni	MAT-2351_Specta	15.79	21.53	62.68	1.40	0.28	1.24
TA718-Ni	MAT-2351_Specta_At	18.76	21.17	60.08	8.23	1.03	7.23
TA718-Ni	MAT-2378_Specta	13.60	20.86	65.55	0.20	0.22	0.35
TA718-Ni	MAT-2378_Specta_At	14.93	21.32	63.74	0.21	0.22	0.36
TA625-Fe	MAT-2379_Specta	20.06	5.10	74.84	0.31	0.22	0.51
TA625-Fe	MAT-2379_Specta_At	22.03	5.21	72.76	0.33	0.22	0.53
TA625-Fe	MAT-2380_Specta	17.35	5.27	77.37	1.69	0.19	1.65
TA625-Fe	MAT-2380_Specta_At	19.11	5.41	75.48	1.82	0.20	1.77
TA625-Fe	MAT-2353_Specta	18.95	5.28	75.78	0.67	0.26	0.89
TA625-Fe	MAT-2353_Specta_At	20.83	5.40	73.77	0.72	0.27	0.94
Composition		Cr (wt%)	Fe(wt%)	Ni (wt%)			
TA718-Ni	MAT-2351_Specta	15.79 ± 1.40	21.53 ± 0.28	62.68 ± 1.24			
TA718-Ni	MAT-2378_Specta	13.60 ± 0.20	20.86 ± 0.22	65.55 ± 0.35			
TA625-Fe	MAT-2379_Specta	20.06 ± 0.31	5.10 ± 0.22	74.84 ± 0.51			
TA625-Fe	MAT-2380_Specta	17.35 ± 1.69	5.27 ± 0.19	77.37 ± 1.65			
TA625-Fe	MAT-2353_Specta	18.95 ± 0.67	5.28 ± 0.26	75.78 ± 0.89			

Wet Chemistry	DCPES - Direct Current Plasma Emission Spectroscopy	Luvak	ASTM E 1097-12				
Sample ID	**Elements Added (wt%)**	**DCPES Final Ni Conc (wt%)**	**error**	**DCPES Final Cr Conc (wt%)**	**error**	**DCPES Final Fe Conc (wt%)**	**error**
MAT-2351	TA-718-Ni	61.4	1.3	18.4	0.4	20.2	0.4
MAT-2378	TA-718-Ni	62.6	1.3	17.6	0.4	19.8	0.4
MAT-2379	TA-625-Fe	72.5	1.50	22.6	0.5	4.93	0.1
MAT-2380	TA-625-Fe	74.8	1.50	20.3	0.5	4.91	0.1
MAT-2353	TA-625-Fe	72.9	1.50	22	0.5	5.13	0.1

Appendix M. Xps Surface Analysis of Five Electro-Statically Levitated Inconel 718 And Inconel 625 Samples

Five, nearly two-millimeter diameter electrostatically levitated samples were provided to EM31 for surface chemical analysis. Two of these were IN-718 and three were IN-625 alloy samples. The samples were analyzed in a Kratos Ultra DLD spectrometer. Samples were mounted on to a sample bar with soft Indium metal sheet on top, The Indium metal had hemispherical impressions with a double-sided black tape covering them. Samples were pushed into these hemispherical dips for proper electrical conductivity and physical security with very little applied pressure to not to damage sample surface at the same time securing the sample to the bar.

Appearance of samples after they were mounted are shown in Figs. 1 through 5. The

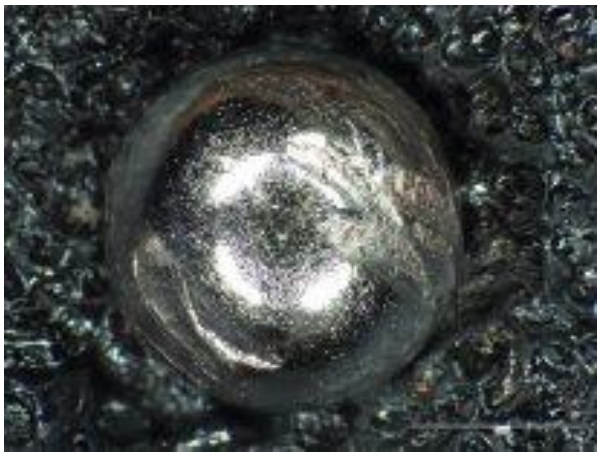

Fig. 1- Sample MAT - 2351

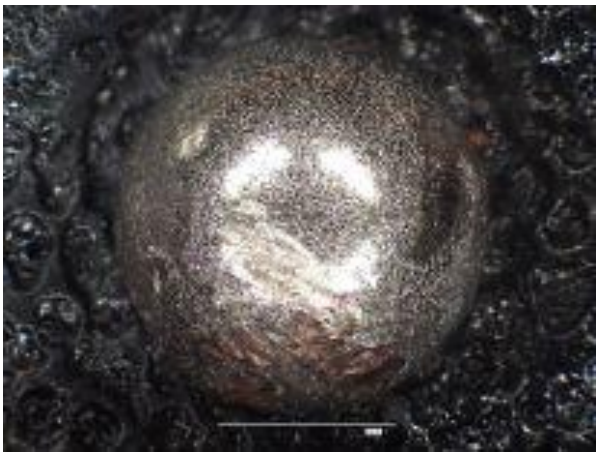

Fig. 2 – Sample MAT - 2353

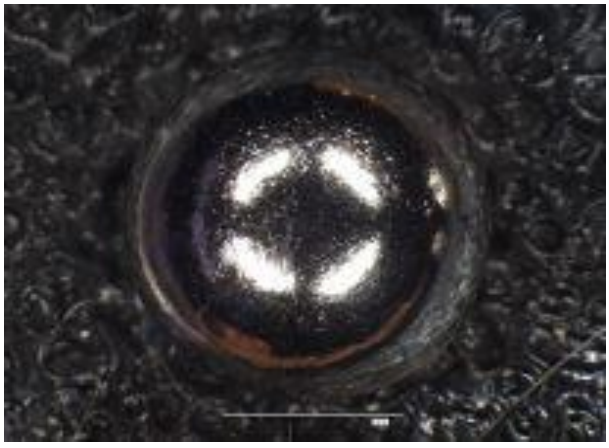

Fig. 3 – Sample MAT – 2378

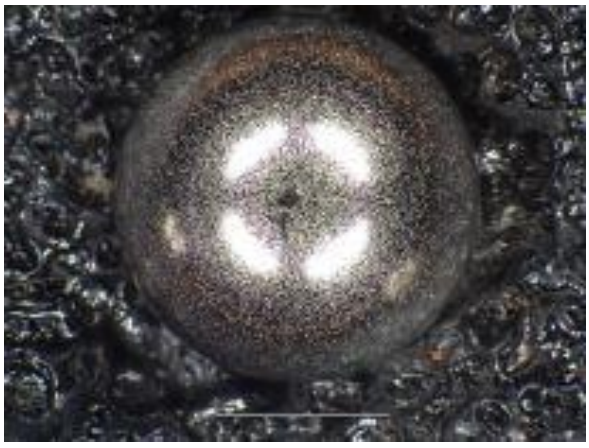

Fig. 4 – Sample MAT - 2379

Fig. 5 – Sample MAT - 2380

sample bar containing the samples was introduced into the analytical chamber of the instrument maintaining a very high vacuum level around low 10^{-9} mbar. All samples one by one were brought into center of the x-ray beam where the counts for any element were maximum. Maximum counts were also obtained in the height (z-direction) prior to any analysis.

Analysis procedure for all samples were same. For the brevity of this report only MAT -2378 sample analysis has been elaborated. Samples had a diameter of two mm, but the analysis area used had a dimension of 700 x 300 microns at the top of the sphere. Samples were stored in alcohol, still the surface contained adsorbed molecules and other impurities, perhaps during processing. Fig. 6 shows an overall survey spectrum from the surface of sample MAT 2378 in the as-received condition without any sputter cleaning. Spectrum shows presence of significant amounts of C and O. These are most probably adsorbed on to the surface and can be removed by ion sputtering. Important peaks have been identified in Fig. 6. The Auger peaks from elements have not been identified but they are there.

Next step in the analysis was to get to the real metal by removing the surface contaminations and adsorbed species. An Argon ion gun was used for this purpose. The area cleaned by the ion gun was 2mm X 2mm assumed to cover the entire analysis area. From earlier experiments rate of material removal was established to be around 1.7 angstroms per second. Recalibrating the ion gun was not important since we are simply using the ion gun for cleaning the surface and not measuring film thicknesses. A two-minute sputter cleaning was employed for all the five samples. This would remove about 20 nm of extraneous material from the surface. Fig.7 shows the spectrum obtained after this surface cleaning. The O and C peaks have been reduced and the elemental peaks have become prominent.

We were asked only to report only the important element distributions on the surface. These elements are Ni, Fe, and Cr. Each of them had more than one peaks. For various reasons, we chose Ni 3p, Fe 3p, and Cr 2p peaks to integrate the intensity for quantitative analysis.

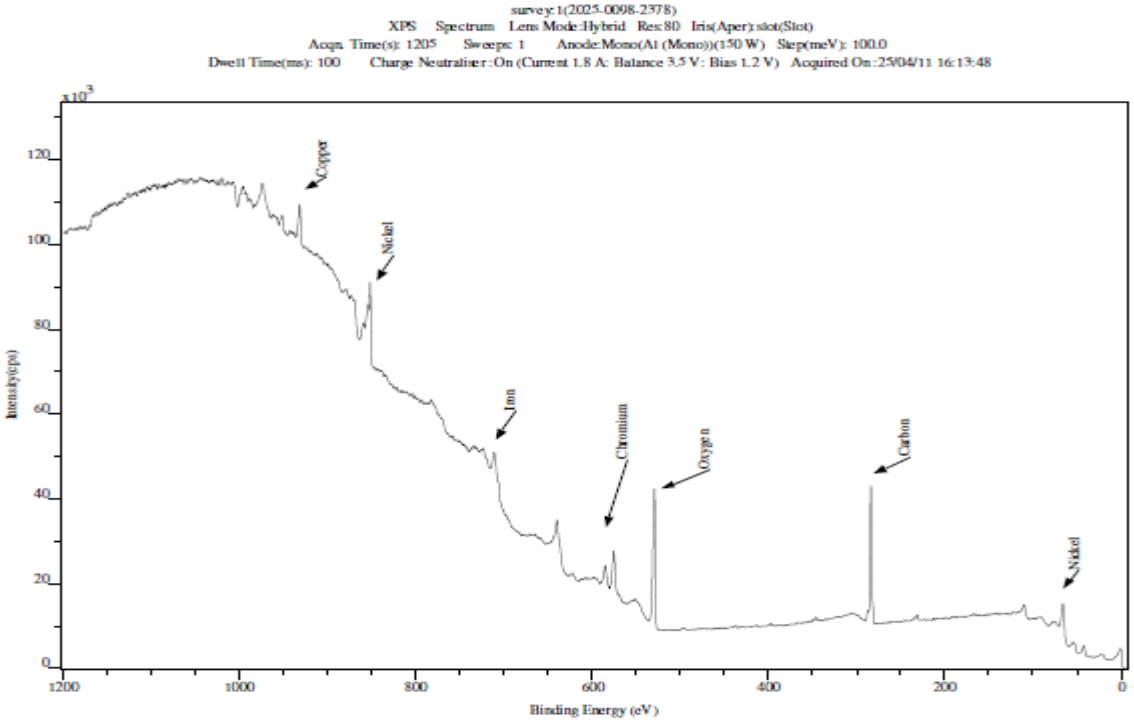

Fig.6 – Survey spectrum on as-received sample MAT – 2378. Peaks from important elements are identified.

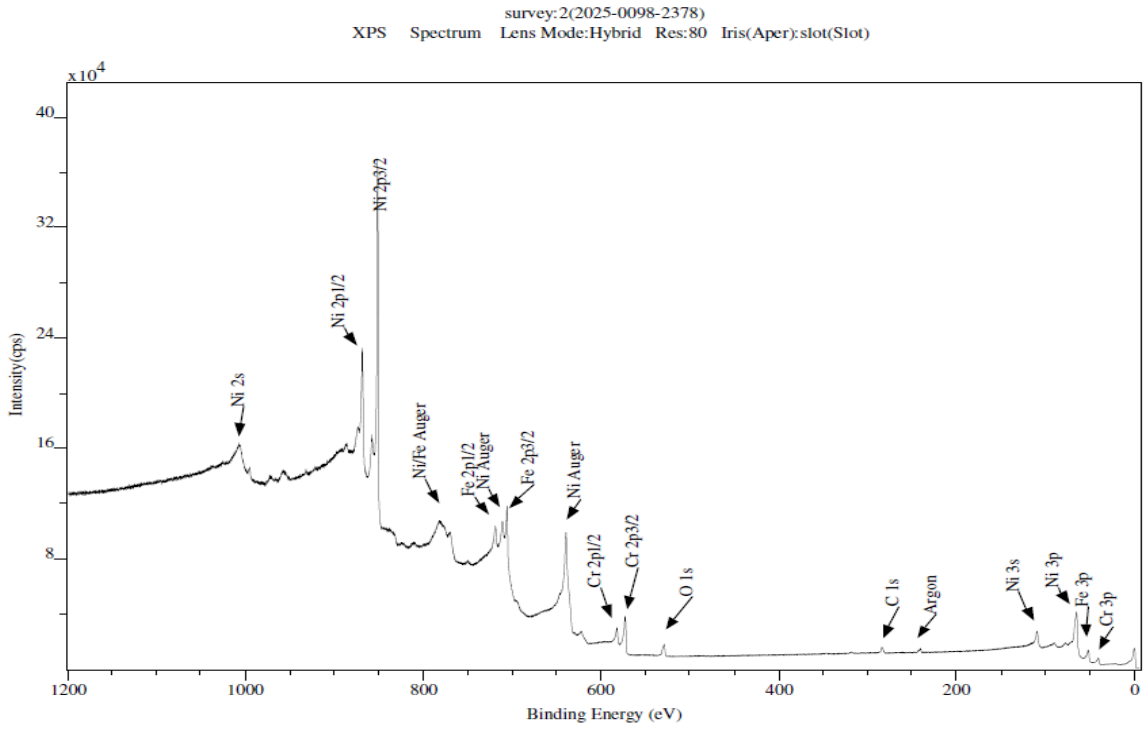

Fig.7 – Spectrum from cleaned MAT – 2378 sample. All peaks are identified.

Fig. 8 shows the positions of the chosen peaks on the spectrum in Fig.7 and Fig.9, the atomic percentages, both for sample MAT - 2378. As mentioned earlier, the above elaborates the surface analysis for sample MAT -2378. For brevity, only the final analysis results for other samples in the Quantification Report form (like Fig. 9) have been presented in Figs. 10 through 13.

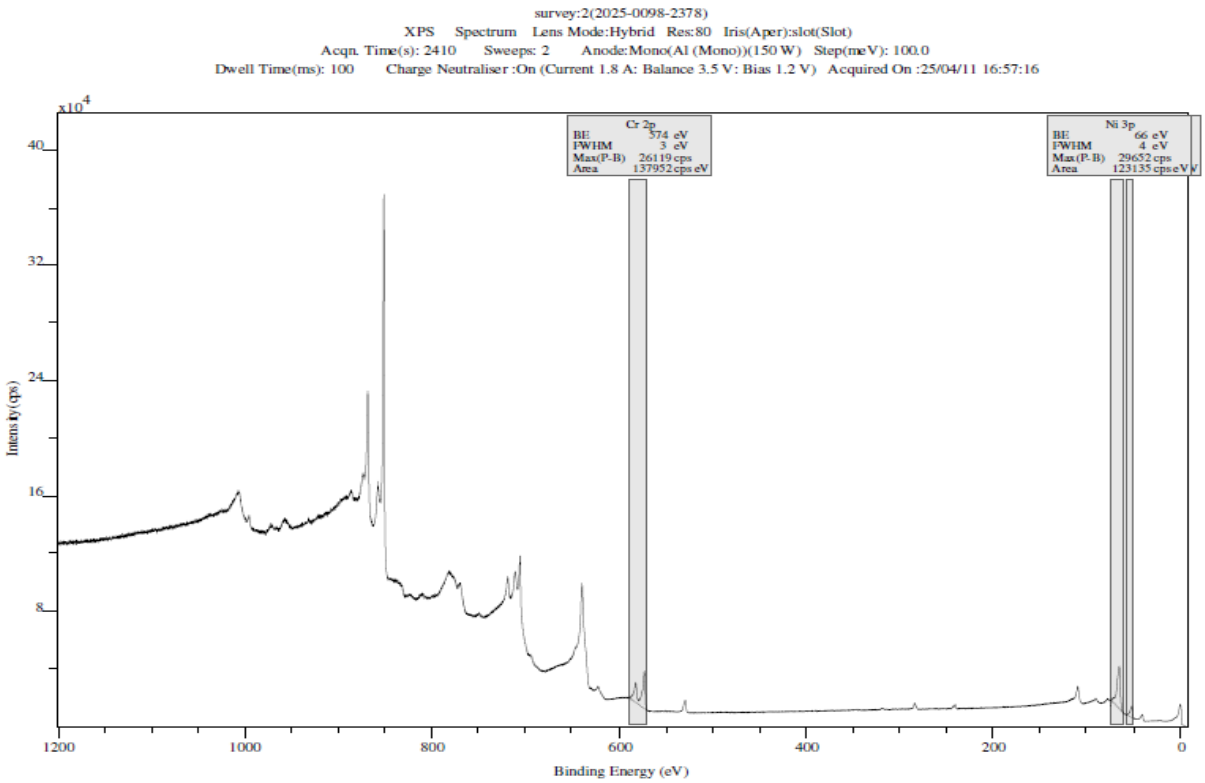

Fig.8 – Shows the three regions (peak areas) used in the intensity calculations for MAT-2378.

Quantification Report

/C=/data/Panda/2025-0098-2378.dset Thu Apr 17 14:09:03 2025

State #0 : Etch Time 0.00 seconds

Peak	Type	Position BE (eV)	FWHM (eV)	Raw Area (cps eV)	RSF	Atomic Mass	Atomic Conc %	Mass Conc %
Cr 2p	Reg	573.500	2.598	137952.5	2.427	51.996	18.75	17.14
Fe 3p	Reg	52.400	2.626	24416.0	0.370	55.846	19.59	19.23
Ni 3p	Reg	65.800	3.573	123135.2	0.598	58.702	61.66	63.63

Fig.9 – Relative surface atomic concentrations for selected elements on sample MAT-2378.

Quantification Report

/C=/data/Panda/2025-0098-2351.dset Thu Apr 17 14:13:38 2025

State #0 : Etch Time 0.00 seconds

Peak	Type	Position BE (eV)	FWHM (eV)	Raw Area (cps eV)	RSF	Atomic Mass	Atomic Conc %	Mass Conc %
Cr 2p	Reg	571.300	2.577	114995.5	2.427	51.996	22.18	20.38
Fe 3p	Reg	49.800	2.870	19182.2	0.370	55.846	21.81	21.52
Ni 3p	Reg	63.300	3.480	78931.0	0.598	58.702	56.01	58.10

Fig.10 - Relative surface atomic concentrations for selected elements on sample MAT-2351.

Quantification Report

/C=/data/Panda/2025-0098-2353.dset Thu Apr 17 14:22:49 2025

State #0 : Etch Time 0.00 seconds

Peak	Type	Position BE (eV)	FWHM (eV)	Raw Area (cps eV)	RSF	Atomic Mass	Atomic Conc %	Mass Conc %
Cr 2p	Reg	574.200	2.394	109282.5	2.427	51.996	25.85	23.66
Fe 3p	Reg	53.100	2.715	3934.5	0.370	55.846	5.50	5.40
Ni 3p	Reg	66.400	3.537	78744.0	0.598	58.702	68.65	70.94

Fig. 11 - Relative surface atomic concentrations for selected elements on sample MAT-2353.

Quantification Report

/C=/data/Panda/2025-0098-2379.dset Thu Apr 17 14:44:52 2025

State #0 : Etch Time 0.00 seconds

Peak	Type	Position BE (eV)	FWHM (eV)	Raw Area (cps eV)	RSF	Atomic Mass	Atomic Conc %	Mass Conc %
Cr 2p	Reg	574.100	2.443	186652.5	2.427	51.996	20.12	18.27
Fe 3p	Reg	53.000	1.844	5306.5	0.370	55.846	3.38	3.29
Ni 3p	Reg	66.500	3.760	192556.0	0.598	58.702	76.50	78.44

Fig.12 - Relative surface atomic concentrations for selected elements on sample MAT-2379.

Quantification Report

/C=/data/Panda/2025-0098-2380.dset Thu Apr 17 14:41:14 2025

State #0 : Etch Time 0.00 seconds

Peak	Type	Position BE (eV)	FWHM (eV)	Raw Area (cps eV)	RSF	Atomic Mass	Atomic Conc %	Mass Conc %
Cr 2p	Reg	574.200	2.713	163505.0	2.427	51.996	18.60	16.87
Fe 3p	Reg	52.900	1.890	6358.8	0.370	55.846	4.27	4.16
Ni 3p	Reg	66.300	3.797	183941.5	0.598	58.702	77.13	78.97

Fig. 13 - Relative surface atomic concentrations for selected elements on sample MAT-2380.

Bibliography

[1] M. Mohr, D. M. Matson and H.-J. Fecht, “Electromagnetic levitation containerless processing of metallic materials in microgravity: thermophysical properties,” *npj Microgravity*, vol. 9, pp. 1-12, 2023.

[2] D. M. Matson, G. Pottlacher and H.-J. Fecht, “Thermophysical Property Measurement: A Call to Action,” *International Journal of Microgravity Science and Application,* vol. 33, no. 3, p. 330301, 2016.

[3] J. Brillo, Thermophysical Properties of Multicomponent Liquid Alloys, De Gruyter Oldenbourg, 2016.

[4] D. M. Matson, R. Wunderlich and H.-J. Fecht, “Use of Thermophysical Properties to Select and Control Convection during Rapid Solidification of Steel Alloys using Electromagnetic Levitation on the Space Station,” *JOM*, vol. 69, no. 8, pp. 1311-1318, 2017.

[5] J. Nawer, T. Ishikawa, G. Pottlacher and D. M. Matson, “A comparison of Inconel 625 density and thermal expansion coefficient measurements in terrestrial and microgravity environments,” in *ATPC2022, 13th Asian Thermophysical Property Conference,* Sendai, Japan, 2023.

[6] B. S. Phillips, J. Nawer, P. Muusha, T. Leitner, C. Turk, M. P. Sansoucie and D. M. Matson, “Thermophysical Property Measurements and Comparison of Inconel 625 and 718 From Competing Vendor Formulations Using Electrostatic Levitation,” in *22nd Symposium on Thermophysical Properties*, 2024.

[7] B. Fu, “Thermodynamic Modeling of the Evaporation of Ternary Analog Alloys of Inconel 625 and Inconel 718 During Electrostatic Levitation,” Tufts University, Medford, 2025.

[8] M. P. SanSoucie, J. R. Rogers, X. Xiao, J. Nawer, M. Pleskus and D. M. Matson, “Thermophysical properties of nickel-based superalloys,” in *Twentieth Symposium on Thermophysical Properties*, Boulder, CO, 2018.

[9] T. Ishikawa, P.-F. Paradis, T. Itami and S. Yoda, “Non-contact thermophysical property measurements of refractory metals using an electrostatic levitator,” *Measurement Science and Technology*, vol. 16, pp. 443-451, 2005.

[10] M. Mohr, R. N. R. Wunderlich, E. Ricci and H. Fecht, “Precise Measurements of Thermophysical Properties of Liquid Ti–6Al–4V (Ti64) Alloy On Board the International Space Station,” *Advanced Engineering Materials*, no. 22, pp. 1-10, 2020.

[11] I. Egry, A. Diefenbach, W. Dreier and J. Piller, “Containerless Processing in Space Thermophysical Property Measurements using Electromagnetic Levitation,” *International Journal of Thermophysics*, vol. 22, p. 569–578, 2001.

[12] J. Brillo, G. Lohöfer, F. Schmidt-Hohagen, S. Schneider and I. Egry, “Thermophysical property measurements of liquid metals by electromagnetic levitation,” *International Journal of Materials and Product Technology*, vol. 26, no. 3-4, pp. 247-273, 2006.

[13] G. Lohöfer, “Theory of an Electromagnetically Levitated Metal Sphere I: Absorbed Power,” *SIAM Journal on Applied Mathematics*, pp. 567-581, 1989.

[14] G. Lohöfer, M. Beckers, T. Blumberg, D. Bräuer, S. Schneider, T. Volkmann and A. Meyer, “TEMPUS - A microgravity electromagnetic levitation facility for parabolic flights,” *Paper appears in Rev. Sci. Instrum. (2024)*, pp. 1-6, 2024.

[15] P. Muusha, B. Stanford, M. Kolbe and D. M. Matson, “Relating Cooling Rates in Superheated Liquid During Solidification for Powder Characterization,” *Metall Mater Trans A*, vol. 54, no. 11, pp. 4169-4178, 2023.

[16] J. Nawer, B. Stanford, M. Kolbe, S. Schneider, S. Gossé, R. K. Wunderlich, M. Mohr, A. Borzì, A. Neels and D. M. Matson, “Thermodynamic assessment of evaporation

during molten steel testing onboard the International Space Station," *npj Microgravity,* vol. 10, p. 77, 2024.

[17] R. Novakovic and J. Brillo, "Thermodynamics, thermophysical and structural properties of liquid Fe–Cr alloys," *Journal of Molecular Liquids,* vol. 200, pp. 153-159, 2014.

[18] T. Leitner, "Thermophysical property measurement of industrial metals and alloys using electromagnetic levitation," 2021. [Online]. Available: https://www.google.com/url?sa=t&source=web&rct=j&opi=89978449&url=https://www.tugraz.at/fileadmin/user_upload/Institute/IEP/Thermophysics_Group/Files/Diss-LeitnerThomas.pdf&ved=2ahUKEwi-8vyTkeiPAxUiK1kFHabWCdkQFnoECCEQAQ&usg=AOvVaw1s_bJg-IZcGDBwX5dvnQg7.

[19] J. Nawer, "Thermophysical Property Measurement using Containerless Levitation Techniques in Microgravity and Terrestrial Environments," Tufts University , 2022. [Online].

[20] R. Schmid-Fetzer and J. Gröbner, "Focused Development of Magnesium Alloys Using the Calphad Approach," *Advanced Engineering Materials,* vol. 3, no. 12, p. 947, December 2001.

[21] H. Kobatake and J. Brillo, "Density and viscosity of ternary Cr–Fe–Ni liquid alloys," *Journal of Materials Science,* vol. 48, no. 19, pp. 6818-6824, 2013.

[22] J. Butler, "The thermodynamics of the surfaces of solutions," *Proceedings of the Royal Society of London. Series A,* vol. 135, no. 827, pp. 348-375, 1932.

[23] J. Brillo, R. Brooks and I. Egry, "Density and viscosity of liquid ternary Al-Cu-Ag alloys," *High Temperatures - High Pressures,* pp. 371-381, 2008.

[24] B. Reiplinger and J. Brillo, "Density and excess volume of the liquid Ti–V system measured in electromagnetic levitation," *Journal of Materials Science,* vol. 57, pp. 1-11, 2022.

[25] X. Xiao and J. Brillo, “Surface tension of liquid Fe–Ni, Fe–Cr, and Ni–Cr with physics-informed statistical modeling on the influence of oxygen content,” *Journal of Molecular Liquids,* vol. 360, p. 119599, 2022.

[26] T. Tanaka and T. Iida, "Application of a thermodynamic database to the calculation of surface tension for iron-base liquid alloys," *Steel Research,* vol. 65, no. 1, pp. 21-28, 1994.

[27] L. Kaufman and H. Nesor, “Coupled phase diagrams and thermochemical data for transition metal binary systems — I,” *Calphad,* vol. 2, no. 1, pp. 55-80, 1978.

[28] L. Kaufman and H. Nesor, “Coupled phase diagrams and thermochemical data for transition metal binary systems — II,” *Calphad,* vol. 2, no. 1, pp. 81-108, 1978.

[29] J. Nawer, T. Ishikawa, H. Oda, C. Koyama and D. M. Matson, “Uncertainty Quantification of Thermophysical Property Measurement in Space and on Earth: A Study of Liquid Platinum Using Electrostatic Levitation,” *Journal of Astronomical and Space Sciences,* vol. 40, no. 3, pp. 93-100, 2023.

[30] J. Nawer, T. Ishikawa, H. Oda, C. Koyama, H. Saruwatari, M. P. Sansoucie, B. Philips, S. Gossé, M. Mohr, M. Kolbe and D. M. Matson, “A quantitative comparison of thermophysical property measurement of CMSX-4 Plus (SLS) in microgravity and terrestrial environments,” *High Temperatures-High Pressures,* vol. 52, p. 323–339, 2023.

[31] J. Nawer, T. Ishikawa, H. Oda, C. Koyama, H. Saruwatari, M. P. Sansoucie, B. Philips, S. Gossé, M. Mohr, M. Kolbe and D. M. Matson, “Uncertainty analysis and performance evaluation of thermophysical property measurement of liquid Au in microgravity,” *npj Microgravity,* vol. 9, p. 38, 2023.

[32] J. Nawer, S. Gossé and D. M. Matson, “Tracking evaporation during levitation processing of nickel-based superalloys on the ISS,” *JOM,* vol. 72, no. 9, pp. 3132-3139, 2020.

[33] J. J. Wessing and J. Brillo, “Density, Molar Volume, and Surface Tension of Liquid Al-Ti,” *The Minerals, Metals & Materials Society and ASM International,* vol. 48, pp. 898-882, 2016.

[34] M. Watanabe, M. Adachi and H. Fukuyama, “Densities of Fe–Ni melts and thermodynamic correlations,” *Journal of Materials Science,* vol. 51, pp. 3303-3310, 2015.

[35] Q. Wang, W. Zhang, S. Li, M. Tong, W. Hou, H. Wang, Y. Hao, N. M. Harriso and R. Yang, “Material Characterisation and Computational Thermal Modelling of Electron Beam Powder Bed Fusion Additive Manufacturing of Ti2448 Titanium Alloy,” *materials,* vol. 14, pp. 1-23, 2021.

[36] H. P. Wang, S. J. Yang and B. B. Wei, “Density and structure of undercooled liquid titanium,” *Chinese Science Bulletin,* no. 57, pp. 719-723, 2012.

[37] T. Tanaka, K. Hack and T. Iida, “Application of Thermodynamic Databases to the Evaluation of Surface Tensions of Molten Alloys, Salt Mixtures and Oxide Mixtures,” *Zeitschrift für Metallkunde,* pp. 380-389, 1996.

[38] P. M. Smith, J. W. Elmer and G. F. Gallegos, “MEASUREMENT OF THE DENSITY OF LIQUID ALUMINUM ALLOYS BY AN X-RAY ATTENUATION TECHNIQUE,” *Scripta Materialia,* no. 40, pp. 937-941, 1999.

[39] G. Pottlacher, High Temperature Thermophysical Properties of 22 Pure Metals, Graz: edition keiper, 2010.

[40] C. Notthoff, H. Franz, M. Hanfland, D. Herlach, D. Holland-Moritz and W. Petry, “Electromagnetic levitation apparatus for investigations of the phase selection in undercooled melts by energy-dispersive x-ray diffraction,” *REVIEW OF SCIENTIFIC INSTRUMENTS* , pp. 3791-3796, 2000.

[41] H. M. Lu and Q. Jiang, “Surface Tension and Its Temperature Coefficient for Liquid Metals,” *The Journal of Physical Chemistry B,* pp. 15463-15468, 2005.

[42] G. Lohöfer, “Force and Torque of an electromagnetically levitated metal sphere,” *Quarterly of Applied Mathematics,* pp. 495-518, 1993.

[43] G. Lohöfer and J. Piller, “40th AlAA Aerospace Sciences Meeting and Exhibit,” in *The new ISS Electromagnetic Levitation Facility: 'MSL-EML',* Reno, NV, 2002.

[44] E. S. Levin, A. G. D. and G. P. V., “Density and surface-energy polytherms of liquid (molten) aluminum,” *High Temperature 6,* no. 3, p. 416, 1968.

[45] J. Lee, D. M. Madson, S. Binder, M. Kolbe, D. Herlach and R. Hyers, “Magnetohydrodynamic Modeling and Experimental Validation of Convection Inside Electromagnetically Levitated Co-Cu Droplets,” *The Minerals, Metals & Materials Society,* pp. 1018-1023, 2014.

[46] S. Krishnan, G. P. Hansen, R. H. Hauge and J. L. Margrave, “Spectral emissivities and optical properties of electromagnetically levitated liquid metals as functions of temperature and wavelength,” *High temperature science,* no. 29, pp. 17-52, 1990.

[47] H. Kobatake, J. Brillo, J. Schmitz and P. Pichon, “Surface tension of binary Al–Si liquid alloys,” *Journal of Materials Science,* pp. 3351-3360, 2015.

[48] H. Kobatake, J. Brillo and J. Schmitz, “Density and viscosity of ternary Al–Cu–Si liquid alloys,” *Journal of Materials Science ,* pp. 3541-3549, 2014.

[49] B. J. Keene, “Review of data for the surface tension of pure metals,” *International Materials Reviews,* vol. 4, no. 38, pp. 157-192, 1993.

[50] A. Kasama, A. McLean, W. Miller, Z. Morita and M. Ward, “Surface Tension of Liquid Iron and Iron-Oxygen Alloys,” *The Canadian Journal of Metallurgy and Materials Science ,* pp. 9-17, 1983.

[51] G. Kaptay, “An improved derivation of the Butler equations for surface tension of solutions,” *Langmuir,* no. 33, p. 10987–10992, 2019.

[52] G. Kaptay, “The partial surface tension of components of a solution,” *Langmuir,* vol. 31, pp. 5796-5804, 2015.

[53] G. Kaptay, “Extension of the Gibbs-Duhem relation to partial molar surface thermodynamic properties of solutions,” *Langmuir,* vol. submitted, 2022.

[54] H. Fukuyama and Y. Waseda, High Temperature Measurements of Materials, Berlin: Springer, 2009.

[55] I. Egry, D. Holland-Moritz, R. Novakovic, E. Ricci, R. Wunderlich and N. Sobczak, “Thermophysical Properties of Liquid AlTi-Based Alloys,” *International Journal of Thermophysics,* no. 31, pp. 949-965, 2010.

[56] I. Egry, E. Ricci, R. Novakovic and S. Ozawa, “Surface tension of liquid metals and alloys - Recent developments,” *Advances in Colloid and Interface Science,* pp. 198-212, 2010.

[57] I. Egry, “Surface tension of compound forming liquid binary alloys: A simple model,” *Journal of Material Science,* no. 39, pp. 6365-6366, 2004.

[58] V. S. D. Herzog, E. Wycisk and C. Emmelmann, “Additive manufacturing of metals,” *Acta Materialia,* pp. 371-392, 2016.

[59] J. Brillo, I. Egry and J. Westphal, “Density and thermal expansion of liquid binary Al – Ag and Al – Cu alloys,” *International Journal of Materials Research,* vol. 2, no. 99, pp. 162-167, 2013.

[60] J. Brillo, J. Wessing, H. Kobatake and H. Fukuyama, “Surface tension of liquid Ti with adsorbed oxygen and its prediction,” *Journal of Molecular Liquids,* pp. 1-12, 2019.

[61] J. Brillo and G. Kolland, “Surface tension of liquid Al-Au binary alloys,” *J. Mater. Sci.,* 2016.

[62] J. Brillo, G. Lauletta, L. Vaianella, E. Arato, D. Giuranno, R. Novakovic and E. Ricci, “Surface tension of liquid Ag-Cu binary alloys,” *ISIJ International,* vol. 54, pp. 2115-2119, 2014.

[63] J. Brillo, M. Watanabe and H. Fukuyama, “Relation between excess volume, excess free energy and isothermal compressibility in liquid alloys,” *Journal of Molecular Liquids,* vol. 326, pp. 114395 1-35, 2021.

[64] J. Brillo and I. Egry, “Density Determination of Liquid Copper, Nickel, and Their Alloys,” *International Journal of Thermophysics,* no. 24, pp. 1155-1170, 2004.

[65] J. Brillo, I. Egry and I. Ho, "Density and Thermal Expansion of Liquid Ag–Cu and Ag–Au Alloys," *International Journal of Thermophysics,* vol. 27, pp. 494-506, 2006.

[66] M. J. Assael and K. Kakosimos, “Reference Data for the Density and Viscosity of Liquid Aluminum and Liquid Iron,” *Journal of Physical and Chemical Reference Data,* no. 35, pp. 285-300, 2006.

[67] S. Amore, J. Brillo, I. Egry and R. Novakovic, “Surface tension of liquid Cu–Ti binary alloys measured by electromagnetic levitation and thermodynamic modelling,” *Applied Surface Science,* pp. 7739-7745, 2011.

[68] S. Amore, S. Delsante, H. Kobatake and J. Brillo, “Excess volume and heat of mixing in Cu-Ti liquid mixture,” *The Journal of Chemical Physics,* vol. 139, pp. 064504-(1-6), 2013.

[69] B. C. Allen, “THE SURFACE TENSION OF LIQUID TRANSITION METALS AT THEIR MELTING POINTS,” *Trans. AIME,* no. 227, p. 1175, 1963.

[70] D. Zivkovic, “A new approach to estimate the viscosity of the ternary liquid alloys using the Budai-Benko-Kaptay Equation,” *Metallurgical and Materials Transactions B,* vol. 39, pp. 395-398, 2008.

[71] X. Xiao, J. Brillo, R. W. Hyers and D. M. Matson, “Impact of convection on the damping of an oscillating droplet during viscosity measurement using the ISS-EML facility,” *npj Microgravity,* vol. 7, pp. 1-7, 2021.

[72] X. Xiao, R. W. Hyers and D. M. Matson, “Deformation induced frequency shifts of oscillating droplets during molten metal surface tension measurement,” *Applied Physics Letters,* vol. 113, no. 01, p. 011903, 2018.

[73] R. N. Singh and F. Sommer, “Viscosity of liquid alloys: generalization of Andrade’s equation,” *Monatsh Chem,* vol. 143, pp. 1235-1242, 2021.

[74] D. M. Matson, R. W. Hyers, T. Volkmann and H.-J. Fecht, “Phase selection in the mushy zone: LODESTARS and ELFSTONE Programs,” in *Journal of Physics Conference Series*, 2011.

[75] H. Kobatake and J. Brillo, “Surface tension and viscosity measurement of ternary Cr–Fe–Ni liquid alloys measured under microgravity during parabolic flights,” *High Temperatures-High Pressures,* vol. 47, pp. 465-477, 2018.

[76] L. Kaufman and H. Nesor, “Coupled phase diagrams and thermochemical data for transition metal binary systems-I,” *Calphad,* vol. 2, no. 1, pp. 55-80, 1978.

[77] S. Jeon, M. P. Sansoucie and D. M. Matson, “Hypercooling limit, heat of fusion, and temperature-dependent specific heat of Fe-Cr-Ni melts,” *Journal of Chemical Thermodynamics,* vol. 138, pp. 51-58, 2019.

[78] S. Jeon and D. M. Matson, “Density, Excess Volume, and Structure of Fe-Cr-Ni melts,” *Journal of Chemical Physics,* vol. 152, p. 094501, 2020.

[79] J. Brillo, I. Egry and T. Matsushita, “Density and surface tension of liquid ternary Ni-Cu-Fe,” *Z. Metallkd.,* vol. 97, pp. 28-34, 2006.

[80] F. Xiao, R. Yang and C. Zhang, “Surface tension of molten Ni–W and Ni–Cr alloys,” *Materials Science and Engineering B,* vol. 132, no. 1–2, pp. 183-186, 2006.

[81] T. Tanaka and S. Hara, “Thermodynamic evaluation of surface tension of liquid metal-oxygen systems,” *Steel Research,* vol. 72, no. 11–12, pp. 439-445, 2001.

[82] A. Sharan, T. Nagasaka and A. Cramb, “Surface tensions of liquid Fe-Cr and Fe-Cr-N alloys,” *Metallurgical and Materials Transactions B (Process Metall.),* vol. 25, no. 4, 1994.

[83] R. Novakovic, “Bulk and surface properties of liquid Al–Cr and Cr–Ni alloys,” *Journal of Physics: Condensed Matter,* vol. 23, no. 23, p. 235107, 2011.

[84] K. Morohoshi, M. Uchikoshi, M. Isshiki and H. Fukuyama, “Surface tension of liquid iron as functions of oxygen activity and temperature,” *ISIJ International,* vol. 51, no. 10, pp. 1580-1586, 2011.

[85] H. Kobatake and J. Brillo, “Density and thermal expansion of Cr–Fe, Fe–Ni, and Cr–Ni binary liquid alloys,” *Journal of Materials Science,* vol. 48, no. 14, pp. 4934-4941, 2013.

[86] M. Kimoto, T. Itoh, T. Nagasaka, M. Hino, K. Suzuki and S. Ban-Ya, Steelmaking Data Sourcebook, The Japan Society for the Promotion of Science (19th Committee on Steelmaking), 1988.

[87] Y. Kim, J. Lim, J. Choe and J. Lee, “Surface tension of liquid Fe–O alloys: Revisiting Belton’s two-step adsorption model,” *Metallurgical and Materials Transactions B,* vol. 45, no. 3, pp. 947-952, 2014.

[88] Y. Kang, J. Brillo, J. Han, H. Kim, D. Giuranno, R. Novakovic, E. Ricci, E. Arato and J. Lee, “Oxygen adsorption of molten Ag–Cu eutectic alloy and its associated surface modification,” *Journal of Molecular Liquids,* vol. 319, p. 114294, 2020.

[89] T. Iida and R. Guthrie, The Physical Properties of Liquid Metals, Clarendon Press, Oxford, 1988.

[90] J. Brillo and I. Egry, “Surface tension of nickel, copper, iron and their binary alloys,” *Journal of Materials Science,* vol. 40, no. 9, pp. 2213-2216, 2005.

[91] M. Ranaiefar, “A differential evaporation model to predict chemistry change of additively manufactured metals,” *Materials & Design,* vol. 213, p. 110328, 2022.

[92] L. Lü, J. Fuh and Y. S. Wong, Laser-Induced Materials and Processes for Rapid Prototyping, 1st edn ed., : Springer Science & Business Media, 2001.

[93] J. Nawer, “Measurement of Mass Evaporation of Ni-Based Single Crystal Super Alloy Using Electrostatic Levitation (ESL) & Electromagnetic Levitation (EML),” Tufts University, 2018. [Online]. Available:

https://www.academia.edu/download/62542125/Jannatun_Nawer_MS_Thesis20200329-114713-105o9eb.pdf.

[94] B. Reiplinger, Y. Plevachuk and J. Brillo, “Surface tension of liquid Ti, V and their binary alloys measured by electromagnetic levitation,” *Journal of Materials Science,* vol. 57, 2022.

[95] B. Reiplinger, Y. Plevachuk and J. Brillo, “Experimental study of density, molar volume and surface tension of the liquid Ti-V system measured in electromagnetic levitation,” *High Temperatures-High Pressures,* vol. 52, 2023.

[96] L. Kaufman, “Coupled phase diagrams and thermochemical data for transition metal binary systems — VI,” *Calphad,* vol. 3, no. 1, pp. 45-76, 1979.

[97] L. Kaufman and H. Nesor, “Coupled phase diagrams and thermochemical data for transition metal binary systems — V,” *Calphad,* vol. 2, no. 4, pp. 325-348, 1978.

[98] L. Kaufman and H. Nesor, “Coupled phase diagrams and thermochemical data for transition metal binary systems — IV,” *Calphad,* vol. 2, no. 4, pp. 295-318, 1978.

[99] L. Kaufman, “Coupled phase diagrams and thermochemical data for transition metal binary systems — III,” *Calphad,* vol. 2, no. 2, pp. 117-146, 1978.

[100] “OpenAI.,” ChatGPT, 2025. [Online]. Available: https://chat.openai.com/chat.